

Energy-resolved Mass Spectrometry for Positional Isomer Differentiation of New Psychoactive Substances

メタデータ	言語: eng 出版者: 公開日: 2020-01-08 キーワード (Ja): キーワード (En): 作成者: メールアドレス: 所属:
URL	http://hdl.handle.net/2297/00056478

This work is licensed under a Creative Commons Attribution-NonCommercial-ShareAlike 3.0 International License.



博士論文

Energy-resolved Mass Spectrometry for Positional Isomer Differentiation of New Psychoactive Substances

エネルギー分解質量分析法による新規乱用薬物の
位置異性体識別に関する研究

金沢大学大学院自然科学研究科
物質化学専攻

学籍番号 1724022007
氏名 村上貴哉
主任指導教員名 長谷川浩
提出年月 2019年9月

List of Abbreviations

AB-FUBINACA	<i>N</i> -(1-amino-3-methyl-1-oxobutan-2-yl)-1-(4-fluorobenzyl)-1 <i>H</i> -indazole-3- carboxamide
ANOVA	analysis of variance
CE	collision energy
CID	collision-induced dissociation
DFT	density functional theory
EI	electron ionization
ERMS	energy-resolved mass spectrometry
ESI	electrospray ionization
FMC	fluoromethcathinone
FPPP	fluoro- α -pyrrolidinopropiophenone
FUBINAE	1-[1-(2-, 3-, or 4-fluorobenzyl)-1 <i>H</i> -indazol-3-yl]ethanone
GC	gas chromatography
LC	liquid chromatography
LIT	linear ion trap
LLE	liquid-liquid extraction
LOD	limit of detection
MA	methamphetamine
MDMA	3,4-methylenedioxymethamphetamine
MeOPPP	methoxy- α -pyrrolidinopropiophenone
MIP	molecularly imprinted polymer
MMC	methylmethcathinone
MS	mass spectrometry
NMR	nuclear magnetic resonance
NPS	new psychoactive substance
QpQ	triple quadrupole
RSD	relative standard deviation
SD	standard deviation
S _N Ar	nucleophilic aromatic substitution
SPE	solid-phase extraction
TFA	trifluoroacetylation
THC	Δ^9 -tetrahydrocannabinol
TOF	time-of-flight
Triton B	benzyltrimethylammonium hydroxide

Table of Contents

List of Abbreviations.....	i
Table of Contents	ii
Chapter 1 General introduction	1
1.1 Recent prevalence of new psychoactive substances	1
1.2 NPS analysis in forensic science.....	4
1.3 Analytical problems in NPS identification.....	6
1.3.1 Continuous emergence of new structural NPSs	6
1.3.2 Existence of structurally similar drugs.....	7
1.3.3 Structural degradation of NPSs	8
1.4 Objectives.....	9
Chapter 2 Differentiation of AB-FUBINACA positional isomers by the abundance of product ions using electron ionization-triple quadrupole mass spectrometry.....	11
2.1 Introduction	11
2.2 Material and Methods.....	13
2.2.1 Reagents	13
2.2.2 Instrumentation.....	13
2.2.3 Principle of energy-resolved mass spectrometry	14
2.2.4 Breakdown curve fittings	14
2.2.5 Statistical and theoretical calculations	15
2.3 Results and discussion.....	16
2.3.1 Full scan mass spectrometry	16
2.3.2 Energy-resolved mass spectrometry.....	18
2.3.3 Positional isomer differentiation based on product ion abundances	22
2.3.4 Theoretical calculations of dissociation energy	28
2.4 Summary	34
Chapter 3 Elucidation of the fluorine substitution position on the phenyl ring of synthetic cannabinoids by triple quadrupole mass spectrometry	37
3.1 Introduction	37
3.2 Materials and Methods	38
3.2.1 Reagents	38
3.2.2 Synthesis of model compounds of synthetic cannabinoids.....	39
3.2.3 Instrumentation.....	40
3.2.4 Statistical calculations	41
3.3 Results and Discussion.....	42
3.3.1 Gas chromatography	42

3.3.2	Full scan mass spectrometry	42
3.3.4	Energy-resolved mass spectrometry.....	45
3.3.5	Breakdown curves of <i>o</i> -, <i>m</i> -, and <i>p</i> -FUBINAEs	47
3.3.6	Comparisons of <i>o</i> -, <i>m</i> -, and <i>p</i> -FUBINAEs with synthetic cannabinoids.....	51
3.4	Summary	53
Chapter 4	Differentiation of AB-FUBINACA and its five positional isomers using liquid chromatography–electrospray ionization– linear ion trap mass spectrometry and triple quadrupole mass spectrometry	55
4.1	Introduction	55
4.2	Materials and methods	56
4.2.1	Reagents	56
4.2.2	Instrumentation.....	56
4.2.3	Statistical calculations	57
4.3	Results and discussion.....	58
4.3.1	Liquid chromatography	58
4.3.2	Linear ion trap multiple-stage mass spectrometry	59
4.3.3	Triple quadrupole energy-resolved mass spectrometry	63
4.4	Summary	75
Chapter 5	Differentiation of the fluorine substitution position on the phenyl ring of fluoromethcathinones using energy-resolved mass spectrometry	77
5.1	Introduction	77
5.2	Material and Methods.....	78
5.2.1	Reagents	78
5.2.2	Instrumentation.....	79
5.2.3	Statistical and theoretical calculations	80
5.3	Results and discussion.....	81
5.3.1	Full scan mass spectrometry	81
5.3.2	Energy-resolved mass spectrometry.....	82
5.3.3	Theoretical calculations of dissociation energy	93
5.3.4	Comparisons with methylmethcathinone positional isomers.....	97
5.3.5	Application of the present method to forensic samples	102
5.4	Summary	103
Chapter 6	Differentiation of 2-, 3-, and 4-fluoro-α-pyrrolidino- propiofenones by Triton B-mediated one-pot reaction.....	105
6.1	Introduction	105
6.2	Materials and methods	106
6.2.1	Reagents	106

6.2.2	Syntheses	106
6.2.3	Synthetic procedures for optimization of Triton B-mediated reaction condition	107
6.2.4	Extraction procedure for instrumental analysis of reaction products..	107
6.2.5	Instrumental analysis of reaction products	108
6.3	Results and discussion.....	110
6.3.1	Chromatographic and mass spectral properties of <i>o</i> -, <i>m</i> -, and <i>p</i> - FPPPs	110
6.3.2	Optimization of Triton B-mediated reaction condition.....	111
6.3.3	Application to positional isomer differentiation	114
6.4	Summary	117
Chapter 7	Molecularly imprinted polymer solid-phase extraction of synthetic cathinones from urine and whole blood samples	119
7.1	Introduction	119
7.2	Material and methods	121
7.2.1	Reagents	121
7.2.2	Synthesis of methcathinone hydrochloride	121
7.2.3	Sample preparation.....	122
7.2.4	Molecularly imprinted polymer solid-phase extraction procedures....	123
7.2.5	Hydrophilic polymer-based solid-phase extraction procedure.....	123
7.2.6	Liquid-liquid extraction procedure.....	124
7.2.7	Instrumentation.....	124
7.2.8	Recovery, matrix effect, and linear regression.....	126
7.3	Results and discussion.....	127
7.3.1	Optimization of the sample solution pH	127
7.3.2	Influence of synthetic cathinone molecular structure on extraction efficiency	128
7.3.3	Extraction of synthetic cathinones from urine and whole blood samples	130
7.4	Summary	136
Chapter 8	Conclusion	139
References		143
List of Publications.....		154
Acknowledgments		155

Chapter 1 General introduction

1.1 Recent prevalence of new psychoactive substances

In recent years, novel synthetic drugs of abuse, generally referred to as new psychoactive substances (NPSs), have been marketed as “legal highs”, “herbal highs”, and “bath salts” on the internet or are available in specialized shops called “head shops” or “smart shops”. These NPSs have rapidly emerged worldwide as “legal” alternatives to controlled drugs, posing a serious threat to public health and safety and a challenge to drug policy [1–3]. NPSs are intentionally produced by introducing slight modifications to the chemical structure of controlled drugs to provide the effects similar to those of methamphetamine (MA), 3,4-methylenedioxymethamphetamine (MDMA), and Δ^9 -tetrahydrocannabinol (THC), while circumventing the existing legislative classification and penalties. Although the term “designer drugs” has been traditionally used to mean synthetic substances, the United Nations Office on Drugs and Crime (UNODC) has recently defined NPSs as “substances of abuse, either in a pure form or a preparation, that are not controlled by the 1961 Single Convention on Narcotic Drugs or the 1971 Convention on Psychotropic Substances, but which may pose a public health threat” [4,5], which not only includes newly developed or manufactured drugs but also recently distributed drugs that were previously developed. Till December 2017, more than 800 NPSs have been monitored in more than 110 countries and regions [4,6].

Both “synthetic cannabinoids” and “synthetic cathinones” are major emerging classes of NPSs [6]. Synthetic cannabinoids elicit cannabimimetic effects similar to THC, the active component in cannabis, by interacting with the CB₁ and CB₂ cannabinoid receptors [7–10]. Over the past 50 years, pharmaceutical companies and academic laboratories have developed synthetic cannabinoids as potential pharmaceutical agents for the treatment of pain. In late

2008, the European Monitoring Center for Drugs and Drug Addiction (EMCDDA) discovered several synthetic cannabinoids, including JWH-018, JWH-073, and CP-47,497, in herbal products marketed as incense or room odorizers under the brand name “Spice” [11,12]. Since then, synthetic cannabinoids for recreational use have become increasingly popular among young people, because they are inexpensive and are typically not detected by the standard marijuana drug tests. From 2008 to 2014, 142 synthetic cannabinoids were reported to the EMCDDA; till 2009, a variety of herbal products labeled “Spice” was being monitored in 21 EU countries (Fig. 1.1a). Also, in 2008, synthetic cathinones first emerged on the European illicit drug market [1,2,13]. In 2009–2010, there was a significant rise in the abuse of synthetic cathinones, initially in the United Kingdom and the rest of Europe [14], and subsequently in the United States. Synthetic cathinones, which are sold as bath salts or plant food (Fig. 1.1b), have been recreationally used as alternatives to stimulants such as amphetamine, MA, and MDMA, because they have amphetamine-like psychoactive and sympathomimetic effects. [15,16]. Mephedrone, methylenedioxypropylvalerone (MDPV), and methylone were the most widely abused within Europe and the US [17].

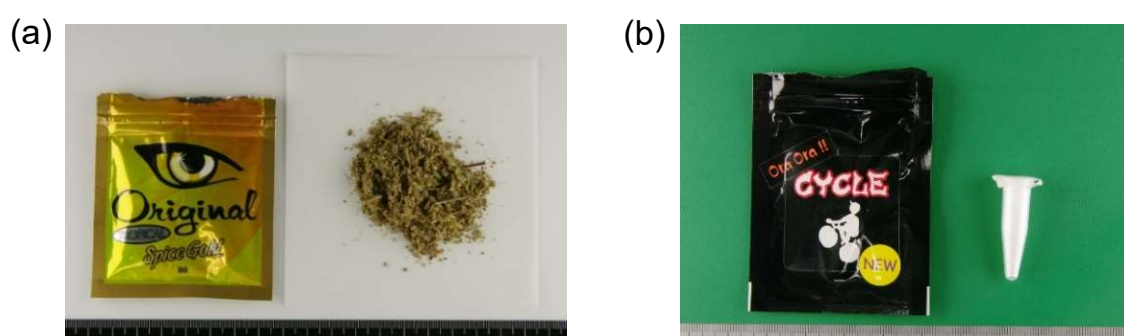


Fig. 1.1 (a) Herbal product containing synthetic cannabinoids and (b) powder containing synthetic cathinones, marketed as ‘Spice’ and ‘bath salt’, respectively.

With recent global trends in drug abuse, NPS distribution has become prevalent in Japan since 2011, increasingly leading to serious health and social concerns [18]. To deter the use of NPSs, the Japanese Ministry of Health, Labor, and Welfare (MHLW) has periodically updated the list of controlled drugs (designated substances) regulated under the Pharmaceutical and Medical Device Act (formerly the Pharmaceutical Affairs Law). However, novel NPSs are continually being developed with slight modifications to the molecular structures of regulated illicit drugs, thereby circumventing existing legal measures. This is akin to a “cat-and-mouse” game between illicit drug developers and regulators [19]. To

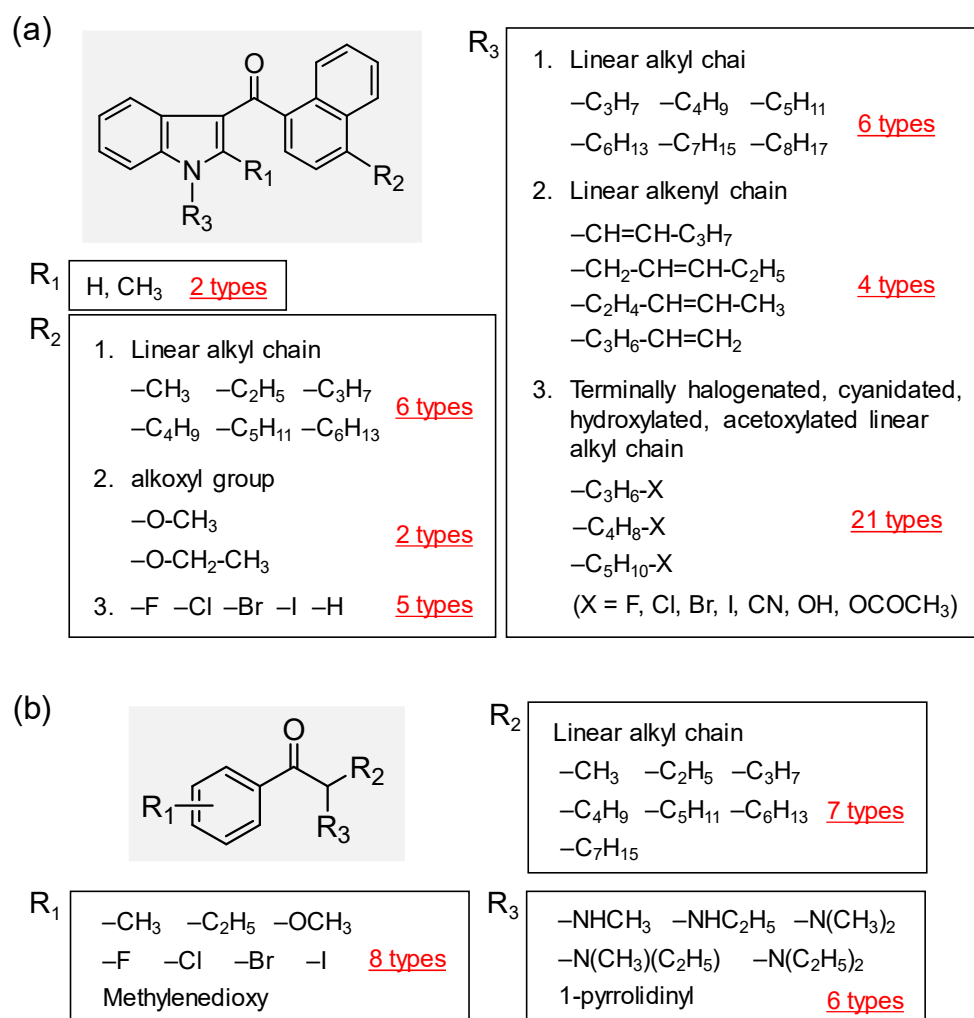


Fig. 1.2 Blanket scheduling of (a) synthetic cannabinoids (enforced in 2013) and (b) synthetic cathinones (enforced in 2014 and 2015) under the Pharmaceutical and Medical Device Act.

resolve this issue, the MHLW has implemented a blanket scheduling of synthetic cannabinoids (enforced in 2013) and synthetic cathinones (enforced in 2014 and 2015) that allows for thorough regulation of compound classes with particular structures. Therefore, 770 synthetic cannabinoids and 1332 synthetic cathinones, as shown in Fig. 1.2, have become subject to illicit drug regulation. Furthermore, following a June 2014 fatal driving incident in Ikebukuro, Tokyo, the government strengthened the regulation and control of NPSs, resulting in the closing of all “head shops” selling NPS products and a gradual decrease of quasi-legal NPS distribution in Japan [20]. However, internet and delivery sales are persistent alternative routes of distribution. New NPSs are now widely created worldwide, and even more harmful drugs are being reported [6,21]. NPSs could be reintroduced to Japan at any moment, necessitating continuous NPS monitoring.

1.2 NPS analysis in forensic science

Analytical methods for NPSs can be broadly divided into simplified and instrumental analyses. Simplified analyses include color tests [22,23], immunoassay screening [24], and thin layer chromatography (TLC) [25]. Instrumental analyses include Fourier transform infrared spectrometry (FT-IR) [26], gas chromatography (GC), liquid chromatography (LC), capillary electrophoresis (CE) [27], and each of these chromatographic/electrophoretic methods coupled with mass spectrometry (MS), that is, GC/MS, LC/MS, and CE/MS. MS commonly utilizes quadrupole (Q), ion trap (IT), and time-of-flight (TOF) principles [28] to separate molecules based on mass and can be used in combination as triple quadrupole (QqQ) [29], Q-TOF [30], or IT-TOF [31]. Recently, orbitrap mass spectrometers, which operate based on the electrodynamic squeezing principle, have been developed and enable ultra-high-resolution analysis with consistent mass accuracy [28,32]. Commonly used MS ionization methods for coupling with GC include electron ionization (EI) and chemical

ionization (CI), whereas electrospray ionization (ESI) and atmospheric pressure chemical ionization (APCI) are more commonly coupled with LC [28]. Based on the guidelines provided by the Scientific Working Group for the Analysis of Seized Drugs (SWGDRUG), which mainly consists of the American Drug Enforcement Administration (DEA), multiple uncorrelated analytical techniques are required to crosscheck the chemical structure of a suspected drug [33]. Furthermore, it is recommended that at least one analytical method that yields direct structural information is included. GC/MS and LC/MS satisfy these requirements as they exhibit high sensitivity and are capable of analyzing samples containing impurities, making them suitable methods for drug analysis.

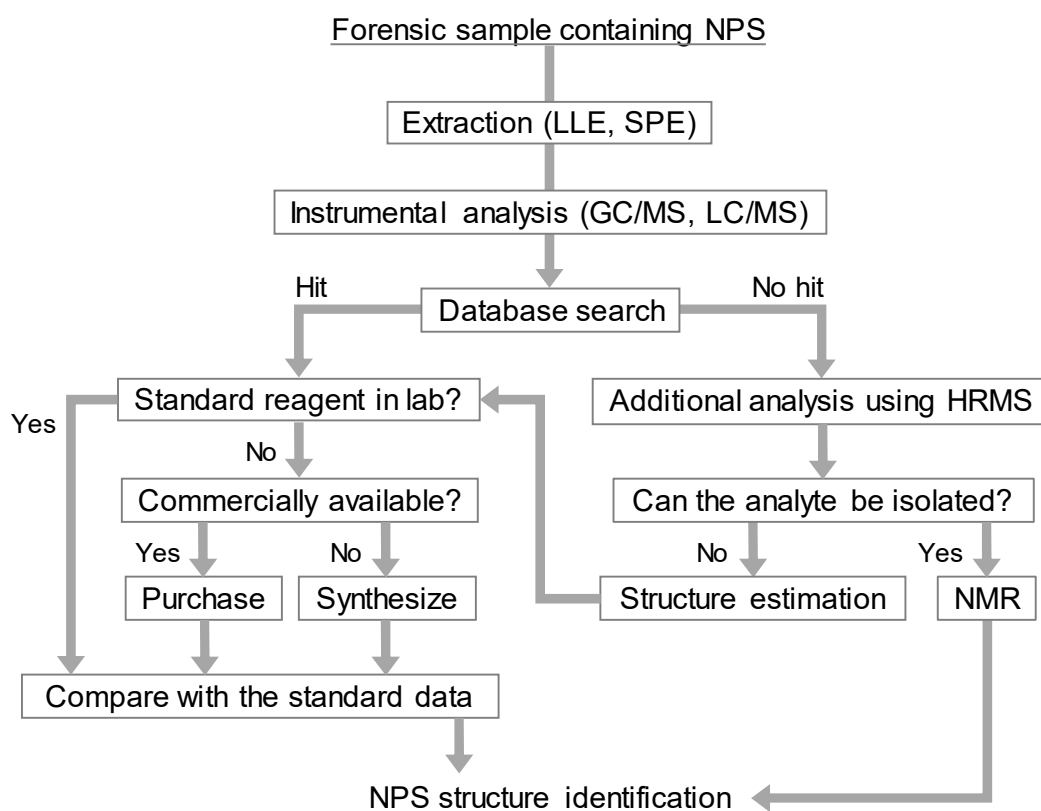


Fig. 1.3 NPS analysis workflow.

A typical NPS analysis workflow is shown schematically in Fig. 1.3. First, the drug in the sample is extracted by using liquid-liquid extraction (LLE) or solid-phase extraction (SPE), which is subsequently analyzed using GC/MS or LC/MS. If the obtained data corresponds with database spectra, the sample is then comparatively analyzed against a reference standard. If the analyte and standard data match, the NPS structure can be conclusively determined. If the reference standard is not available, it must be commercially purchased or synthesized in-house. However, if the obtained data return no database matches, high-resolution mass spectrometry (HRMS) must be performed to obtain the accurate mass of the analyte. If the sample is comprised of a single drug (without significant impurities), nuclear magnetic resonance (NMR) spectroscopy can be used for analyte structure determination. If the sample contains significant impurities, the analyte must be purified using preparative LC or TLC and subsequently analyzed by NMR spectroscopy for structure determination. If insufficient analyte is isolated for NMR analysis, as is the case for many biological samples, the sample is subjected to multiple analytical methods and the chemical structure of the analyte is determined by verification of the consistency of all obtained data from multiple methods. Candidate standards are obtained via purchase or synthesis and comparatively analyzed with the analyte for structure determination. From this workflow, unlike routinely analyzed drugs of abuse, such as MA or MDMA, the positive identification of the chemical structure of unknown NPSs requires many analytical techniques.

1.3 Analytical problems in NPS identification

1.3.1 Continuous emergence of new structural NPSs

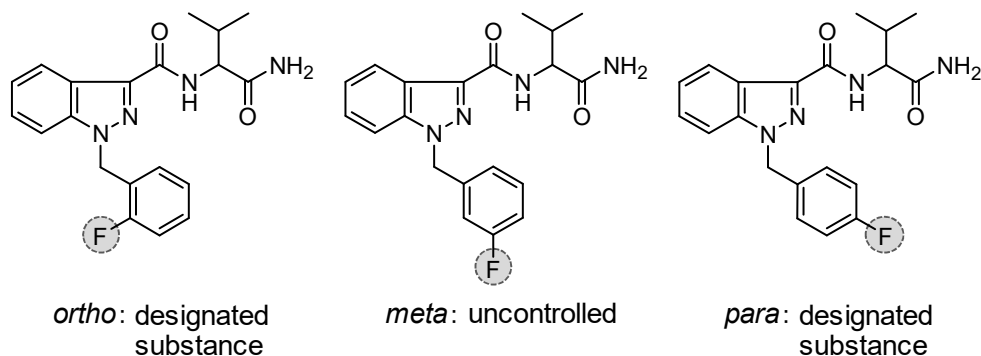
NPSs are continuously created by slightly changing the molecular structure of an illicit drug to avoid legal prosecution. As of June 2019, the number of designed substances has risen to 2378 under the Pharmaceutical and Medical Device Act, of which 855 are synthetic

cannabinoids (36% of all designated substances) and 1353 are synthetic cathinones (57% of all designated substances). Thus, although drug analysis always requires a reference standard of the analyte, preparing this massive number of standard reagents is not practical. Moreover, analytical methods and data of newly emerging NPSs are seldom reported, and their pharmacological activity and metabolism remain unknown. Therefore, NPS identification should be carefully performed based on the data obtained by multiple analytical techniques, considering the possibility of a wide array of chemical structures.

1.3.2 Existence of structurally similar drugs

NPSs include many structural and positional isomers bearing substituents at different positions in the molecular structure [34,35]. Positional isomers of NPSs often cause legal and analytical difficulties. For instance, AB-FUBINACA fluorine positional isomers are separately classified in terms of legislative action (*ortho* and *para*: designated substances, *meta*: uncontrolled) and methylnmethcathinone methyl positional isomers are subject to different laws (*ortho* and *meta*: designated substances, *para*: narcotic) (Fig. 1.4). These legislations necessitate clear determination of the isomeric structures of an analyte. NMR is considered to be the most appropriate method for differentiating isomers, but it is ill-suited for forensic samples because it requires large (mg-scale) sample quantities and be present at non-trace levels. Therefore, forensic analysts often use chromatography and MS as alternative methods. Isomer standard reagents of NPSs are required for isomeric differentiation analysis using these methods, but these standards are rarely commercially available and must be synthesized in-house. These steps represent a time-consuming and financial burden for forensic analysts.

AB-FUBINACA positional isomers



Methylmethcathinone positional isomers

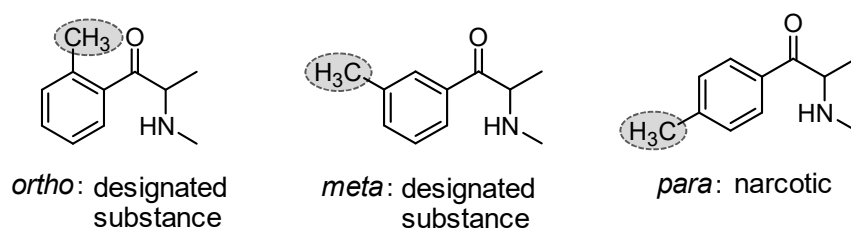


Fig. 1.4 Legal status of positional isomers of AB-FUBINACA and methylmethcathinone.

1.3.3 Structural degradation of NPSs

The storage, extraction, and instrumental analytical conditions may promote NPS decomposition, potentially resulting in missing the analyte or erroneously assigning an improper chemical structure. Some examples of such cases are described below.

- All synthetic cathinones decompose under neutral to basic conditions [36].
- When synthetic cannabinoids containing an ester bond (e.g., 5F-PB-22, QUPIC, and SDB-005) dissolved in alcoholic solutions are subjected to GC, transesterification can occur in the GC inlet.
- Synthetic cannabinoids containing a tetramethylcyclopropyl group (e.g., UR-144, XLR-11, and FUB-144) can be thermally decomposed in the GC inlet [37].
- CHMINACA-BA and BiPICANA cannot be detected by EI-MS.
- Synthetic cathinones are readily thermally decomposed in the GC inlet, yielding

2,3-enamine products [38].

- Synthetic cathinones containing a fluorine group at the *ortho* position of the phenyl ring (e.g., 2-fluoromethcathinone, 2-fluoroethcathinone, and 2-fluoro- α -pyrrolidinopropiophenone) can thermally undergo intramolecular cyclization reactions via HF elimination in the GC inlet [39].
- *t*-Boc-MA and *t*-Boc-MDMA (MA and MDMA attached to *tert*-butoxycarbonyl groups at the N-position) can thermally degrade into MA and MDMA in the GC inlet [40].

1.4 Objectives

Considering the abovementioned issues, NPS analysis requires strict identification of the chemical structure and accurate determination of the applicable legal regulation. However, the *ortho*, *meta*, and *para* ring-fluorinated positional isomers of synthetic cannabinoids and synthetic cathinones exhibit only small differences in retention time and very similar mass spectra patterns, confounding their positive identification. Herein, a novel and practical analytical method to unambiguously and reliably differentiate the ring-fluorinated positional isomers was developed utilizing energy-resolved mass spectrometry (ERMS) (Chapters 2–5). The usefulness of derivatization method with a Triton B-mediated one-pot reaction for differentiating the ring-fluorinated synthetic cathinone positional isomers was also demonstrated (Chapter 6). Conventional pretreatment methods for the extraction of synthetic cathinones, like hydrophilic polymer-based SPE and LLE, does not exclude the biological matrices sufficiently and processes a risk of target analyte decomposition. To address this issue, a class-selective sample clean-up method for the extraction of synthetic cathinones from urine and whole blood samples, was developed using a molecularly imprinted polymer (Chapter 7).

Chapter 2

Differentiation of AB-FUBINACA positional isomers by the abundance of product ions using electron ionization-triple quadrupole mass spectrometry

2.1 Introduction

Synthetic cannabinoids are full agonists to the CB₁ and CB₂ cannabinoid receptors and elicit cannabimimetic effects similar to THC [41–43]. Synthetic cannabinoids have prevailed globally since herbal mixtures, referred to as “Spice” or “K2”, were first marketed as legal natural products [44], resulting in numerous serious incidents involving individuals under their influence. To immediately deter the epidemic of drug abuse, many countries have increased the number of individually named controlled substances. However, structurally distinct NPSs aimed at circumventing such legal measures have continued to be synthesized. In an attempt to address worldwide social concerns, the UK government has implemented a blanket scheduling of synthetic cannabinoids through the introduction of generic legislation based on modifications to core structures, as recommended by the UK home office from the Advisory Council on the Misuse of Drugs (ACMD) in 2009 [45]. However, this regulation did not deter the prevalence of synthetic cannabinoids. Indeed, according to reports from the Forensic Early Warning System (FEWS) in 2012, noncontrolled synthetic cannabinoids such as AM2201, RCS-4, and UR-144, so-called “second-generation” synthetic cannabinoids, were frequently detected in forensic seizures [46–48].

A new designer indazole-type synthetic cannabinoid drug bearing a 4-fluorobenzyl group at the N-1 position, *N*-(1-amino-3-methyl-1-oxobutan-2-yl)-1-(4-fluorobenzyl)-1*H*-indazole-3-carboxamide (AB-FUBINACA), which circumvents such blanket laws, was first identified in Japan from herbal products [49,50]. It was developed and patented by Pfizer Inc. as an

agonist to the CB₁ receptor, which has a much higher affinity for this receptor ($K_i = 0.9$ nM) than THC ($K_i = 41$ nM) [51]. AB-FUBINACA was one of the most identified components of herbal products in early 2012, and was subsequently scheduled as a “designated substance” under the Pharmaceutical and Medical Device Act in December 2012 in Japan, and its 2-fluorobenzyl (*ortho*) isomer was added to the law in December 2015. In the United States, AB-FUBINACA and its *ortho* and 3-fluorobenzyl (*meta*) isomers were all listed as schedule I narcotics in February 2014. These laws require an ability to clearly determine the isomeric structures of an analyte. In this regard, NMR is considered to be the most appropriate instrument to determine the structures of analytes, but it is unsuitable for forensic samples because of their minute amounts or high levels of impurities. GC/MS was often employed as an alternative method, which makes it possible to analyze small and impure samples and provides abundant structural information because of the occurrence of various fragment ions. So far, several research groups have discriminated isomers of abused drugs by the difference of retention time and/or the occurrence of fragment ions using GC/MS [52–59]. However, the three AB-FUBINACA isomers exhibit similar retention properties and give identical fragment ions in mass spectra [60]. Such legal and analytical difficulties prompted to obtain reliable evidence for differentiation of the positional isomers. To this end, we utilized GC/EI-QqQ-MS in product ion scan mode for the three AB-FUBINACA positional isomers and investigated the abundances of the product ions as a function of collision energy (CE), so-called “energy-resolved mass spectrometry (ERMS)” [61–63], whose technique can help to interpret the structures of various compounds, including steroids [64], disaccharides [65], oligosaccharides [66,67], and *N*-glycans [68]. We found significant differences in the abundances of the two characteristic product ions among the three isomers attributed to differences in bond dissociation reactivities. This is the first study on positional isomer differentiation of synthetic cannabinoids based on the ERMS methodology.

2.2 Material and Methods

2.2.1 Reagents

AB-FUBINACA and its 2-fluorobenzyl (*ortho*) and 3-fluorobenzyl (*meta*) isomers were purchased from Cayman Chemical (Ann Arbor, MI, USA). Standard stock solutions of the AB-FUBINACA positional isomers were prepared in methanol at concentrations of 200 $\mu\text{g}/\text{mL}$ and were stored at -20°C prior to use. The working standard solutions for the injections into the mass spectrometer (20 $\mu\text{g}/\text{mL}$) were prepared by diluting the stock solutions.

2.2.2 Instrumentation

Mass spectra were obtained by a SCION TQ triple quadrupole mass spectrometer (Bruker Daltonics, Billerica, MA, USA) with fused-silica capillary columns BR-5ms (30 m \times 0.25 mm i.d., 0.25- μm film thickness; Bruker Daltonics). The inlet temperature was set at 200°C . The injection mode was splitless. Sample injection volume was 1 μL . The carrier gas was high-purity helium (six nine-grade) at a constant column flow rate of 45.1 cm/s. The temperature program for full scan mode consisted of an initial temperature at 80°C held for 1 min, ramped up to 300°C at $10^\circ\text{C}/\text{min}$ followed by a hold at 300°C for 15 min. The temperature program for product ion scan mode consisted of an initial temperature at 200°C held for 1 min, ramped up to 300°C at $10^\circ\text{C}/\text{min}$ followed by a hold at 300°C for 10 min. The transfer line was maintained at 280°C . The mass spectrometer was operated in EI mode at 70 eV using an ion source temperature of 230°C . The acquisition of full scan mode was in the range of m/z 40–600. The acquisition of product ion scan mode was in the range of m/z 40–109, 40–253 and 40–324 for the precursor ions at m/z 109, 253 and 324, respectively. Argon gas pressure on the collision-induced dissociation (CID) was set at 1.5 mTorr.

2.2.3 Principle of energy-resolved mass spectrometry

Mass spectrometers equipped with CID enabled the observation of product ions produced by fragmentation of a precursor ion. ERMS is an analytical method where product ion data as a function of CE can be obtained on a chromatographic timescale, potentiating detailed tracking of activation-induced ion dissociation behavior. Triple quadrupole mass spectrometers were used to perform ERMS for the precursor ions containing a positional isomeric moiety (Fig. 2.1). Dissociation energy depends on the molecular structure of the ion, and the yields of the product ions differ between positional isomer analytes. Herein, the yields of the obtained product ions were quantitatively evaluated and compared between NPS positional isomers.

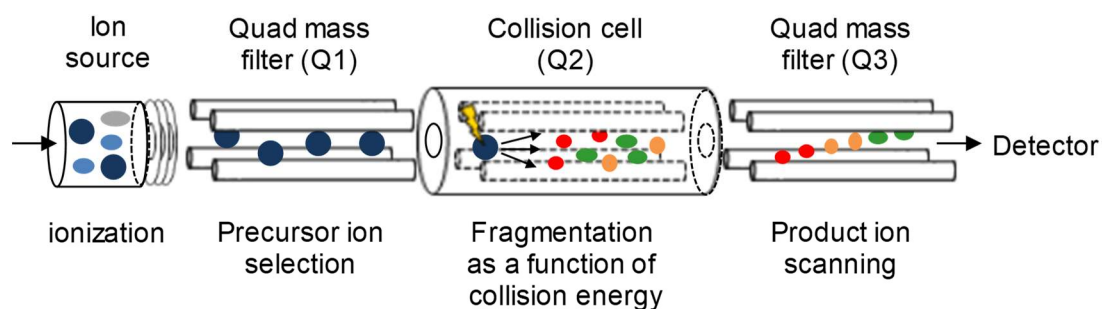


Fig. 2.1 ERMS principle using a triple quadrupole mass spectrometer in product ion scan mode.

2.2.4 Breakdown curve fittings

The abundances of selected ions in the product ion spectra were taken as the areas of the mass chromatographic peaks to avoid the effect of spectral skewing. The plots of the abundances against CEs were fitted with the Boltzmann sigmoidal function with nonlinear regression analysis using KaleidaGraph Ver. 3.52 (Synergy Software, Reading, PA, USA) [66].

$$y = \frac{a}{1+e^{[(b-x)/c]}} \quad (\text{growth})$$

$$y = \frac{a}{1+e^{[-(b-x)/c]}} \quad (\text{decay})$$

where the parameters a , b , and c denote the maximum response, half the maximum response and the slope, respectively.

2.2.5 Statistical and theoretical calculations

Statistical analysis was performed using Microsoft Excel 2010. One-way analysis of variance (ANOVA) was used to determine whether there were any significant differences among the three isomers and was followed by multiple pairwise comparisons as post hoc analysis using Ryan's method [69].

Quantum chemical calculations were performed with Gaussian 09 Rev. D (Gaussian, Inc., Wallingford, CT, USA). The geometries of all the studied compounds were optimized using density functional theory (DFT) at the B3LYP/6-31G(d,p) level [70–73]. Each optimized structure was confirmed by frequency calculation to be the true energy minimum with the absence of imaginary vibration frequencies. The self-consistent field convergence required both $< 10^{-6}$ energy change and $< 10^{-8}$ root mean square change in the density matrix. No symmetry constraint was imposed in the optimization. The optimized structures were shown by Winmostar program [74]. The dissociation energy can be given as the difference between the total free energy of the dissociated species and those of the precursor species, including the electronic energy and zero-point corrections generated from a vibrational frequency calculation [75].

2.3 Results and discussion

2.3.1 Full scan mass spectrometry

Figure 2.2 shows EI-full scan mass spectra of the three AB-FUBINACA isomers. All the isomers underwent three main fragmentations. The proposed EI-fragmentation pathways are shown in Fig. 2.3. The fragment ion at m/z 109, which constitutes base peak, corresponds to the fluorobenzyl cation (or fluorotropylium cation) resulting from the cleavage of methylene

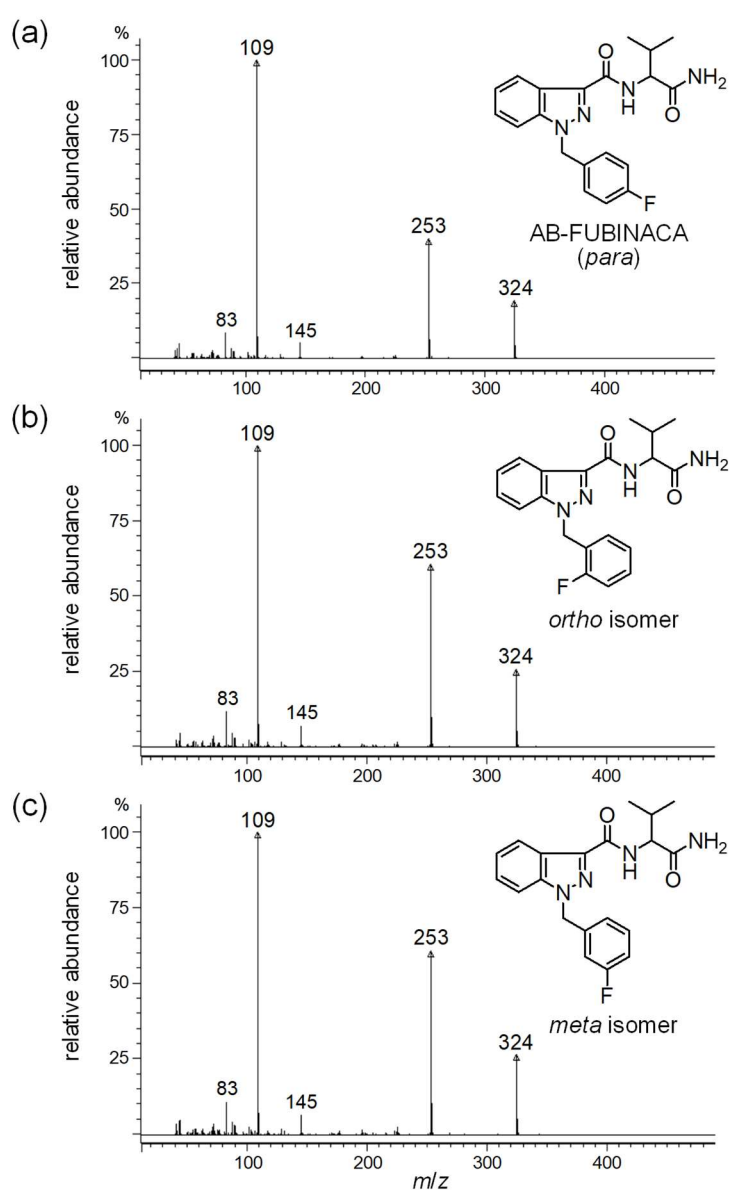


Fig. 2.2 EI-full scan mass spectra of (a) AB-FUBINACA (*para*) and (b) its *ortho* and (c) *meta* isomers.

linkage between the indazole moiety and the fluorobenzyl group. The second-most abundant fragment ion at m/z 253 was generated by elimination of $\text{NHCH}i\text{PrCONH}_2$ in the carboxamide side chain. The fragment ion at m/z 324 was formed by elimination of CONH_2 at the side chain end. The minor fragment ions at m/z 83 and 145 occurred via elimination of acetylene from the m/z 109 ion and via elimination of the fluobenzyl group from the m/z 253 ion, respectively. Although the relative abundances of the AB-FUBINACA ions at m/z 253 and 324 were slightly less than those of the *ortho* and *meta* isomers, the three spectra were highly similar to each other. Therefore, full scan mass spectra were unsuitable for differentiation.

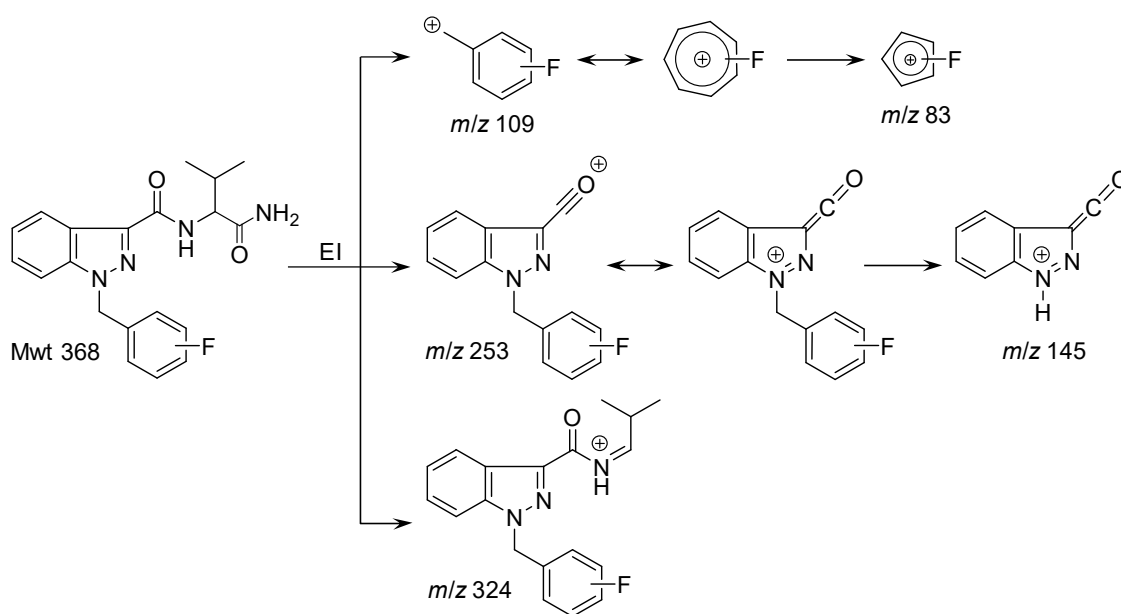


Fig. 2.3 Proposed fragmentation pathways of the AB-FUBINACA isomers by EI.

2.3.2 Energy-resolved mass spectrometry

To differentiate the three isomers, ERMS was performed in product ion scan mode for the precursor ions at m/z 109, 253 and 324. The CE was set at 5, 10, 20, 30, 40 and 50 eV. All of the obtained spectra are shown in Figs 2.4–2.6. The spectra for the precursor ion at m/z 109 were difficult to distinguish at any CE (Fig. 2.4). In the spectra for the precursor ion at m/z 253 (Fig. 2.5), the relative abundance of the ion at m/z 109 at CE of 10 eV varied among the three isomers in the order *meta* < *ortho* < AB-FUBINACA (*para*), indicating that the yield of the fluorobenzyl cation depends on the difference of the fluorine substitution position on the phenyl ring, although the difference between the *ortho* and *meta* isomers was slight. The spectral patterns at 5, 20, 30, 40 and 50 eV were similar. In the spectra for the precursor ion at m/z 324 (Fig. 2.6), the relative abundance of the AB-FUBINACA ion at m/z 109 at 10 eV was higher than those of the *ortho* and *meta* isomers. The spectral patterns of the three isomers at 20 eV clearly differed in the relative abundance of the m/z 109 ion in the order *meta* < *ortho* < *para*. The relative abundance of the AB-FUBINACA ion at m/z 253 at 30 eV was slightly lower than those of the *ortho* and *meta* isomers. The spectral patterns of the three isomers at 5, 40 and 50 eV were almost identical to each other.

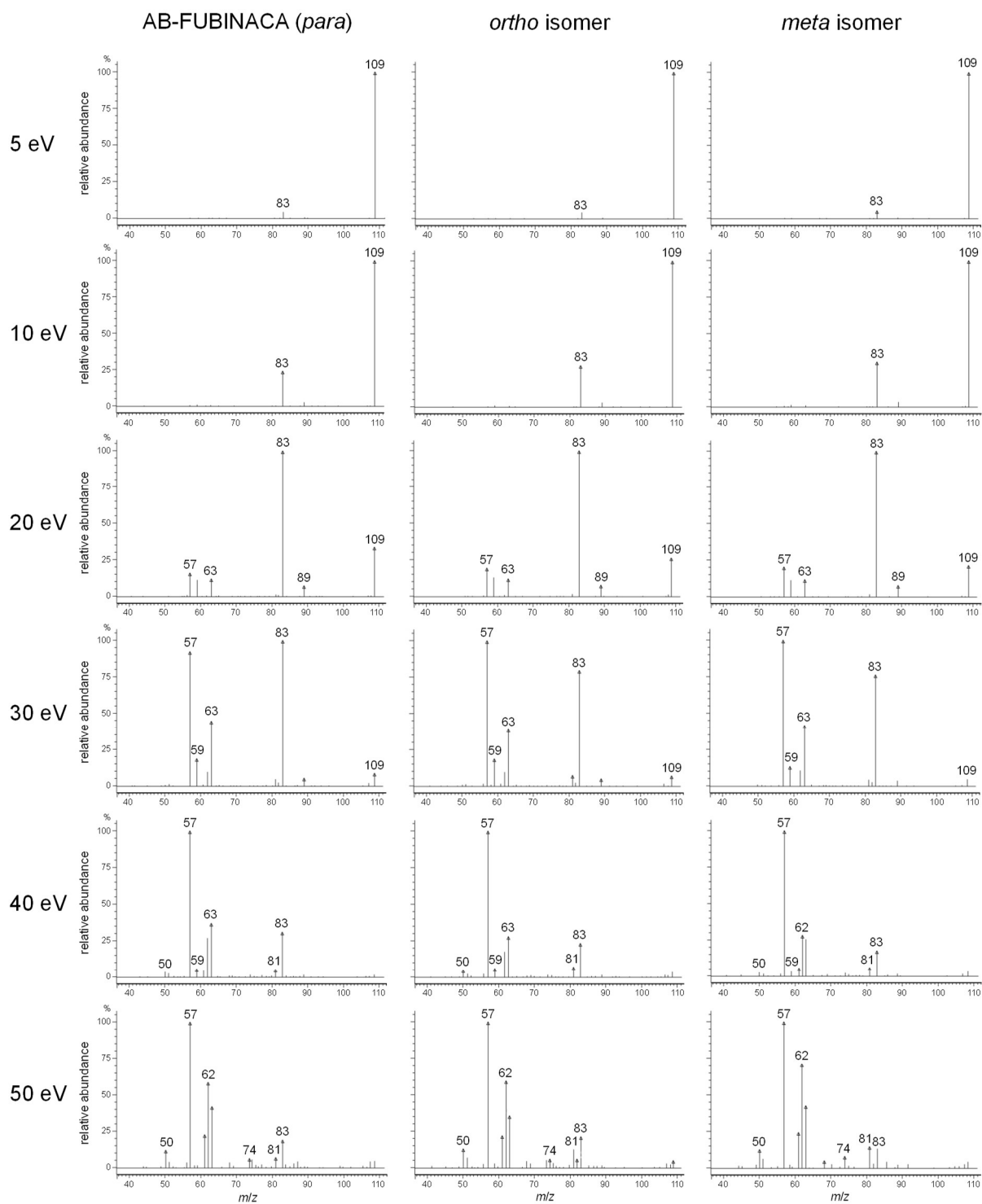


Fig. 2.4 Product ion spectra for the precursor ion at m/z 109. The CE was set at 5, 10, 20, 30, 40, and 50 eV.

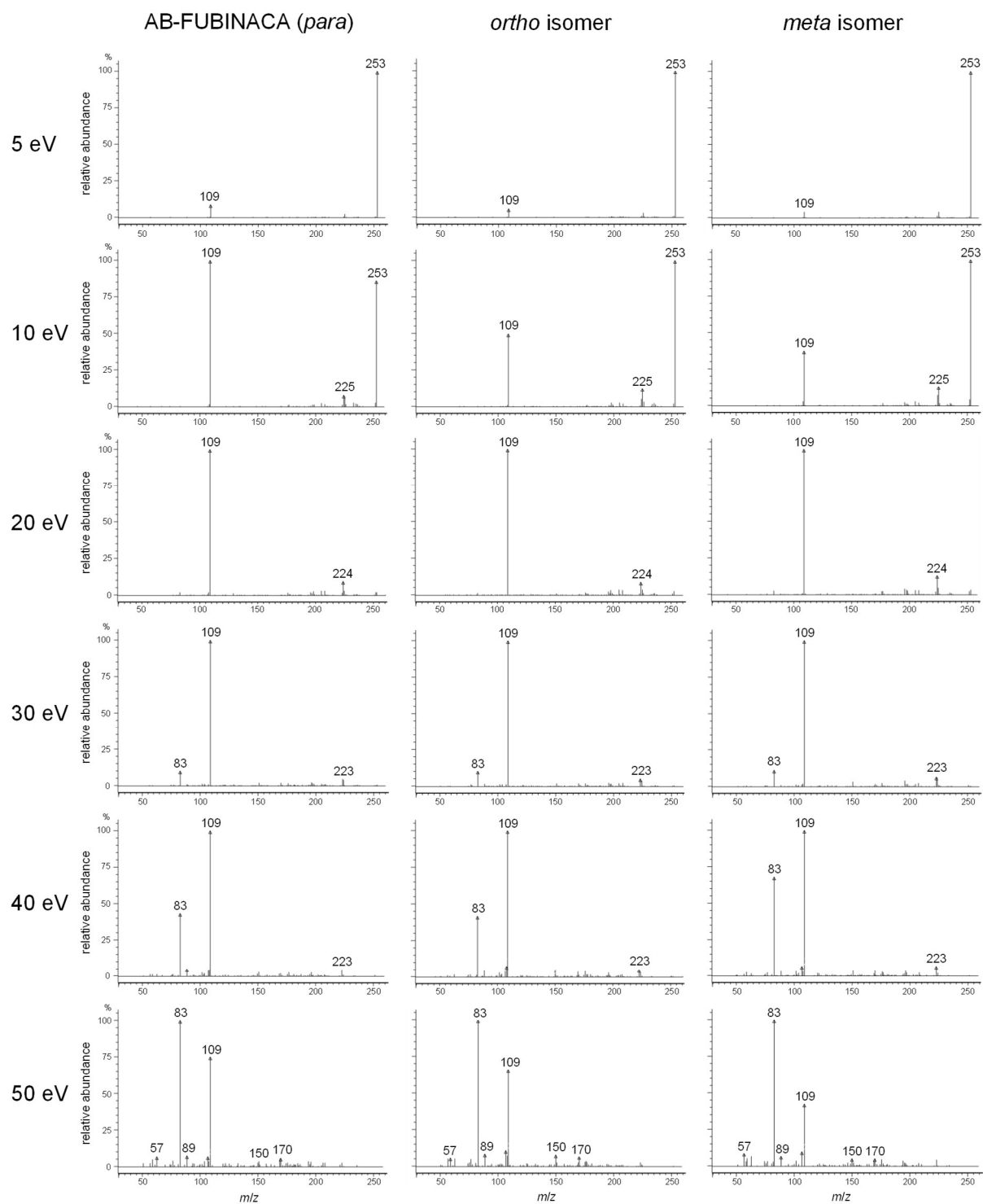


Fig. 2.5 Product ion spectra for the precursor ion at m/z 253. The CE was set at 5, 10, 20, 30, 40, and 50 eV.

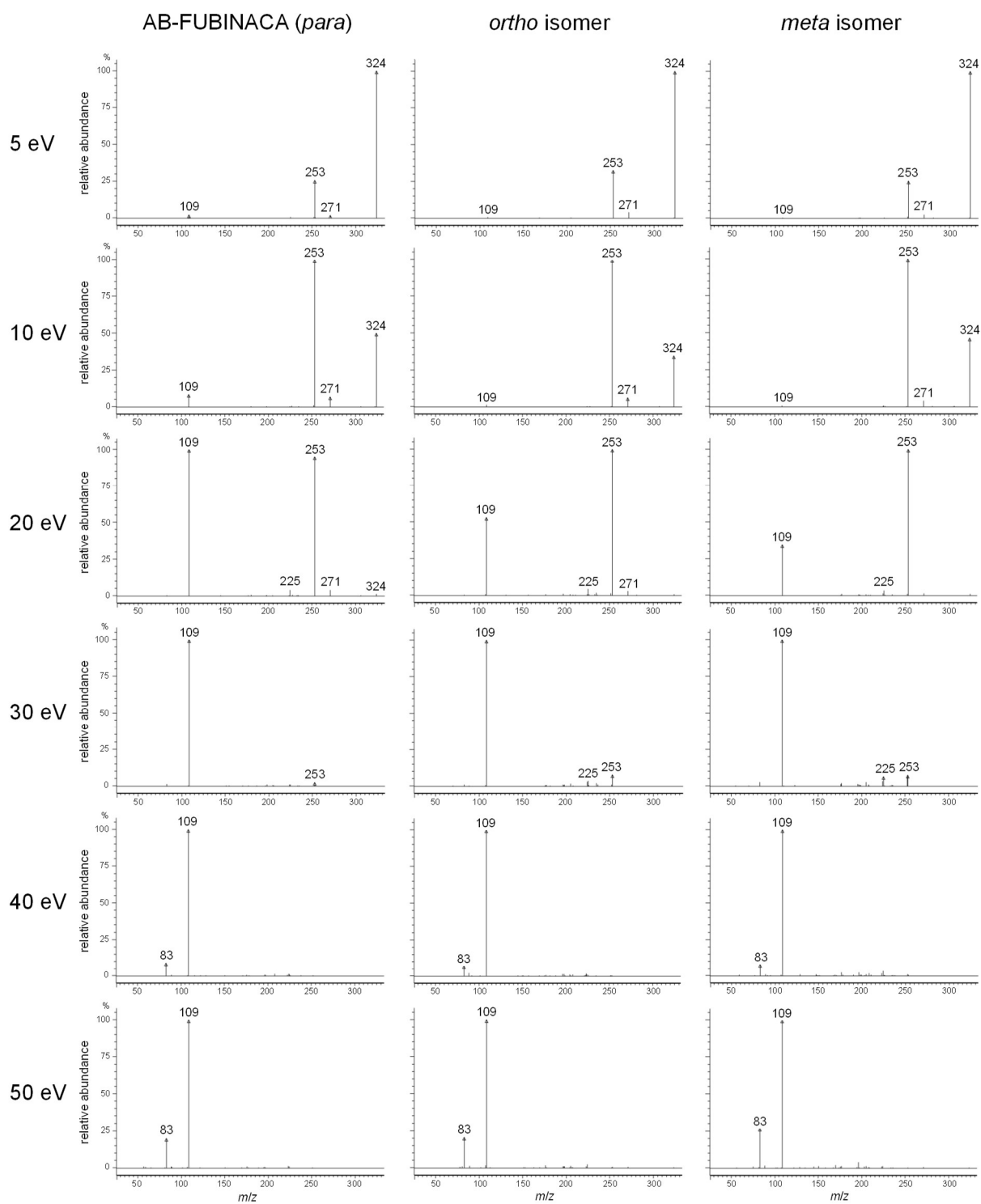


Fig. 2.6 Product ion spectra for the precursor ion at m/z 324. The CE was set at 5, 10, 20, 30, 40, and 50 eV.

2.3.3 Positional isomer differentiation based on product ion abundances

Based on the aforementioned results, the key ions for differentiation appear to be m/z 109 and 253. To better understand the behaviors of the product ions, ERMS was also performed with CE setting varying from 12 to 28 eV in increments of 2 eV. The precursor ion was set at

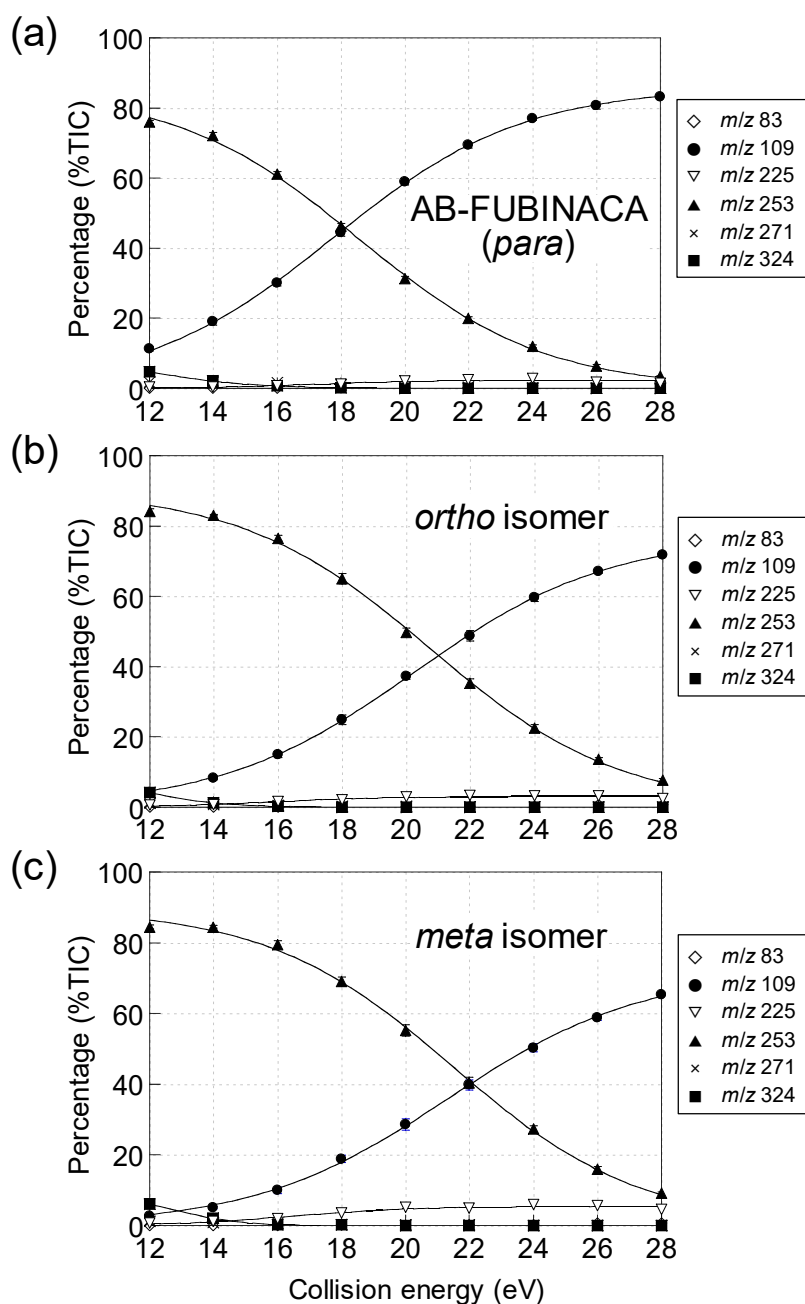


Fig. 2.7 Breakdown curves of (a) AB-FUBINACA (*para*), (b) its *ortho*, and (c) *meta* isomers in the CE range of 12–28 eV. The precursor ion was set at m/z 324. Error bars of the ions at m/z 109 and 253 represent standard errors ($n = 5$).

m/z 324. The abundance of a selected ion, expressed as a percentage of the total ion current (%TIC), was plotted against CE to yield “breakdown curve” (Fig. 2.7). The decomposition of the m/z 324 ion almost always produced the two ions at m/z 109 and 253. Small amounts of the product ions at m/z 83, 225, and 271 were generated at various CEs. The ion intensity at m/z 109 and 253 increased and decreased with increasing CE, respectively. The increment of m/z 109 was almost equal to the decrement of m/z 253, indicating that the generation of the m/z 109 ion resulted from the cleavage of the m/z 253 ion. Although the three breakdown curve patterns were apparently similar, the CE values on the intersection point of the sigmoidal-shaped growth (m/z 109) and decay (m/z 253) curves were different among the three isomers. These results were guaranteed by high reproducibility of mass spectral data. The standard deviations of the two key ions at m/z 109 and 253, determined by the variabilities of the abundances (%TIC) at each CE, were < 1.1 and < 1.1 for intraday, and < 1.0 and < 0.9 for interday, respectively ($n = 5$, Tables 2.1 and 2.2).

Table 2.1 Standard deviations determined by intraday variability of the abundances (%TIC) of the m/z 109 and 253 ions at each CE ($n = 5$).

CE (eV)	AB-FUBINACA		<i>ortho</i> isomer		<i>meta</i> isomer	
	m/z 109	m/z 253	m/z 109	m/z 253	m/z 109	m/z 253
12	0.3	0.5	0.1	0.6	0.1	0.1
14	0.2	0.3	0.3	0.7	0.2	0.2
16	0.3	0.3	0.7	0.8	0.3	0.5
18	0.5	0.5	1.0	1.1	0.3	0.4
20	0.3	0.4	1.0	1.1	0.5	0.7
22	0.5	0.1	1.0	0.8	0.5	0.7
24	0.5	0.4	0.7	0.7	0.5	0.5
26	0.7	0.2	0.9	0.4	0.4	0.5
28	0.7	0.3	1.1	0.5	0.4	0.3

Table 2.2 Standard deviations determined by interday variability of the abundances (%TIC) of the m/z 109 and 253 ions at each CE ($n = 5$).

CE (eV)	AB-FUBINACA		<i>ortho</i> isomer		<i>meta</i> isomer	
	m/z 109	m/z 253	m/z 109	m/z 253	m/z 109	m/z 253
12	0.1	0.3	0.2	0.9	0.5	0.3
14	0.5	0.5	0.3	0.5	0.4	0.6
16	0.6	0.6	0.4	0.9	0.5	0.7
18	0.3	0.3	0.8	0.9	0.5	0.7
20	0.4	0.3	0.8	0.9	0.6	0.8
22	0.5	0.5	0.8	0.8	0.6	0.9
24	0.3	0.2	0.7	0.6	0.9	0.9
26	0.5	0.2	0.9	0.5	0.9	0.7
28	0.2	0.1	0.7	0.6	1.0	0.5

To make the difference clearer, the natural logarithmic values of the abundance ratio of the m/z 109 ion to the 253 ion [$\ln(A_{109}/A_{253})$], assuming that CID reaction was quantitatively occurred in accordance with Gibbs free energy equation, were plotted against the CE. The $\ln(A_{109}/A_{253})$ values showed the relation of *meta* < *ortho* < *para* at any CE (Fig. 2.8), and thus it suggested that the three isomers required different energies for cleaving the fluorobenzyl group from the indazole moiety. In addition, the $\ln(A_{109}/A_{253})$ values for each isomer were linearly related to the CE with high correlation coefficients, decisively separating the three approximation lines (Fig. 2.8). One-way ANOVA showed that the $\ln(A_{109}/A_{253})$ values of the three isomers were significantly different at each CE (significance $\alpha < 9.0 \times 10^{-7}$; Table 2.3), indicating that the within-sample variances were much smaller than the between-sample variances (F value), and multiple pairwise comparisons showed low p values ($< 1.4 \times 10^{-2}$) at each CE, revealing that the differences in the $\ln(A_{109}/A_{253})$ values of the three isomers were statistically significant. A comparison of $\ln(A_{109}/A_{253})$ values at various CEs allowed the three isomers to be more clearly and more reliably differentiated than a comparison of only values at a certain CE.

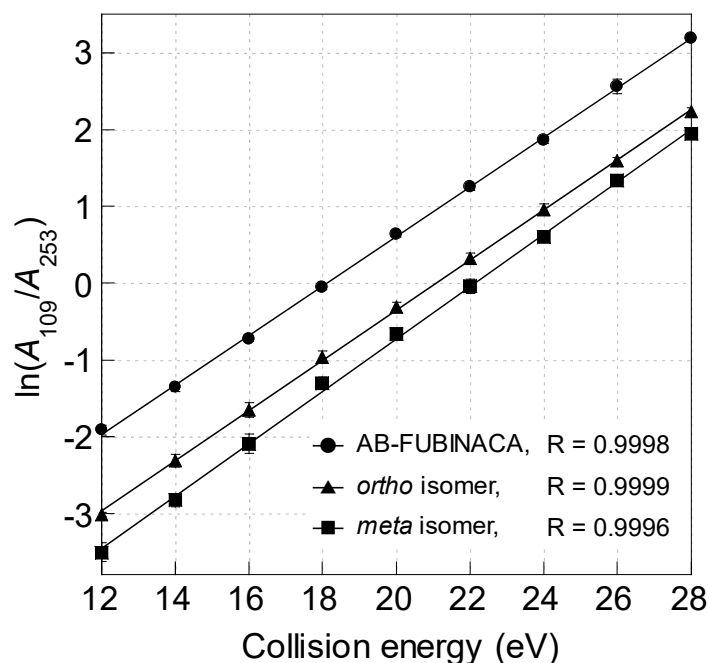


Fig. 2.8 Logarithmic plots of the abundance ratio of the m/z 109 ion to the 253 ion for the precursor ion at m/z 324. Error bars represent standard errors ($n = 5$).

Table 2.3 One-way analysis of variance (ANOVA) and multiple pairwise comparisons for logarithmic values of the abundance ratio of the ion at m/z 109 to m/z 253 [$\ln(A_{109}/A_{253})$] for the precursor ion at m/z 324 of the AB-FUBINACA positional isomers.

CE (eV)	One-way ANOVA		Multiple pairwise comparisons (p)		
	F value	Significance (α)	$para \times ortho$	$para \times meta$	$ortho \times meta$
12	98.8	3.5×10^{-8}	1.4×10^{-5}	2.1×10^{-4}	1.4×10^{-2}
14	96.2	4.1×10^{-8}	4.2×10^{-5}	6.5×10^{-5}	1.6×10^{-3}
16	55.1	9.0×10^{-7}	1.7×10^{-4}	4.7×10^{-4}	1.0×10^{-3}
18	92.0	5.3×10^{-8}	7.0×10^{-5}	3.4×10^{-5}	8.2×10^{-6}
20	133	6.6×10^{-9}	2.5×10^{-5}	3.9×10^{-5}	3.8×10^{-4}
22	90.8	5.7×10^{-8}	5.2×10^{-5}	8.5×10^{-5}	3.6×10^{-4}
24	129	7.8×10^{-9}	2.1×10^{-5}	5.4×10^{-6}	3.8×10^{-3}
26	91.4	5.5×10^{-8}	3.4×10^{-4}	1.3×10^{-4}	7.3×10^{-3}
28	196	6.8×10^{-10}	1.8×10^{-5}	7.1×10^{-5}	3.8×10^{-4}

Similar results were obtained for the precursor ion at m/z 253 (Figs 2.9 and 2.10, and Table 2.4). Although, in the case of isomeric mixture, the AB-FUBINACA isomers could not be baseline separated on the chromatographic analysis using BR-5ms column (Fig. 2.11), the fluorine-substituted position of each isomer was able to be identified by comparing the

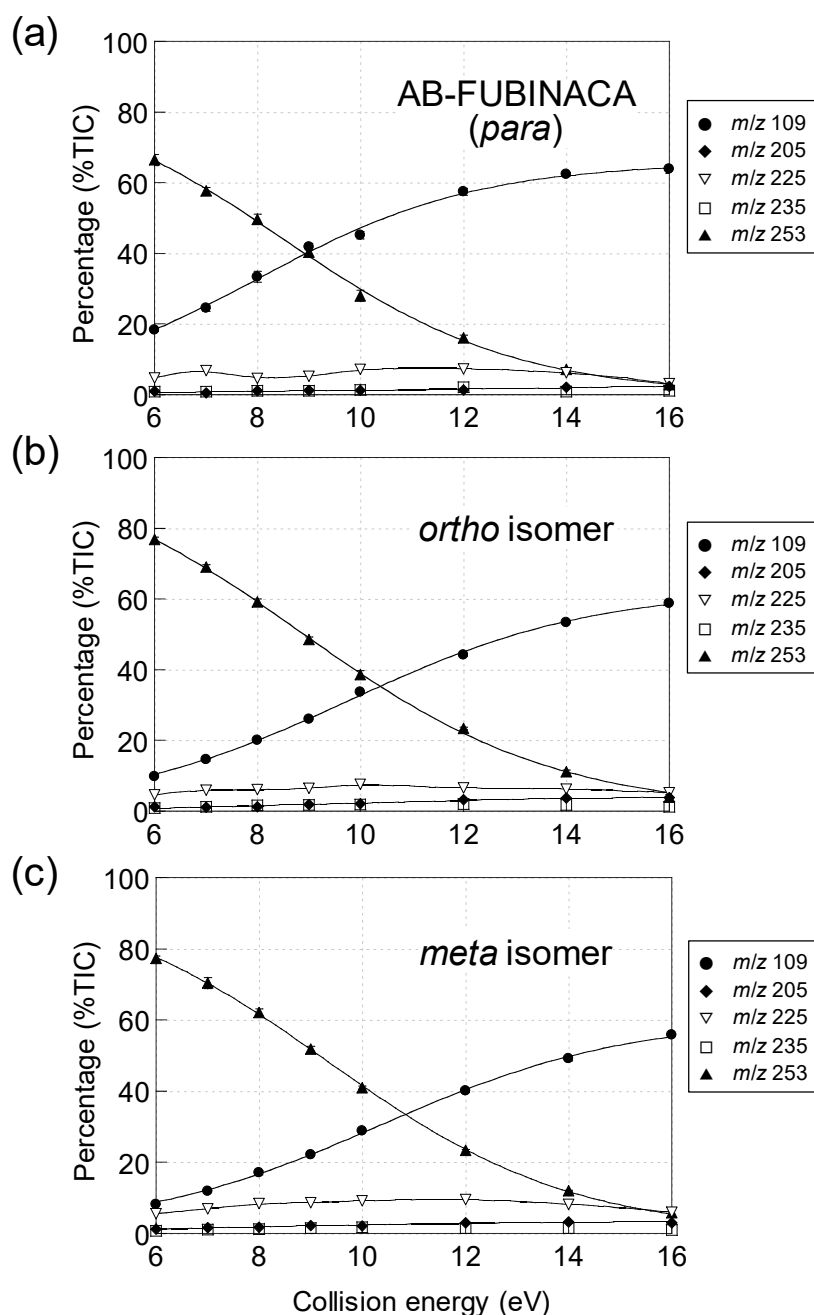


Fig. 2.9 Breakdown curves of (a) AB-FUBINACA (*para*), (b) its *ortho*, and (c) *meta* isomers in the CE range of 6–16 eV. The precursor ion was set at m/z 253. Error bars of the ions at m/z 109 and 253 represent standard errors ($n = 5$).

$\ln(A_{109}/A_{253})$ values extracted from the mass spectra at non-overlapping parts on adjacent peaks in chromatogram.

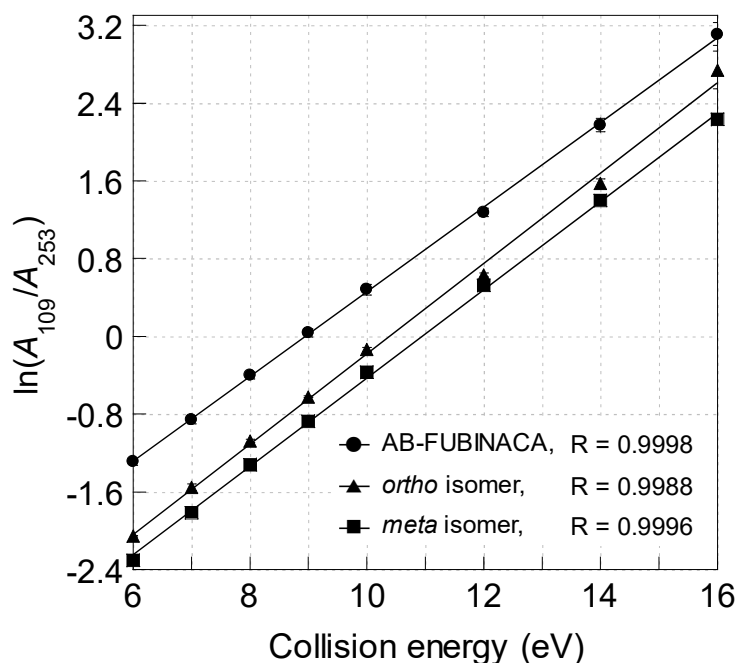


Fig. 2.10 Logarithmic plots of the abundance ratio of the m/z 109 ion to the 253 ion for the precursor ion at m/z 253. Error bars represent standard errors ($n = 5$).

Table 2.4 One-way analysis of variance (ANOVA) and multiple pairwise comparisons for logarithmic values of the abundance ratio of the ion at m/z 109 to m/z 253 [$\ln(A_{109}/A_{253})$] for the precursor ion at m/z 253 of the AB-FUBINACA positional isomers.

CE (eV)	One-way ANOVA		Multiple pairwise comparisons (p)		
	F value	Significance (α)	<i>para</i> \times <i>ortho</i>	<i>para</i> \times <i>meta</i>	<i>ortho</i> \times <i>meta</i>
6	546	1.6×10^{-12}	3.2×10^{-5}	3.6×10^{-6}	1.3×10^{-4}
7	262	1.3×10^{-10}	3.4×10^{-4}	3.5×10^{-5}	2.9×10^{-3}
8	242	2.0×10^{-10}	1.3×10^{-4}	3.2×10^{-4}	2.7×10^{-3}
9	346	2.5×10^{-11}	7.2×10^{-5}	1.2×10^{-4}	2.5×10^{-4}
10	157	2.5×10^{-9}	1.6×10^{-3}	5.0×10^{-4}	4.0×10^{-4}
12	213	4.2×10^{-10}	2.7×10^{-4}	2.3×10^{-4}	9.0×10^{-3}
14	71.1	2.2×10^{-7}	5.0×10^{-3}	7.5×10^{-4}	4.9×10^{-2}
16	11.2	1.8×10^{-3}	3.8×10^{-1}	2.3×10^{-3}	1.0×10^{-1}

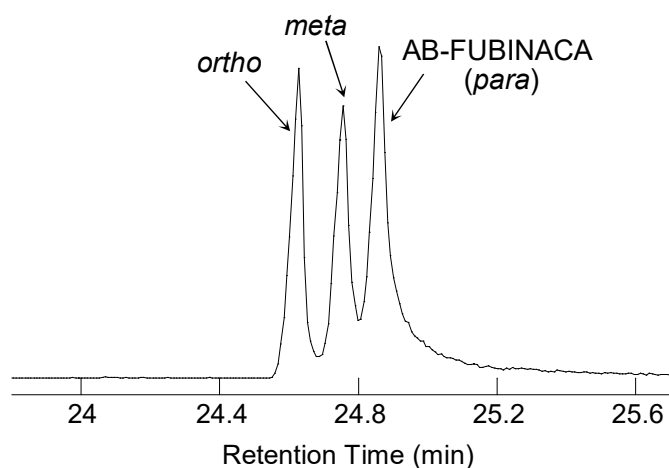


Fig. 2.11 Total ion current chromatogram of the mixture of three AB-FUBINACA isomers. Column, BR-5ms; acquisition mode, product ion scan; precursor ion, m/z 324; column temperature program, 80°C (1 min)–10°C/min→300°C (15 min).

2.3.4 Theoretical calculations of dissociation energy

DFT calculations are helpful to interpret the experimental results [76]. Free energies of the molecules involved in the cleavage reaction of the m/z 253 ion generated by CID were calculated at the B3LYP/6-31G(d,p) level. Skeletal rearrangements such as the change of benzyl cations to tropylium ions were not considered. The optimized structures, geometries, and calculated free energies of the product ions (*para*, *ortho*, and *meta*- m/z 253, 225, and 109) and neutrals (N144 and N116) are shown in Fig. 2.12, Tables 2.5, and 2.6, respectively.

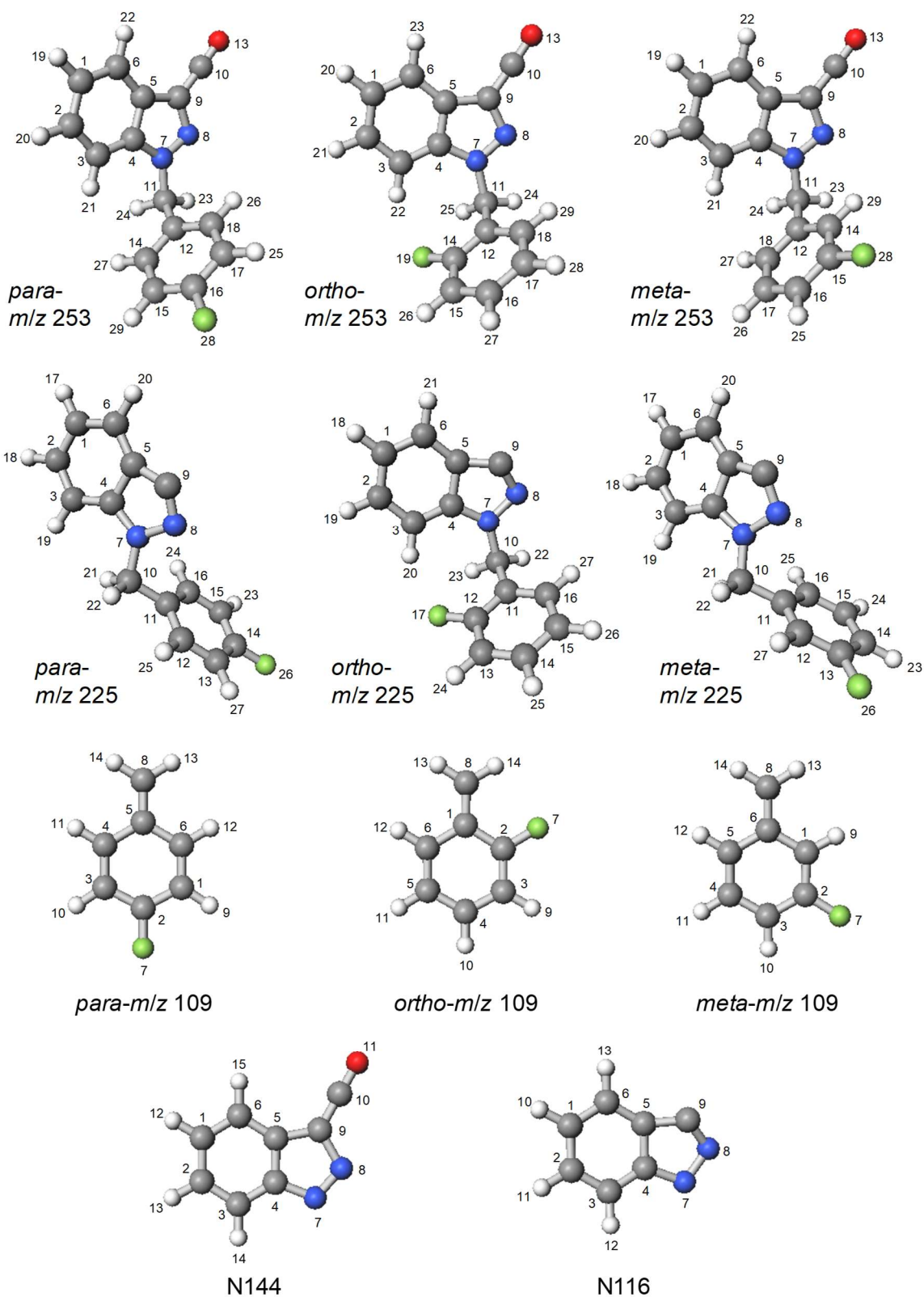


Fig. 2.12 Optimized structures of the *para*, *ortho*, and *meta*-*m/z* 253, 225, and 109 ions and neutrals (N144^a and N116^b) at B3LYP/6-31G(d,p) level.

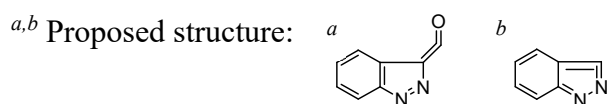


Table 2.5 Geometries of the *para*, *ortho*, and *meta*-*m/z* 253, 225, and 109 ions and neutrals (N144 and N116) at B3LYP/6-31G(d,p) level.

<i>para</i> - <i>m/z</i> 253					<i>ortho</i> - <i>m/z</i> 253					<i>meta</i> - <i>m/z</i> 253				
Center number	Atom	Coordinates [Angstroms]			Center number	Atom	Coordinates [Angstroms]			Center number	Atom	Coordinates [Angstroms]		
		x	y	z			x	y	z			x	y	z
1	C	2.63196	-2.73793	-0.73097	1	C	-2.63492	-2.60325	0.86458	1	C	-2.71980	2.50492	-1.09854
2	C	1.39572	-2.98773	-0.09493	2	C	-1.36276	-2.94832	0.35716	2	C	-1.50983	2.94762	-0.51925
3	C	0.66185	-1.97042	0.49669	3	C	-0.53661	-2.01023	-0.24423	3	C	-0.70292	2.09749	0.22208
4	C	1.21424	-0.68551	0.43085	4	C	-1.03694	-0.70439	-0.31997	4	C	-1.15547	0.78040	0.36606
5	C	2.44859	-0.42495	-0.20576	5	C	-2.30713	-0.34713	0.18661	5	C	-2.36211	0.32654	-0.21218
6	C	3.17628	-1.46143	-0.79860	6	C	-3.12656	-1.30564	0.79027	6	C	-3.16411	1.19598	-0.95811
7	N	0.75089	0.53286	0.92822	7	N	-0.48122	0.45293	-0.86570	7	N	-0.60092	-0.30345	1.04659
8	N	1.54230	1.53525	0.67438	8	N	-1.24504	1.50149	-0.75935	8	N	-1.30964	-1.39272	0.96095
9	C	2.59860	1.00180	-0.02042	9	C	-2.37832	1.06474	-0.11984	9	C	-2.40066	-1.06006	0.19847
10	C	3.60430	1.83518	-0.41619	10	C	-3.37657	1.96282	0.12230	10	C	-3.33429	-2.02299	-0.05593
11	C	-0.51016	0.78076	1.67583	11	C	0.85502	0.59788	-1.50400	11	C	0.67087	-0.32638	1.80960
12	C	-1.73982	0.55204	0.82811	12	C	1.97762	0.61103	-0.49620	12	C	1.88033	-0.14820	0.91699
13	O	4.46446	2.50368	-0.76254	13	O	-4.23322	2.68744	0.34174	13	O	-4.13581	-2.80366	-0.28889
14	C	-2.67969	-0.41773	1.19866	14	C	2.80453	-0.50258	-0.34075	14	C	2.11823	-1.05389	-0.12422
15	C	-3.83617	-0.61235	0.44553	15	C	3.86972	-0.53153	0.54744	15	C	3.25210	-0.88565	-0.90848
16	C	-4.03321	0.17332	-0.68532	16	C	4.11925	0.60410	1.31747	16	C	4.16061	0.14677	-0.68753
17	C	-3.11777	1.14812	-1.07822	17	C	3.31240	1.73912	1.18971	17	C	3.91680	1.03596	0.35652
18	C	-1.97236	1.33572	-0.31193	18	C	2.25246	1.74152	0.28658	18	C	2.77842	0.89716	1.15571
19	H	3.16883	-3.56648	-1.18037	19	F	2.54993	-1.60551	-1.09341	19	H	-3.31621	3.20738	-1.67083
20	H	1.02024	-4.00120	-0.07244	20	H	-3.24384	-3.37364	1.32550	20	H	-1.20360	3.97814	-0.66225
21	H	-0.29399	-2.15801	0.96944	21	H	-1.02306	-3.97482	0.44173	21	H	0.23445	2.42943	0.65081
22	H	4.12615	-1.28560	-1.29155	22	H	0.44502	-2.26922	-0.62162	22	H	-4.09462	0.87121	-1.41066
23	H	-0.42081	1.81149	2.02435	23	H	-4.10554	-1.05632	1.18471	23	H	0.66748	-1.28906	2.32453
24	H	-0.49550	0.11850	2.54570	24	H	0.79631	1.53386	-2.06012	24	H	0.60854	0.46882	2.55693
25	H	-3.31831	1.74512	-1.96060	25	H	0.96008	-0.23007	-2.20660	25	H	5.03488	0.23445	-1.32261
26	H	-1.25986	2.10365	-0.60093	26	H	4.48254	-1.42289	0.61901	26	H	4.61725	1.84151	0.55017
27	H	-2.52380	-1.01514	2.09339	27	H	4.94981	0.60306	2.01558	27	H	2.60590	1.58909	1.97543
28	F	-5.13732	-0.00897	-1.41857	28	H	3.51776	2.62208	1.78503	28	F	3.47611	-1.75071	-1.90798
29	H	-4.57947	-1.35119	0.72242	29	H	1.63393	2.62803	0.17594	29	H	1.45225	-1.88610	-0.32852

Table 2.5 Continued.

<i>para-m/z 225</i>				<i>ortho-m/z 225</i>				<i>meta-m/z 225</i>						
Center number	Atom	Coordinates [Angstroms]			Center number	Atom	Coordinates [Angstroms]			Center number	Atom	Coordinates [Angstroms]		
		x	y	z			x	y	z			x	y	z
1	C	-4.85864	-0.16243	0.52659	1	C	-3.85337	1.17310	-0.74256	1	C	4.88170	-0.01496	-0.22629
2	C	-4.28774	1.12098	0.60523	2	C	-2.79613	1.90158	-0.17069	2	C	4.26658	1.24852	-0.28242
3	C	-2.95161	1.36082	0.27946	3	C	-1.64363	1.27771	0.32156	3	C	2.89347	1.41487	-0.08894
4	C	-2.17419	0.25674	-0.07294	4	C	-1.61466	-0.11126	0.31285	4	C	2.13209	0.26167	0.09999
5	C	-2.76908	-1.04552	-0.19791	5	C	-2.67468	-0.86334	-0.33487	5	C	2.76788	-1.02485	0.20679
6	C	-4.11642	-1.25984	0.09659	6	C	-3.79130	-0.21229	-0.86528	6	C	4.14708	-1.16666	0.04808
7	N	-0.80905	0.13898	-0.38793	7	N	-0.63771	-1.02269	0.75908	7	N	0.74705	0.07388	0.25401
8	N	-0.53386	-1.14929	-0.76042	8	N	-0.98786	-2.26644	0.40504	8	N	0.49100	-1.24286	0.51341
9	C	-1.66978	-1.68210	-0.82654	9	C	-1.94424	-2.05562	-0.43095	9	C	1.63735	-1.73463	0.67795
10	C	0.20662	1.18573	-0.55204	10	C	0.65069	-0.75790	1.43566	10	C	-0.31392	1.07957	0.37793
11	C	1.58192	0.68067	-0.23541	11	C	1.77197	-0.37289	0.50218	11	C	-1.64692	0.54573	-0.06254
12	C	2.58342	0.69335	-1.22257	12	C	2.11596	0.96828	0.32682	12	C	-2.71777	0.52563	0.83565
13	C	3.86373	0.24186	-0.93497	13	C	3.14856	1.37996	-0.50186	13	C	-3.94527	0.04754	0.39491
14	C	4.13102	-0.22552	0.35496	14	C	3.87217	0.40353	-1.18697	14	C	-4.13941	-0.41378	-0.91081
15	C	3.15949	-0.24865	1.36068	15	C	3.55899	-0.95050	-1.03442	15	C	-3.06445	-0.38828	-1.79962
16	C	1.88711	0.20847	1.05879	16	C	2.51839	-1.33497	-0.19115	16	C	-1.82415	0.09163	-1.38647
17	H	-5.89899	-0.29828	0.80000	17	F	1.40251	1.90972	1.00498	17	H	5.95016	-0.09330	-0.39294
18	H	-4.91258	1.95891	0.89546	18	H	-4.73021	1.69957	-1.10239	18	H	4.88095	2.12752	-0.44562
19	H	-2.56413	2.37319	0.24602	19	H	-2.85254	2.98470	-0.14660	19	H	2.45990	2.40704	-0.02557
20	H	-4.54809	-2.25312	0.04342	20	H	-0.77382	1.85266	0.62285	20	H	4.61411	-2.14474	0.08087
21	H	-0.09807	1.97403	0.14835	21	H	-4.61371	-0.78333	-1.28236	21	H	0.01191	1.90416	-0.26932
22	H	0.14460	1.59821	-1.56440	22	H	0.87369	-1.68720	1.97825	22	H	-0.34325	1.45430	1.40636
23	H	3.42138	-0.61139	2.34788	23	H	0.44568	0.04210	2.15185	23	H	-5.11846	-0.77430	-1.20620
24	H	1.12224	0.20678	1.82990	24	H	3.37645	2.43598	-0.59169	24	H	-3.20123	-0.73557	-2.81791
25	H	2.35687	1.05893	-2.21954	25	H	4.68788	0.70290	-1.83672	25	H	-0.99538	0.12485	-2.08706
26	F	5.35659	-0.65821	0.63888	26	H	4.13031	-1.70427	-1.56501	26	F	-4.97273	0.02362	1.24667
27	H	4.65286	0.24139	-1.67796	27	H	2.28232	-2.38792	-0.06365	27	H	-2.61601	0.86675	1.86025

Table 2.5 Continued.

para-m/z 109

Center number	Atom	Coordinates [Angstroms]		
		x	y	z
1	C	-1.24734	-0.68243	0.00000
2	C	0.00000	-1.34529	0.00000
3	C	1.24734	-0.68242	0.00000
4	C	1.24680	0.68674	0.00000
5	C	0.00000	1.42109	0.00000
6	C	-1.24680	0.68673	0.00000
7	F	0.00001	-2.65376	0.00000
8	C	-0.00001	2.78816	0.00000
9	H	-2.15896	-1.26913	0.00000
10	H	2.15895	-1.26913	0.00000
11	H	2.18268	1.23700	0.00000
12	H	-2.18268	1.23700	0.00000
13	H	-0.92642	3.35630	0.00000
14	H	0.92640	3.35631	0.00000

ortho-m/z 109

Center number	Atom	Coordinates [Angstroms]		
		x	y	z
1	C	-0.90226	0.23494	0.00000
2	C	0.00000	-0.89964	0.00000
3	C	1.36890	-0.74246	0.00000
4	C	1.87723	0.56236	0.00000
5	C	1.04510	1.71098	0.00000
6	C	-0.31637	1.55834	0.00000
7	F	-0.53044	-2.10430	0.00000
8	C	-2.25408	0.04308	0.00000
9	H	2.01805	-1.61049	0.00000
10	H	2.95553	0.69620	0.00000
11	H	1.49385	2.69757	0.00000
12	H	-0.98038	2.41714	0.00000
13	H	-2.93906	0.88646	0.00000
14	H	-2.68518	-0.95382	0.00000

meta-m/z 109

Center number	Atom	Coordinates [Angstroms]		
		x	y	z
1	C	0.00000	1.05772	0.00000
2	C	-1.17950	0.35342	0.00000
3	C	-1.18761	-1.05636	0.00000
4	C	0.01179	-1.78999	0.00000
5	C	1.21742	-1.12109	0.00000
6	C	1.23812	0.32184	0.00000
7	F	-2.34188	0.99022	0.00000
8	C	2.43780	0.98793	0.00000
9	H	-0.00550	2.14267	0.00000
10	H	-2.14849	-1.56370	0.00000
11	H	-0.02392	-2.87352	0.00000
12	H	2.15762	-1.66324	0.00000
13	H	2.48609	2.07398	0.00000
14	H	3.38303	0.45112	0.00000

N144

Center number	Atom	Coordinates [Angstroms]		
		x	y	z
1	C	2.07281	-1.54318	-0.00006
2	C	2.81098	-0.34436	-0.00004
3	C	2.17201	0.89099	-0.00003
4	C	0.77491	0.89803	-0.00002
5	C	0.03150	-0.30635	0.00002
6	C	0.67944	-1.54407	-0.00002
7	N	-0.08438	2.00097	0.00028
8	N	-1.30738	1.62240	-0.00046
9	C	-1.32662	0.18369	0.00029
10	C	-2.48622	-0.47772	0.00021
11	O	-3.49760	-1.04633	-0.00011
12	H	2.60232	-2.49115	-0.00004
13	H	3.89549	-0.38926	0.00001
14	H	2.72453	1.82439	0.00006
15	H	0.12796	-2.47908	0.00004

N116

Center number	Atom	Coordinates [Angstroms]		
		x	y	z
1	C	-2.12800	-0.58724	0.03950
2	C	-1.98934	0.81474	-0.01990
3	C	-0.73668	1.42472	-0.06101
4	C	0.38669	0.60435	0.03825
5	C	0.24242	-0.81741	0.06174
6	C	-1.01633	-1.42474	0.03273
7	N	1.75122	0.98740	0.06091
8	N	2.47518	-0.15443	0.10795
9	C	1.60243	-1.05325	-0.26901
10	H	-3.12242	-1.01997	0.08016
11	H	-2.88300	1.42969	-0.06454
12	H	-0.62293	2.49661	-0.19150
13	H	-1.12356	-2.50416	0.06000

Table 2.6 Calculated free energies (kcal/mol) of the product ions (*para*, *ortho*, and *meta*-*m/z* 253, 225, and 109) and neutrals (N144 and N116).

Compound	<i>Para</i>	<i>Ortho</i>	<i>Meta</i>
<i>m/z</i> 253	-540722.2	-540725.0	-540722.1
<i>m/z</i> 225	-469539.9	-469540.4	-469538.5
<i>m/z</i> 109	-232051.4	-232048.7	-232044.6
N144		-308622.9	
N116		-237441.8	

The fluorobenzyl cation (*m/z* 109) can be released from the *m/z* 253 ion, which is the most predominant reaction for CID fragmentation, in either a one-step reaction (Path 1 in Fig. 2.13a) or a two-step reaction via elimination of carbon monoxide (CO) (Path 2 in Fig. 2.13a). Predicted free energy diagrams of Paths 1 and 2 are shown in Fig. 2.13b. The *m/z* 253 ion of the *ortho* isomer in Path 1 had the lowest free energy, while those of the *para* and *meta* isomers showed similar energies. Once the *m/z* 253 ions were cleaved by CID reaction, the order of free energies changed due to the halogen electron-donating resonance effect; *para* and *ortho* halogen substituents could stabilize the positive charge on the phenyl ring, while the *meta* halogen substituent has no such stabilization system. Based on the free energies of all the molecules, the relationship of the dissociation energy was *para* (47.9 kcal/mol) < *ortho* (53.5 kcal/mol) < *meta* (54.6 kcal/mol) (Path 1 in Fig. 2.13b). Analogous results were obtained in Path 2: 46.6 kcal/mol for *para*, 50.0 kcal/mol for *ortho*, and 52.1 kcal/mol for *meta* (Path 2 in Fig. 2.13b). Assuming that the CID reactions induced little conformational changes and had no large reverse activation energies, the dissociation reactivity between the fluorobenzyl group and the indazole moiety was concluded to be *meta* < *ortho* < *para*, which confirmed the relationship of the three isomers obtained by ERMS.

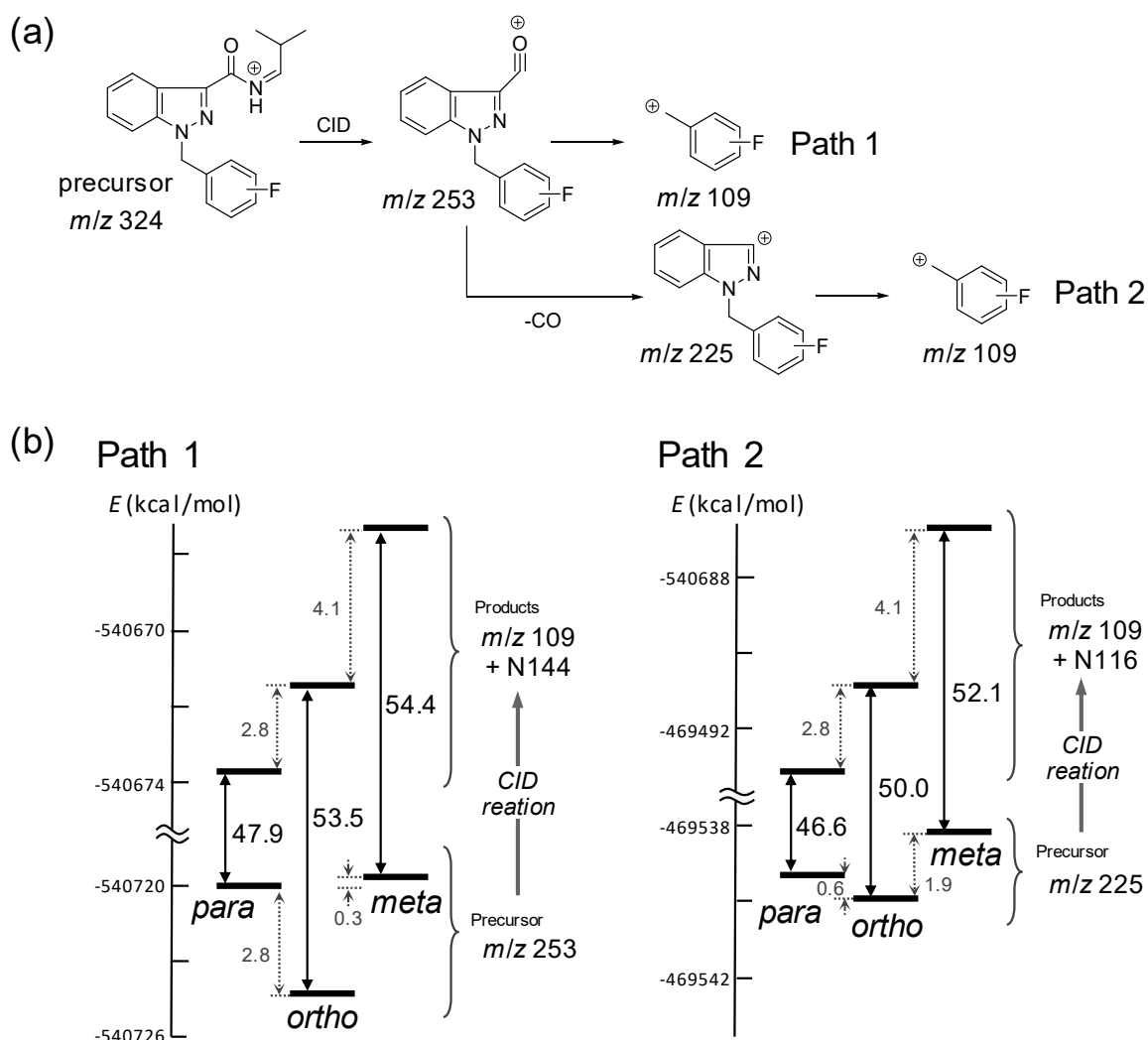


Fig. 2.13 (a) Proposed CID fragmentations and (b) predicted free energy diagrams of the CID cleavage reactions of the m/z 253 and 225 ions (Paths 1 and 2, respectively).

2.4 Summary

AB-FUBINACA (*para*) and its fluorine positional (*ortho* and *meta*) isomers on the phenyl ring were successfully differentiated by comparing the $\ln(A_{109}/A_{253})$ values obtained by ERMS using EI-QqQ-MS. The values showed in the order $meta < ortho < para$ at each CE. The reliability of the ERMS analysis was confirmed by the reproducibility of product ion spectra. Moreover, the relationships between the $\ln(A_{109}/A_{253})$ values and CEs were linear with high correlation coefficients. The differences in product ion abundances were attributed to

difference in the dissociation reactivity due to the halogen-substituted position on the phenyl ring. This methodology should also be applied to the positional isomer differentiation of other synthetic cannabinoids containing a fluorobenzyl group at the N-1 position, which is discussed in Chapter 3.

Chapter 3

Elucidation of the fluorine substitution position on the phenyl ring of synthetic cannabinoids by triple quadrupole mass spectrometry

3.1 Introduction

Synthetic cannabinoids containing a fluorobenzyl group at the N-1 position, including ADB-FUBINACA (narcotic) [77, 78], FUB-AMB (narcotic) [79], FUB-APINACA (designated substance) [80], FUB-NPB-22 (designated substance), and FU-PX-2 (designated substance) (Fig. 3.1), are difficult to distinguish between their fluorine positional isomers in both full scan and product ion spectra because few characteristic fragment ions can be observed. In addition, their positional isomer reference standards necessary for isomer differentiation analysis are not commercially available. In Chapter 2, AB-FUBINACA and its fluorine positional isomers were successfully differentiated using ERMS based on the differences in the abundance ratios of the product ions resulting from the difference in

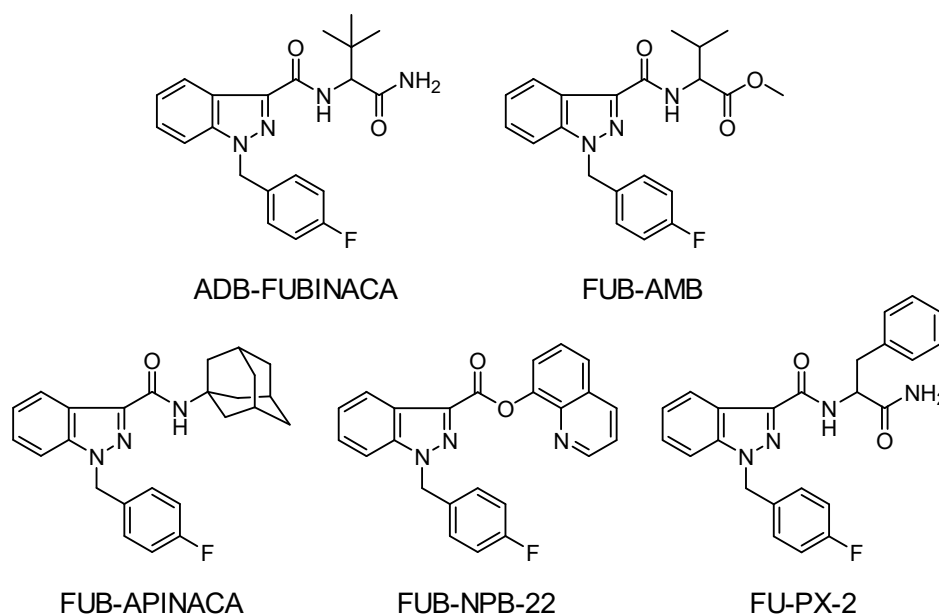


Fig. 3.1 Synthetic cannabinoids containing a fluorobenzyl group at the N-1 position.

dissociation reactivity of the fluorobenzyl group and indazole moiety [81]. This approach was expected to be applicable to positional differentiation for all indazole-type synthetic cannabinoids containing a fluorobenzyl group at the N-1 position. Herein, *o*-, *m*-, and *p*-fluorine positional isomeric model compounds of such synthetic cannabinoids were synthesized and their product ion spectra were examined using a similar ERMS technique described in Chapter 2. The logarithmic values of the mass spectral abundance ratios of the model compounds with those of several synthetic cannabinoids were compared.

3.2 Materials and Methods

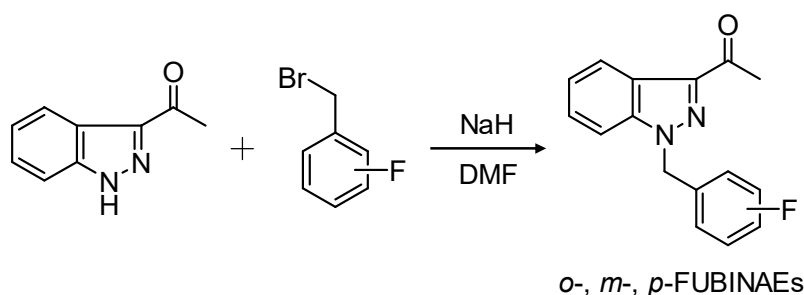
3.2.1 Reagents

AB-FUBINACA, its fluorine positional (*ortho* and *meta*) isomers, *N*-(1-amino-3,3-dimethyl-1-oxobutan-2-yl)-1-(4-fluorobenzyl)-1*H*-indazole-3-carboxamide (ADB-FUBINACA), methyl 2-[1-(4-fluorobenzyl)-1*H*-indazole-3-carboxamido]-3-methylbutanoate (FUB-AMB), *N*-(1-adamantyl)-1-(4-fluorobenzyl)-1*H*-indazole-3-carboxamide (FUB-APINACA), quinolin-8-yl 1-(4-fluorobenzyl)-1*H*-indazole-3-carboxylate (FUB-NPB-22), and *N*-(1-amino-1-oxo-3-phenylpropan-2-yl)-1-(4-fluorobenzyl)-1*H*-indazole-3-carboxamide (FU-PX-2) were purchased from Cayman Chemical (Ann Arbor, MI, USA). An herbal mixture laced with AB-FUBINACA, packed in a plastic bag, was seized from a suspect. 1-(1*H*-indazole-3-yl)ethanone was purchased from Sigma-Aldrich Co. (St. Louis, MO, USA). 2-, 3-, and 4-Fluorobenzyl bromide were purchased from Tokyo Chemical Industry Co., Ltd. (Tokyo, Japan).

The standard solutions of the synthetic cannabinoids (200 µg/mL) were prepared in methanol and were stored at -20°C. The working standard solutions (20 µg/mL) that were injected into the mass spectrometer were prepared by diluting the stock solutions. The herbal material (~10 mg) was extracted with 1 mL of methanol under ultrasonication for 10 min.

After the extract was centrifuged at $12,000 \times g$ for 1 min, the supernatant was filtered by an Ultrafree[®]-MC GV centrifugal filter unit with Durapore[®] PVDF 0.22- μm membrane (Millipore, Bedford, MA, USA). The solution was diluted with methanol to a suitable concentration for instrumental analysis.

3.2.2 Synthesis of model compounds of synthetic cannabinoids



Scheme 3.1 Synthesis of *o*-, *m*-, and *p*-FUBINAEs.

The three model compounds, 1-[1-(2-, 3-, and 4-fluorobenzyl)-1*H*-indazol-3-yl]ethanones (*o*-, *m*-, and *p*-FUBINAEs), were synthesized as shown in Scheme 3.1. To a solution of 1-(1*H*-indazol-3-yl)ethanone (29.7 mg) in dry *N,N*-dimethylformamide (1.8 mL) under argon atmosphere was added 60% sodium hydride (11.4 mg) at room temperature. After stirring for 30 min, 4-fluorobenzyl bromide (34.5 μL) was added. The mixture was stirred for 1 h and quenched by ammonium chloride aqueous solution. The mixture was extracted with ethyl acetate/hexane (1:1, *v/v*) three times. The combined organic extracts were dried over anhydrous sodium sulfate, filtered through Celite[®], and evaporated. The residue was purified by preparative TLC using Wakogel[®] B-5F (Wako Pure Chemical Industries, Ltd., Osaka, Japan) with ethyl acetate/hexane (1:2, *v/v*) as the eluent to afford 1-[1-(4-fluorobenzyl)-1*H*-indazol-3-yl]ethanone (*p*-FUBINAE) as a colorless solid (44.2 mg, yield: 89%). 1-[1-(2-Fluorobenzyl)-1*H*-indazol-3-yl]ethanone (*o*-FUBINAE, 20.7 mg, yield: 59%) and 1-[1-(3-fluorobenzyl)-1*H*-indazol-3-yl]ethanone (*m*-FUBINAE, 21.9 mg, yield: 66%) were

also prepared by the same procedure from 1-(1*H*-indazol-3-yl)ethanone (20 mg), respectively. The chemical structures were confirmed by ¹H-NMR spectroscopy. ¹H-NMR spectra (400 MHz, CDCl₃) were recorded on a JNM-ECS 400 (JEOL Ltd., Tokyo, Japan) at 23°C with residual solvent peak at 7.24 ppm as an internal standard. The ¹H-NMR data for each synthesized compound are summarized below.

o-FUBINAE; ¹H NMR (CDCl₃) δ: 8.35 (1H, d, *J* = 7.9 Hz), 7.47–7.35 (2H, m), 7.33–7.24 (2H, m), 7.11–7.00 (3H, m), 5.69 (2H, s), 2.72 (3H, s).

m-FUBINAE; ¹H NMR (CDCl₃) δ: 8.37 (1H, d, *J* = 7.9 Hz), 7.41–7.25 (4H, m), 7.02–6.93 (2H, m), 6.88 (1H, d, *J* = 9.5 Hz) 5.63 (2H, s), 2.77 (3H, s).

p-FUBINAE; ¹H NMR (CDCl₃) δ: 8.36 (1H, d, *J* = 8.0 Hz), 7.40–7.27 (3H, m), 7.23–7.17 (2H, m), 7.02–6.95 (2H, m), 5.60 (2H, s), 2.72 (3H, s).

3.2.3 Instrumentation

Mass spectra were obtained by a SCION TQ triple quadrupole mass spectrometer (Bruker Daltonics, Billerica, MA, USA) with a BR-5ms fused-silica capillary column (30 m × 0.25 mm i.d., 0.25-μm film thickness; Bruker Daltonics). The inlet temperature was set at 200°C. The injection mode was splitless. The sample injection volume was 1 μL. The carrier gas was high-purity helium (six nine-grade) at a constant column flow rate of 45.1 cm/s. The temperature program for full scan mode consisted of an initial temperature at 80°C held for 1 min, ramped up to 300°C at 10°C/min followed by a hold at 300°C for 15 min. The temperature program for product ion scan mode consisted of an initial temperature at 200°C held for 1 min, ramped up to 300°C at 10°C/min followed by a hold at 300°C for 10 min. The transfer line was maintained at 280°C. The mass spectrometer was operated in EI mode at 70 eV using an ion-source temperature of 230°C. The acquisition of full scan mode was in the

range of m/z 40–600. The acquisition of product ion scan mode was in the range of m/z 40–253 for the precursor ion at m/z 253. Argon gas pressure on CID reaction was set at 1.5 mTorr. The abundances of the selected ions were presented as the areas of the mass chromatographic peaks in order to avoid the effect of spectral skewing. Individual data were fitted using the Boltzmann sigmoidal function with nonlinear regression analysis (Subsection 2.2.4 of Chapter 2). To obtain an acceptable quality spectrum, the mass spectrometer was tuned according to the instrument protocol as needed. All the analyses described below should be completed in as short a period of time as possible using the same instrumental condition, since the given CE potentially changes slightly due to instrumental mechanical fluctuations.

3.2.4 Statistical calculations

Statistical analyses were performed using BellCurve for Excel ver. 2.02 (Social Survey Research Information Co., Ltd., Tokyo, Japan), which is add-in software to Microsoft Excel 2010. The homogeneity of variances was calculated by performing Bartlett's test to determine if obtained data were normally distributed (parametric, $p > 0.05$) or not (nonparametric, $p < 0.05$). If the data were parametric, one-way ANOVA was carried out, followed by multiple pairwise comparisons as post hoc analysis using the Tukey's test [69,82]. For the nonparametric data, nonparametric ANOVA (Kruskal-Wallis test) followed by multiple pairwise comparisons using Steel-Dwass test was carried out [83].

3.3 Results and Discussion

3.3.1 Gas chromatography

GC separation of the *o*-, *m*-, and *p*-FUBINAEs was achieved using a non-polar capillary column BR-5ms (30 m × 0.25 mm i.d., 0.25- μ m film thickness, stationary phase: 5% diphenyl/95% dimethyl arylene siloxane) under the temperature program for full scan mode (Fig. 3.2). The three isomers eluted in the order of *o*-, *m*-, *p*-FUBINAE. The retention indices were 2158 for *o*-FUBINAE, 2170 for *m*-FUBINAE, and 2183 for *p*-FUBINAE.

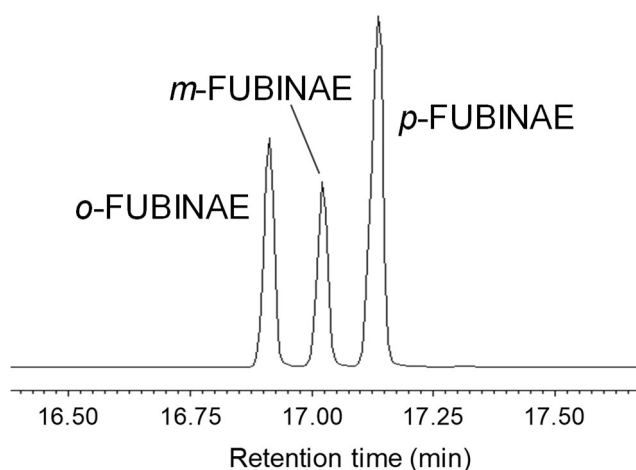


Fig. 3.2 Total ion current chromatogram for the mixture of *o*-, *m*-, and *p*-FUBINAEs.

3.3.2 Full scan mass spectrometry

Figure 3.3 shows the EI-full scan mass spectra of *o*-, *m*-, and *p*-FUBINAEs. The three isomers gave identical fragment ions. Major fragment ions were observed at m/z 43, 83, 109, 225, 253, and 268. The proposed EI fragmentation pathways are shown in Fig. 3.4. The m/z 268 ion is the molecular radical cation of the analyte resulting from initial ionization of the indazole nitrogen (Fig. 3.4a), the carbonyl oxygen (Fig. 3.4b), or the fluorobenzene carbon (Fig. 3.4c) in accordance with classical mass spectral interpretation [55,84]. The m/z 253 ion could originate from the nitrogen (Fig. 3.4d) or the carbonyl oxygen (Fig. 3.4e), resulting in

the loss of a methyl radical by homolytic cleavage between the carbonyl and methyl carbons [55]. The mechanisms by which the fragment ions at m/z 268 (Figs. 3.4a and 3.4b) and 253 (Figs. 3.4c and 3.4d) are formed are essentially the same because they are resonance structures. The m/z 225 ion is the carbenium cation generated by elimination of CO from the m/z 253 ion. The m/z 109 ion, which is the base peak, corresponds to the fluorobenzyl cation

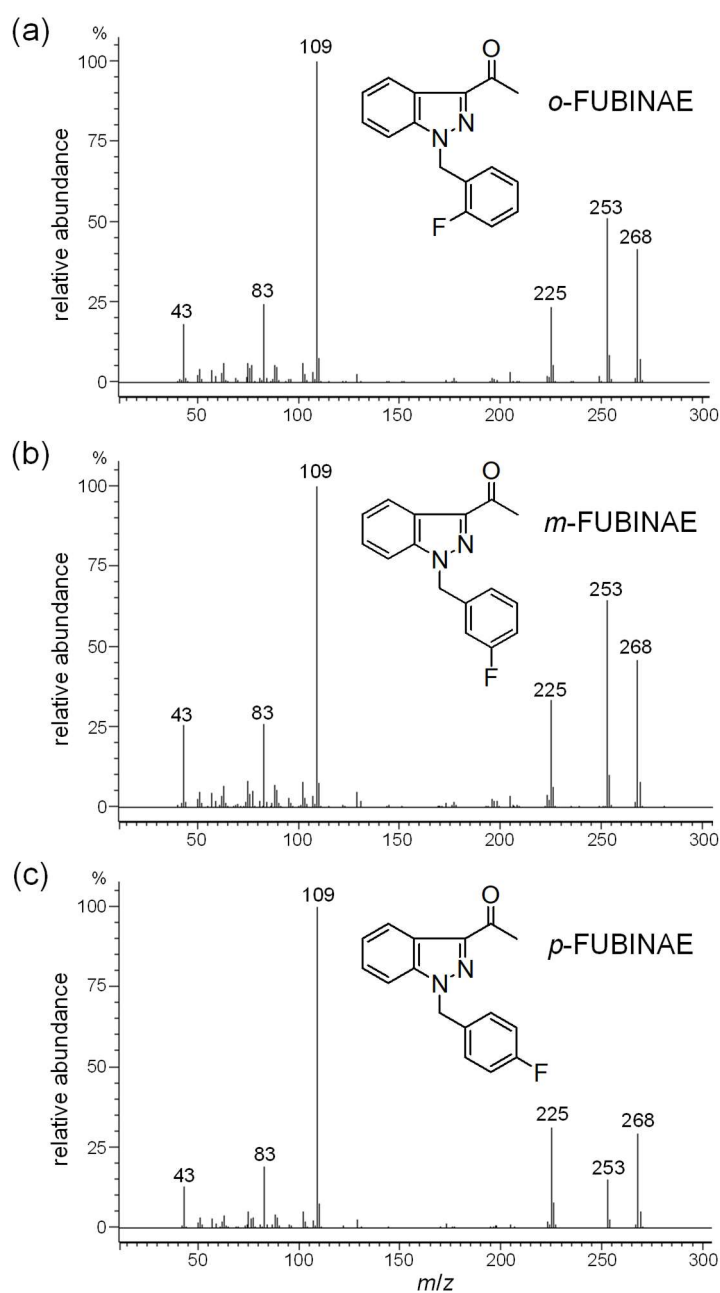


Fig. 3.3 EI-full scan mass spectra of o -, m -, and p -FUBINAEs.

(or fluorotropylium cation) resulting from cleavage of the methylene linkage between the fluorobenzyl group and the indazole moiety of the m/z 268 ion. The two remaining low mass ions at m/z 83 and 43 are the fluorocyclopentadienyl cation formed by the loss of an acetylene from the m/z 109 ion [84] and the acetyl cation formed by the loss of the 1-(2-, 3-, or 4-fluorobenzyl)-1*H*-indazole radical from the m/z 268 ion, respectively. *p*-FUBINAE was clearly differentiated from *o*- and *m*-FUBINAEs in respect to the different relative abundances of the ions at m/z 253 and 268 (Fig. 3.3). Although the relative abundance of the *o*-FUBINAE ion at m/z 253 was slightly lower than that of the *m*-FUBINAE, *o*- and *m*-FUBINAE spectra overall were highly similar to each other.

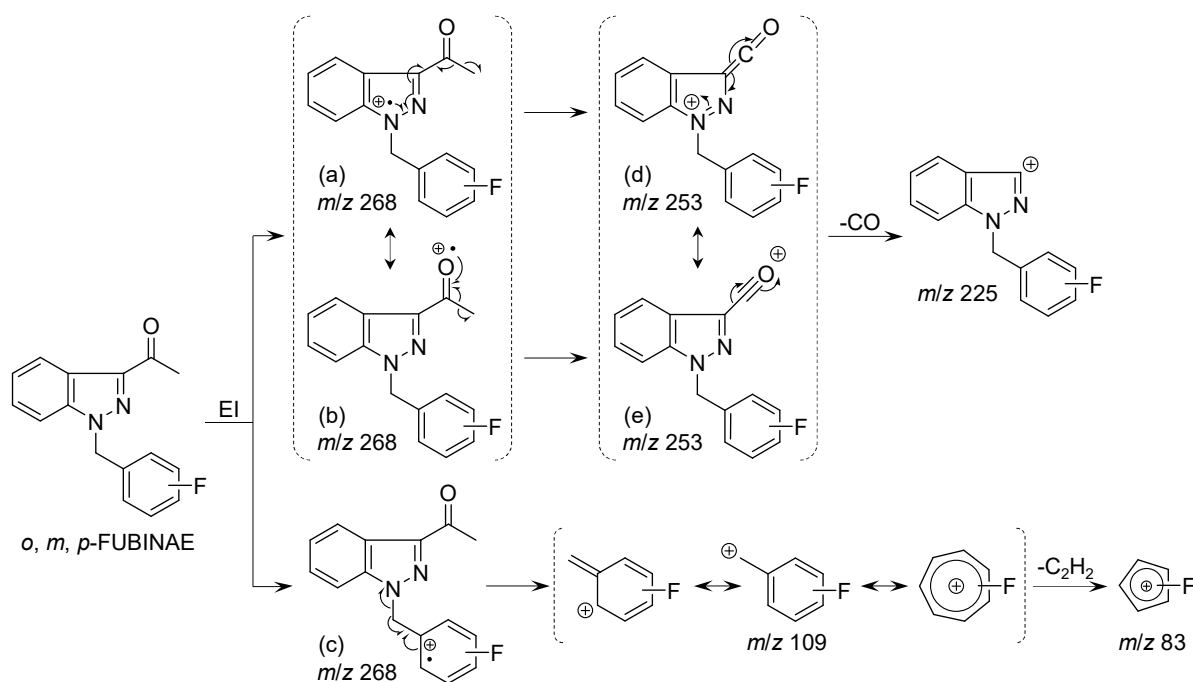


Fig. 3.4 Proposed EI fragmentation pathways of *o*-, *m*-, and *p*-FUBINAEs.

3.3.4 Energy-resolved mass spectrometry

The fragment ion peak at m/z 253 is common to all of the indazole-type synthetic cannabinoids containing a fluorobenzyl group at the N-1 position. The product ion spectra of *o*-, *m*-, and *p*-FUBINAEs were measured by the same ERMS methodology performed in Subsection 2.3.2 of Chapter 2. The precursor ion and the CE were set at m/z 253 and at 5–40 eV in increments of 5 eV, respectively. The observed product ions were identical among the three isomers at all the CEs (Fig. 3.5). However, the three isomers differed in the relative abundances of the product ion at m/z 109 and the precursor ion at m/z 253 at the CEs ranging from 5 to 15 eV. The relative abundances of the *p*-FUBINAE ion at m/z 109 at the CEs of 5 and 10 eV were higher than those of the *o*- and *m*-FUBINAEs, while the relative abundance of the *o*-FUBINAE ion at m/z 109 at 10 eV was slightly higher than that of *m*-FUBINAE. The relative abundance of the *m*-FUBINAE ion at m/z 253 at 15 eV was higher than that of the *o*- and *p*-FUBINAEs, while that of the *o*-FUBINAE ion at m/z 253 was slightly higher than for *p*-FUBINAE. In the product ion spectra in the range of 20–40 eV, significant differences among the three isomers were not found.

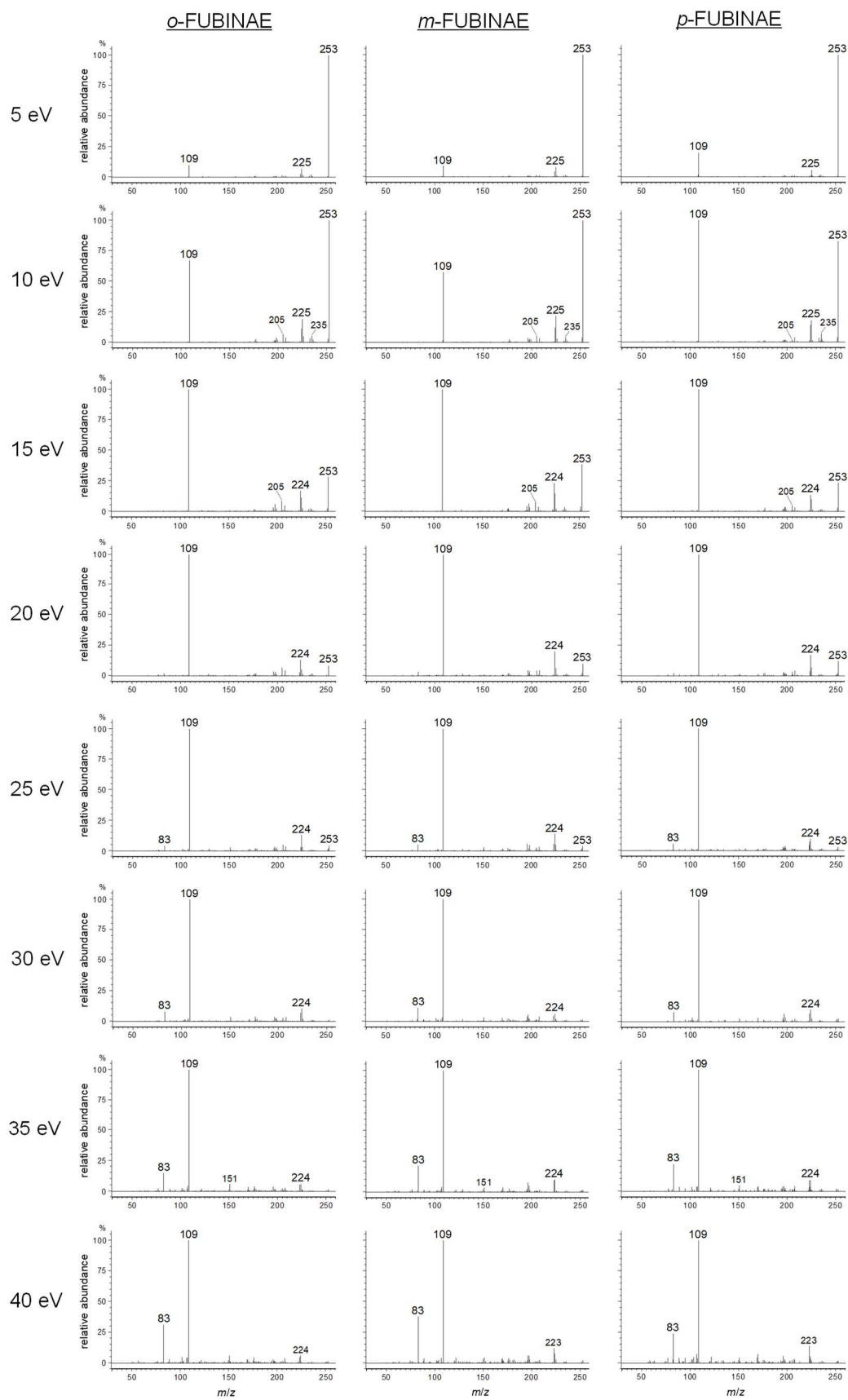


Fig. 3.5 Product ion spectra of *o*-, *m*-, and *p*-FUBINAEs for the precursor ion at *m/z* 253 at the CEs of 5–40 eV in increments of 5 eV.

3.3.5 Breakdown curves of *o*-, *m*-, and *p*-FUBINAEs

To further clarify the behaviors of the two ions at m/z 109 and 253, ERMS was also performed with CE setting varying from 4 to 16 eV (4–10 eV in increments of 1 eV and 10–16 eV in increments of 2 eV). The obtained three breakdown curves were shown in Fig. 3.6. The fragment ion at m/z 109 was mainly produced by a CID reaction. Only small amounts of the product ions at m/z 205, 224, 225, and 235 were observed, and there were little differences in the total yields of their ions at any given CE. This data suggested that the decomposition of the precursor m/z 253 ion almost always produced the m/z 109 ion. Although the patterns of the breakdown curves were similar, the sigmoidal-shaped growth (m/z 109) and decay (m/z 253) curves intersected at different CE values for each of the three isomers (*para* < *ortho* < *meta*). The two ions at m/z 109 and 253 showed very small variabilities attributed to good reproducibility of mass spectral analysis. The standard deviations determined by the intraday variabilities of the abundances (%TIC) of m/z 109 and 253 were < 1.8 and < 1.7, respectively ($n = 5$, Table 3.1). The logarithmic values of the abundance ratio of the ion at m/z 109 to 253 [$\ln(A_{109}/A_{253})$] in the CE range of 4–10 eV showed the relationship of *meta* < *ortho* < *para* (Fig. 3.7), and those values for each isomer increased linearly relative to CE with high correlation coefficients. To assure the significances between the $\ln(A_{109}/A_{253})$ values of the three isomers, ANOVA followed by multiple pairwise comparisons was carried out. Bartlett's test for homogeneity of variances showed that the $\ln(A_{109}/A_{253})$ values at the CEs of 4, 5, 6, 8, 9 and 10 eV were normally distributed (parametric) and those at 7 eV were nonparametric. For the parametric data, one-way ANOVA followed by the Tukey's test was carried out. The $\ln(A_{109}/A_{253})$ values of the three isomers were significantly different at each CE ($\alpha < 3.4 \times 10^{-11}$), and Tukey's test showed low p values at each CE ($p < 1.4 \times 10^{-5}$) (Table 3.2). For the nonparametric data (CE, 7 eV), the Kruskal-Wallis and the Steel-Dwass tests showed that three isomers were significantly different ($\alpha = 2.5 \times 10^{-3}$, $p < 2.5 \times 10^{-2}$, Table 3.2).

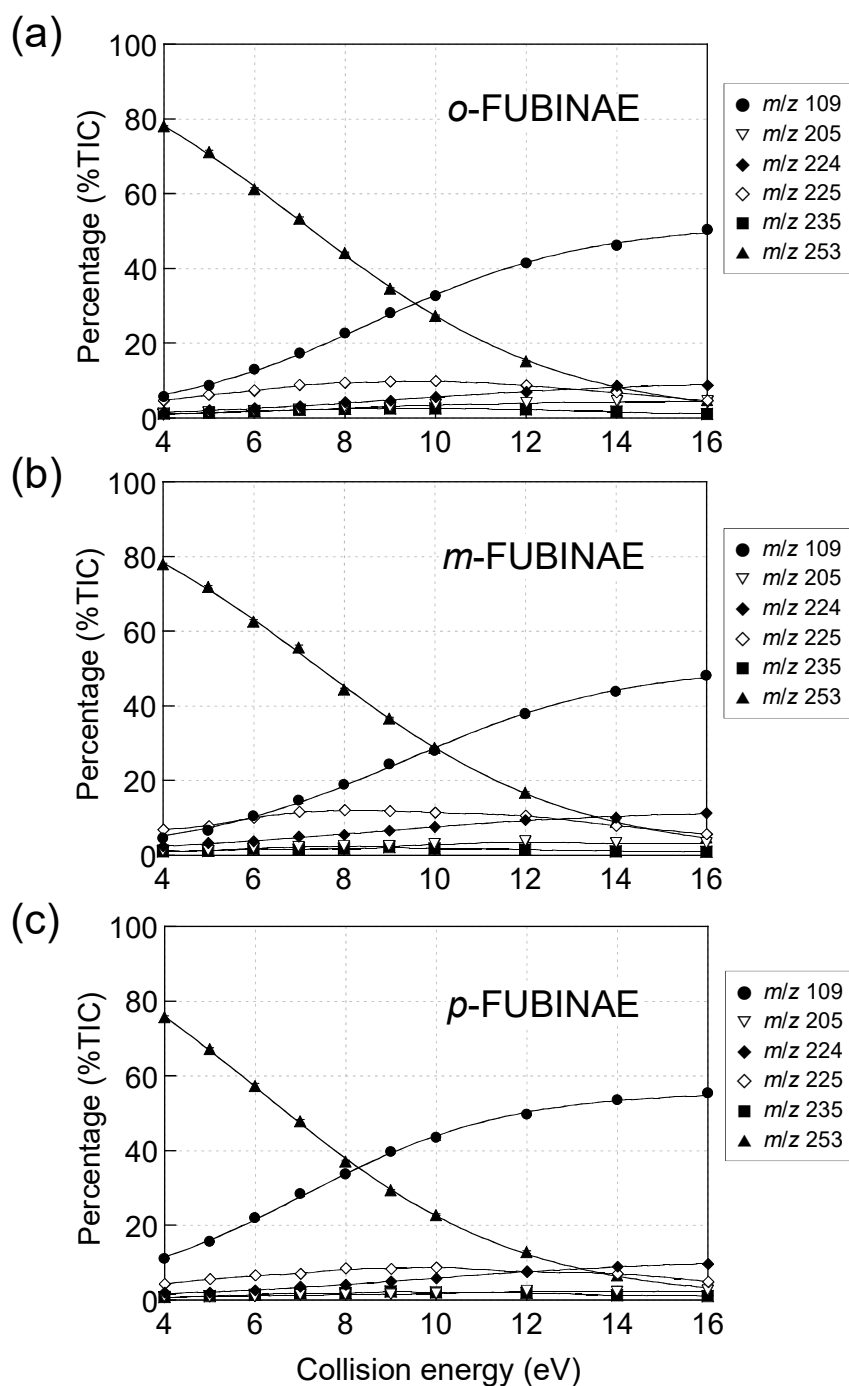


Fig. 3.6 Breakdown curves of (a) *o*-FUBINAE, (b) *m*-FUBINAE, and (c) *p*-FUBINAE in the CE range of 4–16 eV. The precursor ion was set at *m/z* 253. Error bars of the ions at *m/z* 109 and 253 represent standard errors ($n = 5$).

Table 3.1 Standard deviations determined by the intraday variability of the abundances (%TIC) of the m/z 109 and 253 ions of the *o*-, *m*-, *p*-FUBINAEs ($n = 5$).

CE (eV)	<i>o</i> -FUBINAE		<i>m</i> -FUBINAE		<i>p</i> -FUBINAE	
	m/z 109	m/z 253	m/z 109	m/z 253	m/z 109	m/z 253
4	0.2	0.4	0.2	0.6	0.3	0.9
5	0.2	0.9	0.1	0.8	0.4	0.8
6	0.5	0.9	0.3	1.2	1.0	1.7
7	0.2	1.2	1.8	1.5	1.5	0.9
8	0.3	0.4	0.3	0.8	0.8	0.5
9	0.7	0.4	0.4	0.6	0.9	0.4
10	0.4	0.7	0.1	0.6	1.3	0.6
12	0.8	0.7	1.1	0.5	0.6	0.9
14	0.9	0.3	1.2	0.4	1.1	0.3
16	0.5	0.1	1.7	0.3	1.4	0.9

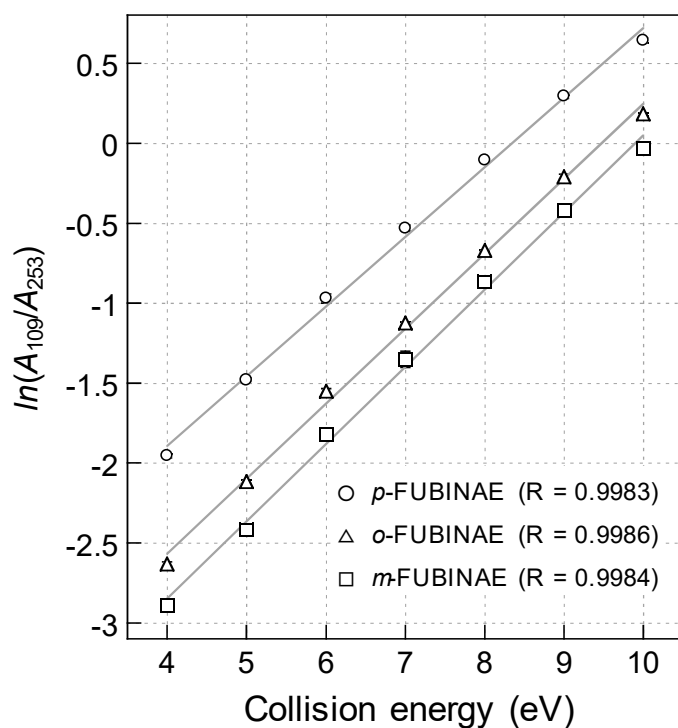


Fig. 3.7 Logarithmic plots of the abundance ratio of the m/z 109 ion to the 253 ion for o -, m -, and p -FUBINAEs. The precursor ion was set at m/z 253. Error bars represent standard errors ($n = 5$).

Table 3.2 Analysis of variance (ANOVA) and multiple pairwise comparisons for logarithmic values of the abundance ratio of the product ion at m/z 109 to the precursor ion at m/z 253 [$\ln(A_{109}/A_{253})$] of o -, m -, and p -FUBINAEs.

CE (eV)	ANOVA ^a (α)	Multiple pairwise comparisons ^b (p)		
		<i>ortho</i> \times <i>meta</i>	<i>ortho</i> \times <i>para</i>	<i>meta</i> \times <i>para</i>
4	2.7×10^{-14}	1.8×10^{-6}	1.7×10^{-6}	1.7×10^{-6}
5	5.1×10^{-16}	1.7×10^{-6}	1.7×10^{-6}	1.7×10^{-6}
6	3.4×10^{-11}	1.4×10^{-5}	1.7×10^{-6}	1.7×10^{-6}
7	2.5×10^{-3}	4.3×10^{-2}	2.5×10^{-2}	2.5×10^{-2}
8	8.4×10^{-16}	1.7×10^{-6}	1.7×10^{-6}	1.7×10^{-6}
9	2.2×10^{-13}	2.0×10^{-6}	1.7×10^{-6}	1.7×10^{-6}
10	9.2×10^{-13}	2.1×10^{-6}	1.7×10^{-6}	1.7×10^{-6}

^a one-way ANOVA (4, 5, 6, 8, 9, and 10 eV), Kruskal-Wallis test (7 eV)

^b Tukey's test (4, 5, 6, 8, 9, and 10 eV), Steel-Dwass test (7 eV)

3.3.6 Comparisons of *o*-, *m*-, and *p*-FUBINAEs with synthetic cannabinoids

The above-mentioned results of the FUBINAE isomers were same as for the AB-FUBINACA isomers described in Subsection 2.3.3 of Chapter 2. The ERMS analyses for both the FUBINAE isomers and the AB-FUBINACA isomers were carried out under the same instrumental conditions. Comparing the $\ln(A_{109}/A_{253})$ plots of the FUBINAE isomers with those of the AB-FUBINACA isomers revealed that the FUBINAE isomers behaved just like their corresponding positional AB-FUBINACA isomers (Fig. 3.8). This suggested that the relative abundances of the two ions at m/z 109 and 253 were nearly independent of the analyte structures, because the given energies in CID reaction were sufficiently higher than the internal energies of the precursor m/z 253 ion [85]. The $\ln(A_{109}/A_{253})$ plots of ADB-FUBINACA, FUB-AMB, FUB-APINACA, FUB-NPB-22, and FU-PX-2, all of which contain a *p*-fluorobenzyl group, also corresponded to that of *p*-FUBINAE (Fig. 3.9a–e). Likewise, the plot of the methanol extract from the herbal product laced with AB-FUBINACA also corresponded with the plot of *p*-FUBINAE (Fig. 3.9f). All these results indicated that the fluorine substitution position on the phenyl ring of indazole-type synthetic cannabinoids containing a fluorobenzyl group at the N-1 position can be elucidated by collating the $\ln(A_{109}/A_{253})$ plot sets of *o*-, *m*-, and *p*-FUBINAEs.

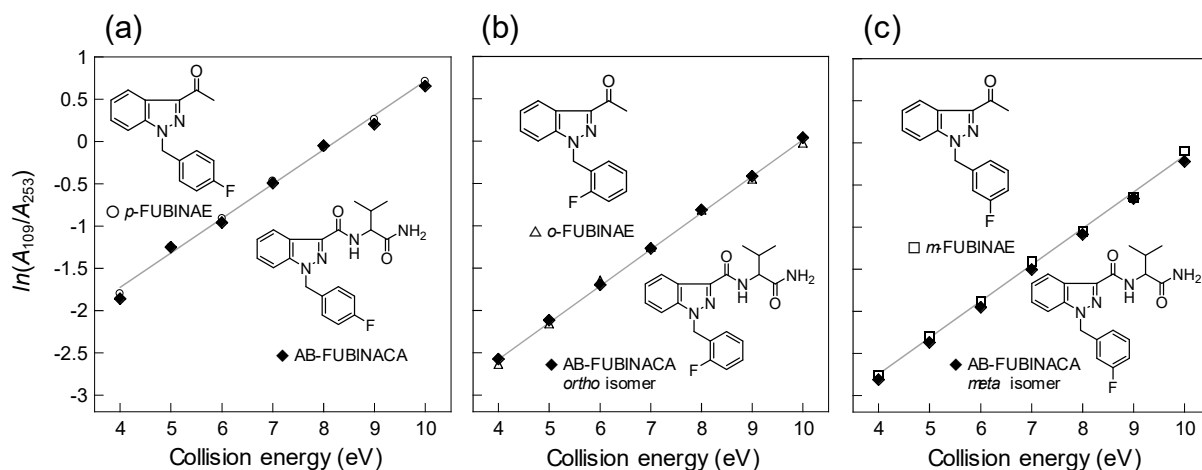


Fig. 3.8 Comparisons of the $\ln(A_{109}/A_{253})$ plots of (a) AB-FUBINACA with *p*-FUBINAE, (b) AB-FUBINACA *ortho* isomer with *o*-FUBINAE, and (c) AB-FUBINACA *meta* isomer with *m*-FUBINAE.

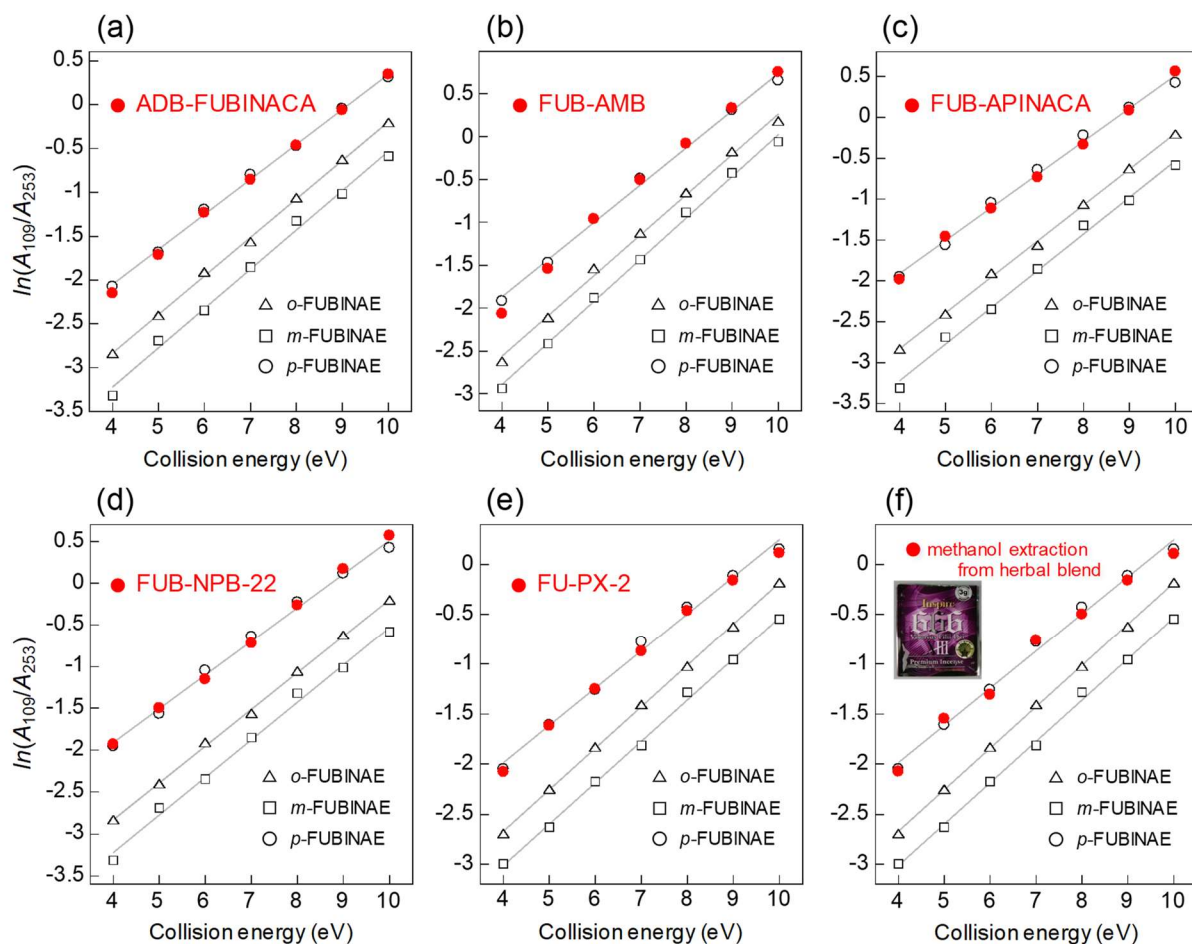


Fig. 3.9 Comparisons of the $\ln(A_{109}/A_{253})$ plots of (a) ADB-FUBINACA, (b) FUB-AMB, (c) FUB-APINACA, (d) FUB-NPB-22, (e) FU-PX-2, and (f) methanol extract from herbal blend containing AB-FUBINACA, with a set of *o*-, *m*- and *p*-FUBINAEs.

3.4 Summary

Three model indazole-type synthetic cannabinoids containing a fluorobenzyl group at the N-1 position, namely *o*-, *m*-, and *p*-FUBINAEs, were synthesized. Although their full scan and product ion spectra were very similar to each other, they were differentiated by plotting the $\ln(A_{109}/A_{253})$ values against CE. Each $\ln(A_{109}/A_{253})$ plot of *o*-, *m*-, and *p*-FUBINAEs corresponded with those of the three AB-FUBINACA positional isomers that contained the same fluorine substitution position on the phenyl ring, obtained by ERMS under the same instrumental conditions. In addition, the plots of other indazole-type synthetic cannabinoids with a *p*-fluorobenzyl group at the N-1 position (ADB-FUBINACA, FUB-AMB, FUB-APINACA, FUB-NPB-22, and FU-PX-2) and the methanolic extract of the herbal product containing AB-FUBINACA corresponded with that of *p*-FUBINAE. Therefore, it could be concluded that the fluorine substitution position of indazole-type synthetic cannabinoids containing a fluorobenzyl group could be determined by collating the *o*-, *m*-, and *p*-FUBINAE data sets. This methodology is promising for selecting reference standard candidates for positional isomers of an analyte.

Chapter 4

Differentiation of AB-FUBINACA and its five positional isomers using liquid chromatography–electrospray ionization–linear ion trap mass spectrometry and triple quadrupole mass spectrometry

4.1 Introduction

Chapters 2 and 3 described the ERMS positional isomer differentiation strategy featuring GC/EI-QqQ-MS and its application in distinguishing between *o*-, *m*-, and *p*-fluorine positional isomers of synthetic cannabinoids containing a fluorobenzyl group, including AB-FUBINACA and its *ortho* and *meta* isomers [81,86]. It is likely that the ERMS methodology could be used in combination with other chromatographic and ionization techniques for forensic analysis. Therefore, other analytical techniques, LC/ESI-LIT-MS and LC/ESI-QqQ-MS, were tested for their capability to distinguish AB-FUBINACA positional isomers, including fluorine positional isomers on the phenyl ring and methyl positional isomers in the carboxamide side chain (Fig. 4.1).

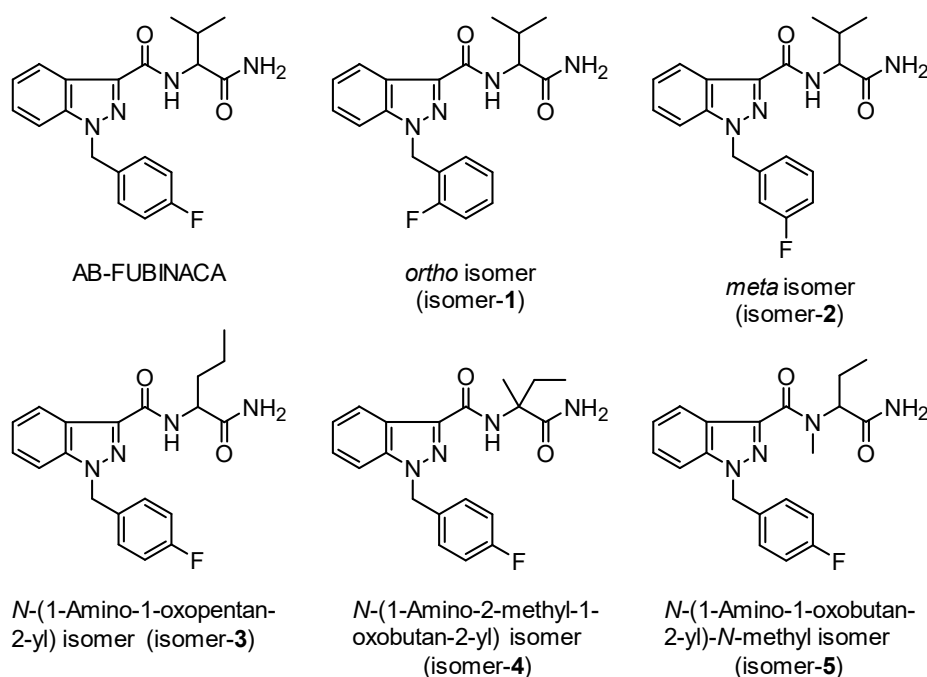


Fig. 4.1 Structures of AB-FUBINACA and its five positional isomers.

4.2 Materials and methods

4.2.1 Reagents

AB-FUBINACA, its *o*- and *m*-fluorine positional isomers (*ortho*: isomer-1, *meta*: isomer-2), *N*-(1-amino-1-oxopentan-2-yl)-1-(4-fluorobenzyl)-1*H*-indazole-3-carboxamide (isomer-3), *N*-(1-amino-2-methyl-1-oxobutan-2-yl)-1-(4-fluorobenzyl)-1*H*-indazole-3-carboxamide (isomer-4), and *N*-(1-amino-1-oxobutan-2-yl)-1-(4-fluorobenzyl)-*N*-methyl-1*H*-indazole-3-carboxamide (isomer-5) (Fig. 4.1) were purchased from Cayman Chemical (Ann Arbor, MI, USA). Their standard stock solutions (200 µg/mL) were prepared in methanol and stored at -20°C. The working standard solutions (20 µg/mL) to be injected into the mass spectrometer were prepared by diluting the stock solutions.

4.2.2 Instrumentation

LC/ESI-LIT-MS was performed on a Prominence Ultrafast Liquid Chromatograph (Shimadzu, Kyoto, Japan) linked to an LXQ LIT mass spectrometer (Thermo Fisher Scientific, Waltham, MA, USA) equipped with an ESI source. Instrumental control, data acquisition, and analysis were performed using Xcalibur software ver. 2.0 (Thermo Fisher Scientific). The analytes were separated using two ODS columns: (I) L-column 2 ODS column (150 × 1.5 mm i.d., 5-µm particle size; Chemicals Evaluation and Research Institute, Tokyo, Japan) and (II) YMC-Ultra HT Pro C18 column (75 × 2.0 mm i.d., 2-µm particle size; YMC. Co., Ltd., Kyoto, Japan) at a column oven temperature of 40°C. The injection volume was 1 µL. Other LC parameters using (I) the L-column 2 ODS column and (II) YMC-Ultra HT Pro C18 column were as follows, respectively: (I) flow rate, 0.1 mL/min; elution mode, gradient with 10 mM ammonium acetate/5% methanol in distilled water (A) and 10 mM ammonium acetate/5% distilled water in methanol (B) from 100% A to 100% B over 15 min, and by isocratic elution with the final solvent composition for 10 min; and (II) flow rate, 0.25

mL/min; elution mode, isocratic with 50% A/50% B for 30 min. The MS parameters were as follows: polarity, positive and negative; scan mode, product ion scan; activation type, CID; isolation width, m/z 2.00; normalized CE, 35.0%; activation Q, 0.250; activation time, 30 ms; and collision gas, helium.

LC/ESI-QqQ-MS was performed on an Agilent 1260 Infinity LC system linked to a 6470A triple quadrupole LC/MS tandem mass spectrometer (Agilent Technologies, Santa Clara, CA, USA) equipped with an ESI source. Instrumental control, data acquisition, and analysis were performed using Mass Hunter software ver. B.07.00 (Agilent Technologies). An L-column 2 ODS column (150 × 1.5 mm i.d., 5- μ m particle size; Chemicals Evaluation and Research Institute) was used at a column oven temperature of 40°C. The injection volume was 5 μ L. The flow rate was 0.1 mL/min. The elution mode was isocratic with 10 mM ammonium acetate/60% methanol in distilled water for 25 min. The MS parameters were as follows: polarity, positive; scan mode, product ion scan; fragmentor voltage, 80 eV; cell accelerator voltage, 5 eV; and collision gas, nitrogen.

4.2.3 Statistical calculations

Statistical analyses were performed using BellCurve for Excel ver. 2.02 (Social Survey Research Information Co., Ltd., Tokyo, Japan), which is an add-in software to Microsoft Excel 2010. The homogeneity of variances was calculated by Bartlett's test to determine if the obtained data were normally distributed (parametric, $p > 0.05$) or not (nonparametric, $p < 0.05$). If the data were parametric, one-way ANOVA followed by multiple pairwise comparisons using the Tukey's test was performed [69,82]. For nonparametric data, Kruskal-Wallis test as nonparametric ANOVA, followed by the Steel-Dwass test as a nonparametric multiple pairwise comparison, was performed [83].

4.3 Results and discussion

4.3.1 Liquid chromatography

The LC method (I) described in subsection 4.2.2 is typically used for drug screening analysis. The extracted ion chromatogram ($[M+H]^+$, m/z 369) of a mixture of the six AB-FUBINACA isomers is shown in Fig. 4.2a. The six isomers coeluted and could not be baseline separated. Although isomer-4 and isomer-5 overlapped at the peak shoulders, they were distinguished at the peak apexes. The existence of isomer-1 was recognized, but the peak was buried in the group of peaks for AB-FUBINACA, isomer-2, and isomer-3. Among other ODS columns and mobile-phase compositions, a YMC-Ultra HT Pro C18 column operated in isocratic mode achieved chromatographic separation among isomers-1, -3, -4, and -5, while AB-FUBINACA and isomer-2 still coeluted (Fig. 4.2b). Their elution order was

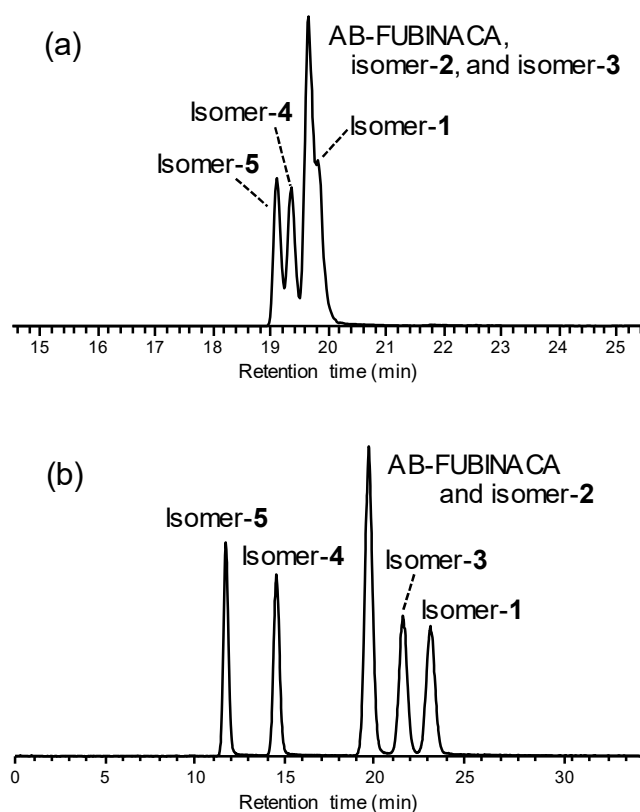


Fig. 4.2 Extracted ion chromatogram ($[M+H]^+$; m/z 369) of a mixture of AB-FUBINACA and its five positional isomers using (a) an L-column 2 ODS column in gradient mode and (b) a YMC Ultra HT Pro C18 column in isocratic mode.

isomer-5 < isomer-4 < 'AB-FUBINACA and isomer-2' < isomer-3 < isomer-1. The coelution of AB-FUBINACA and isomer-2 resulted from the minimal interaction strength difference with the ODS column surface, because of their high conformational similarity.

4.3.2 Linear ion trap multiple-stage mass spectrometry

LIT-MS can be used for multiple-stage MS (MS^n) simply by using additional operations performed sequentially and varies the ion/molecule reaction time to delineate the kinetics, equilibrium, and fragmentation mechanisms [87]. ESI-LIT mass spectra of the six isomers were recorded in positive mode. The precursor ions at the MS^2 – MS^6 stages were set at m/z 369, 352, 324, 253, and 225, respectively. The obtained mass spectra in the MS^1 – MS^6 stages are shown in Fig. 4.3. Spectra in stages greater than MS^7 were not obtained because of the lack of product ions. In the mass spectra of each isomer, identical ions were observed at m/z 369 ($[M+H]^+$) and 391 ($[M+Na]^+$) in the MS^1 stage, at m/z 352 ($[M-NH_2]^+$) in MS^2 , at m/z 324 ($[M-CONH_2]^+$) in MS^3 , at m/z 253 ($[M-(C_4H_9N)CONH_2]^+$) in MS^4 , at m/z 109 (fluorobenzyl cation or fluorotropylium cation), 225 ($[M-CO(C_4H_9N)CONH_2]^+$) and 235 in MS^5 , and at m/z 198 and 205 in MS^6 . Although the abundances of the ions at m/z 198 in MS^6 appeared to slightly differ in isomer-2, the other mass spectra were very similar. Therefore, ESI-LIT-MS operated in positive mode could not be used to effectively differentiate the six isomers.

Mass spectra of the six isomers were also obtained in negative mode in the MS^1 – MS^3 stages (Fig. 4.4). Note that spectra at stages greater than MS^4 were not consistently available, because of the lack of product ions. The precursor ions at MS^2 and MS^3 stages were set at m/z 427 and 367, respectively. The acetate adduct ions at m/z 427 ($[M+CH_3COO]^-$) at MS^1 and the deprotonated ions at m/z 367 ($[M-H]^-$) at MS^2 were observed as base peaks for all the isomers. At the MS^3 stage, some spectral differences among isomers-1, -4, and -5 were

observed. The m/z 271 ion of isomer-1 was detected as the base peak, whereas the m/z 349 ion was hardly detected. Furthermore, the abundances of the m/z 141 and 225 ions were lower than those of the other isomers. Isomer-4 showed a characteristic ion at m/z 243. Isomer-5 showed characteristic ions at m/z 251 and 324, whereas the m/z 271 ion was barely detected. In addition, the relative abundance of the m/z 349 ion was higher than that of AB-FUBINACA, isomer-2, -3, or -4, which constituted the base peak. It was difficult to differentiate among AB-FUBINACA, isomer-2, and isomer-3 because of their similar spectral patterns, although the relative abundance of the m/z 141 ion of isomer-2 was slightly lower.

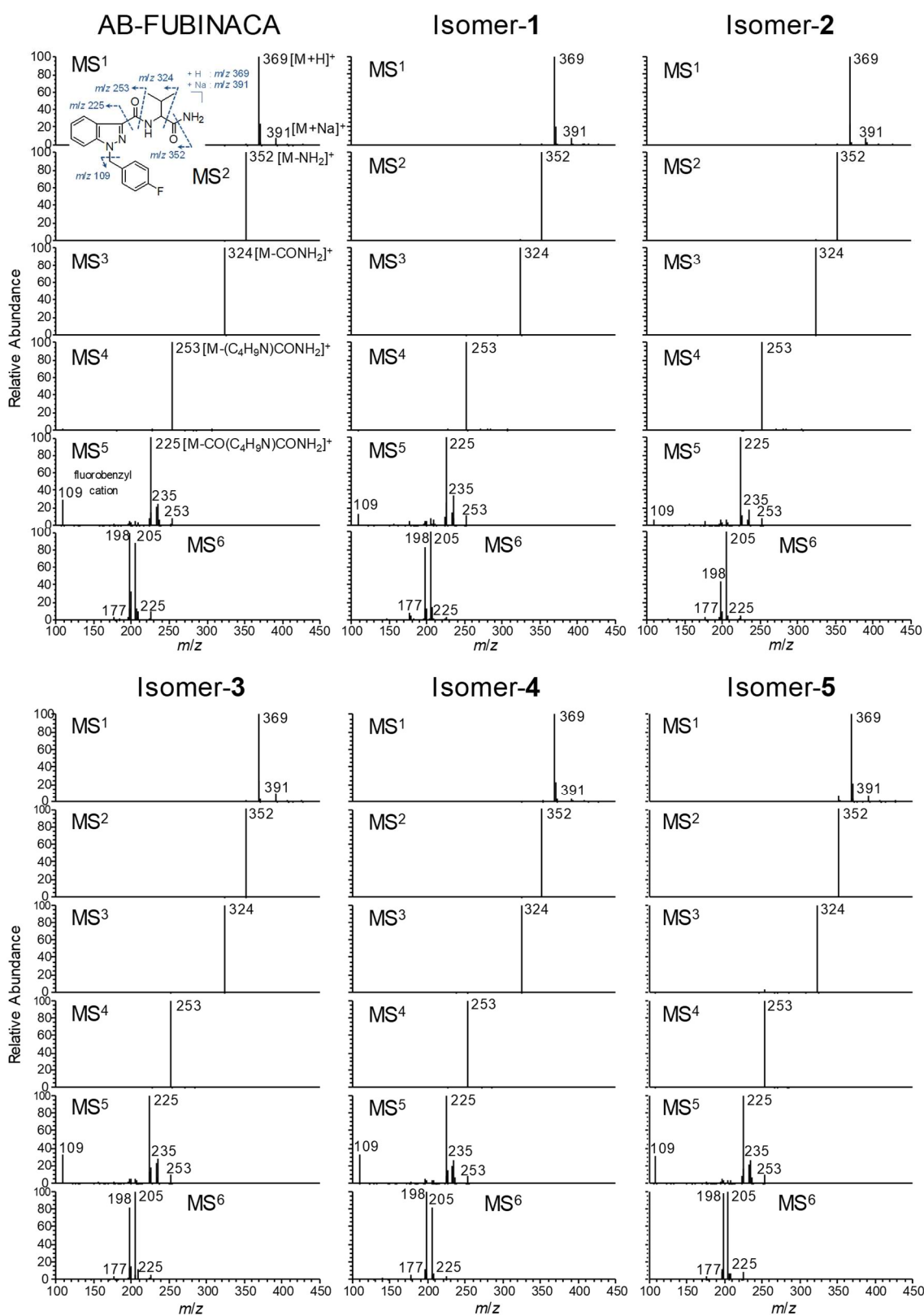


Fig. 4.3 ESI-LIT mass spectra at the MS¹–MS⁶ stages of AB-FUBINACA and its five positional isomers in positive mode. The precursor ions at the MS²–MS⁶ stages were set at *m/z* 369, 352, 324, 253, and 225, respectively.

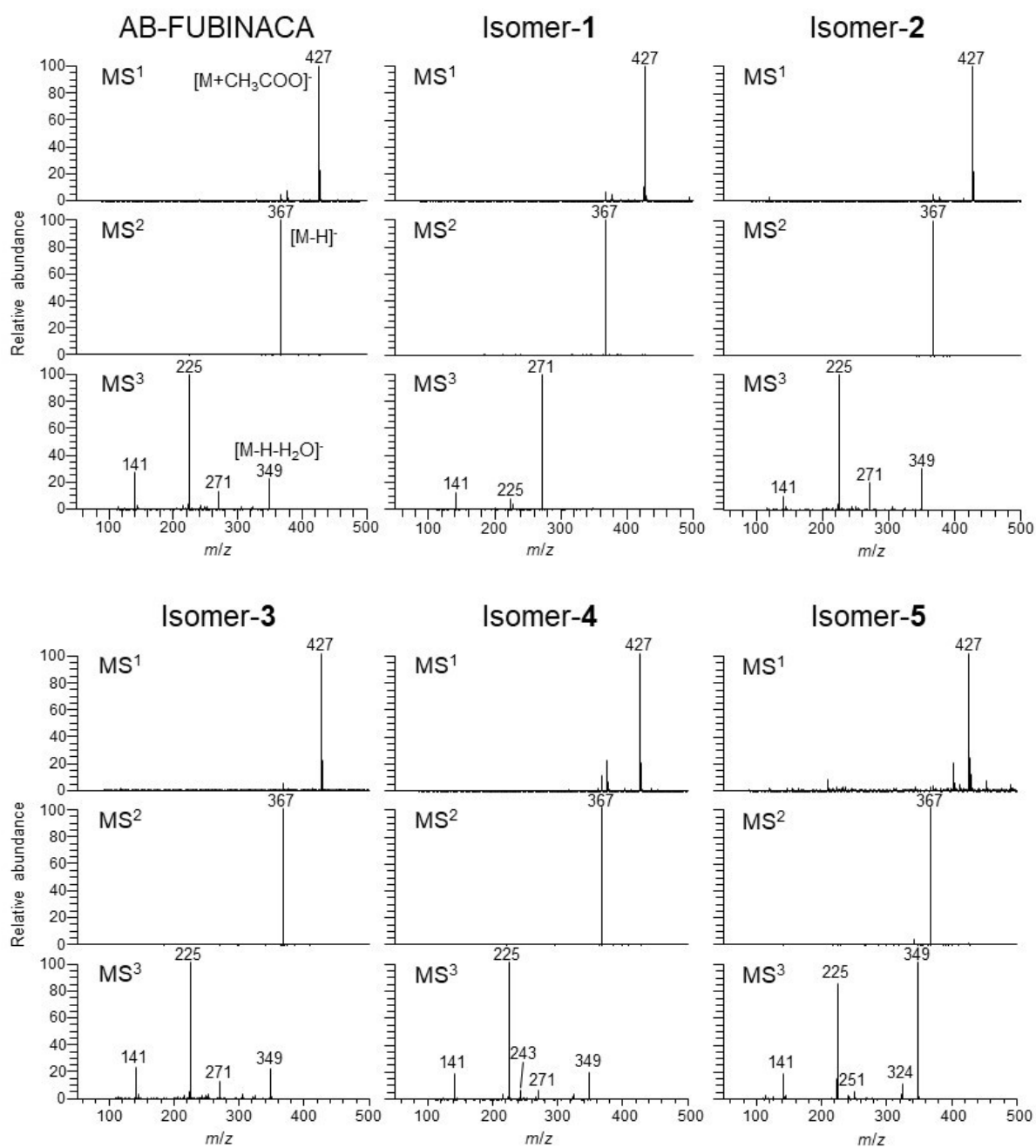


Fig. 4.4 ESI-LIT mass spectra at the MS¹–MS³ stages of AB-FUBINACA and its five positional isomers in negative mode. The precursor ions at the MS² and MS³ stages were set at *m/z* 427 and 367, respectively.

4.3.3 Triple quadrupole energy-resolved mass spectrometry

QqQ-MS provides good control over the kinetic energies of the ions by controlling the given CE [87]. The ERMS strategy makes it possible to reveal the behaviors of product ions. The product ion spectra for the precursor ions at m/z 369 were measured with the CE setting at 0–90 eV (0–40 eV in increments of 5 eV, and 50, 70, and 90 eV). All the obtained spectra are shown in Fig. 4.5. As a reference, the breakdown curves are shown in Fig. 4.6. The observed product ions for the six isomers at all CEs were identical. However, careful comparison of the relative abundances of the product ions enabled us to determine the dissociation characteristics of each isomer. As seen in the spectra at 0 and 5 eV, the relative abundances of the two ions at m/z 352 and 369 of isomer-5 were clearly different from the other isomers. This indicates that it was easier to eliminate the terminal amine in the carboxamide side chain of the precursor ion at m/z 369 of isomer-5, because the dissociation energy from m/z 369 to 352 was lower than the other isomers due to methylation of the amine in the amido bond. Among the four isomers except isomer-5, the relative abundance of the m/z 352 ion for isomer-4 was the highest at a CE of 0 eV and those of the m/z 324 and 369 ions were lowest at 5 eV. AB-FUBINACA, and isomers-1, -2, and -3 exhibited minimal differences in their spectra at 0 and 5 eV. The relative abundance of the m/z 324 ion of isomer-5 at 10 eV was much lower than that of the other isomers, indicating that isomer-5 required the highest dissociation energy to eliminate the carbonyl group from the m/z 352 ion. Comparing isomer-3 with isomer-4, the relative abundance of the m/z 352 ion of isomer-3 was lower at 10 eV, which suggested that the tertiary carbon–carbonyl carbon bond was easier to cleave than the quaternary carbon–carbonyl carbon bond. At a CE of 15 eV, the m/z 253 ion of the isomer-5 showed the highest abundance among the six isomers, suggesting that the m/z 253 ion was generated easily upon cleavage of the m/z 324 ion. Except for isomer-5, the relative abundances of the m/z 253 ions at 15 eV were in the order of AB-FUBINACA <

isomer-4 < isomer-3, whereas those of the m/z 324 ions at 20 eV were isomer-3 < isomer-4 < ABFUBINACA. Additionally, the relative abundances of the ions at m/z 109 and 253 varied among the three isomers at 20–50 eV. The abundances of the ions at m/z 109 and 253 were in the order of isomer-2 < isomer-1 < AB-FUBINACA at 20–35 eV and AB-FUBINACA < isomer-1 < isomer-2 at 40 and 50 eV, respectively. This ordering was due to the differences in energy required to cleave the fluorobenzyl group from the indazole moiety, attributed to a halogen electron-donating resonance effect [81].

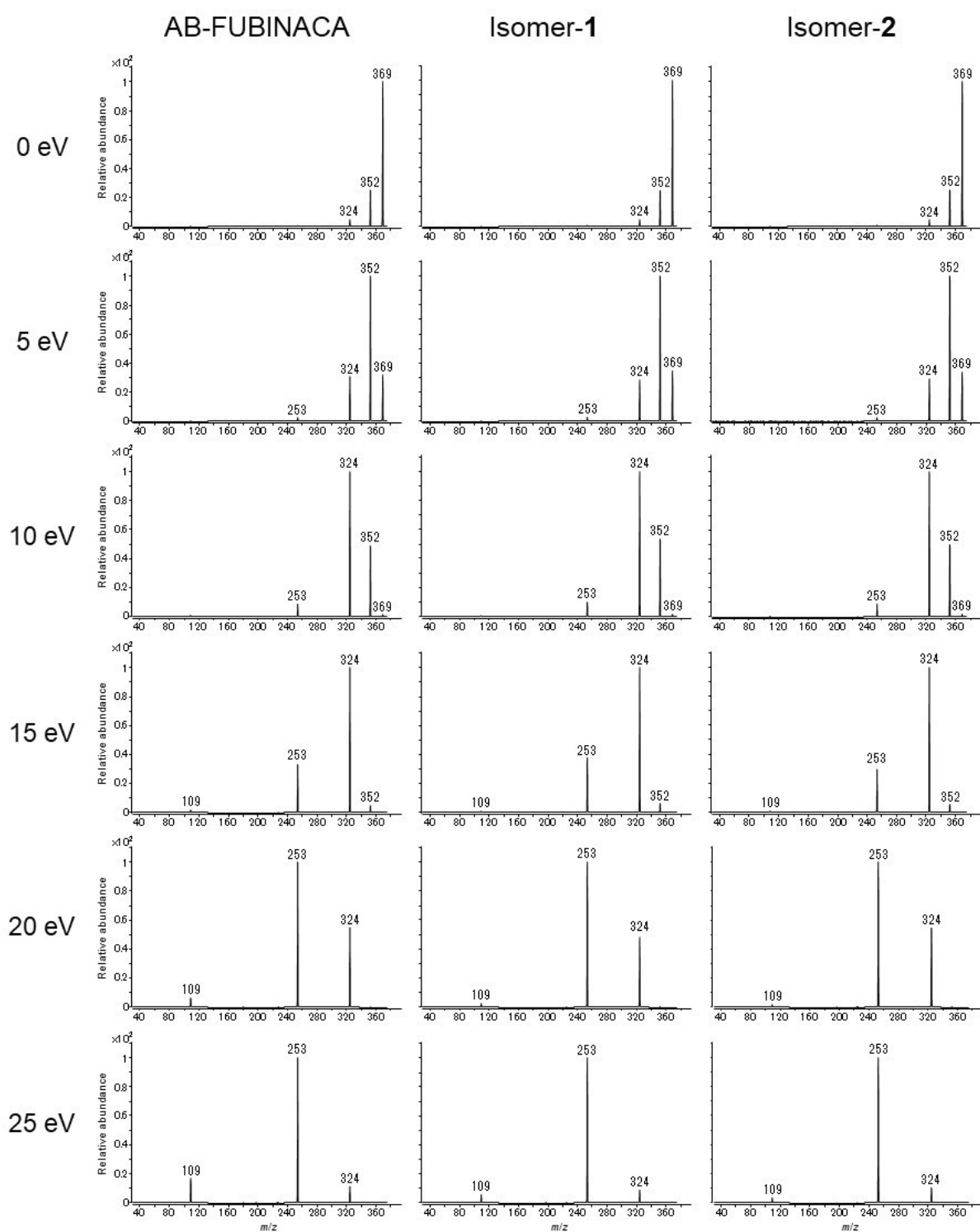


Fig. 4.5 ESI-QqQ mass spectra of AB-FUBINACA and its five positional isomers at CE of 0–90 eV for the precursor ions at m/z 369.

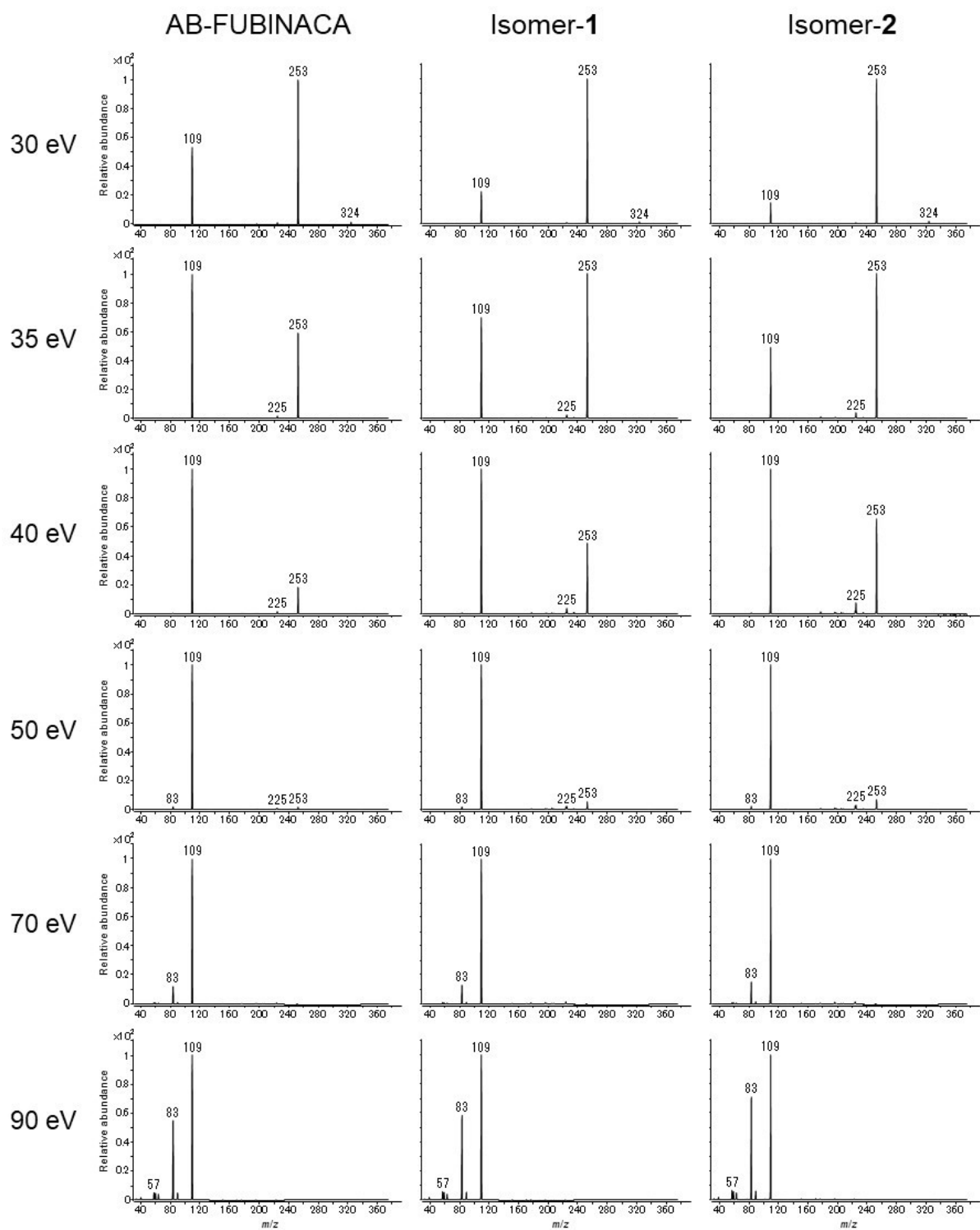


Fig. 4.5 Continued.

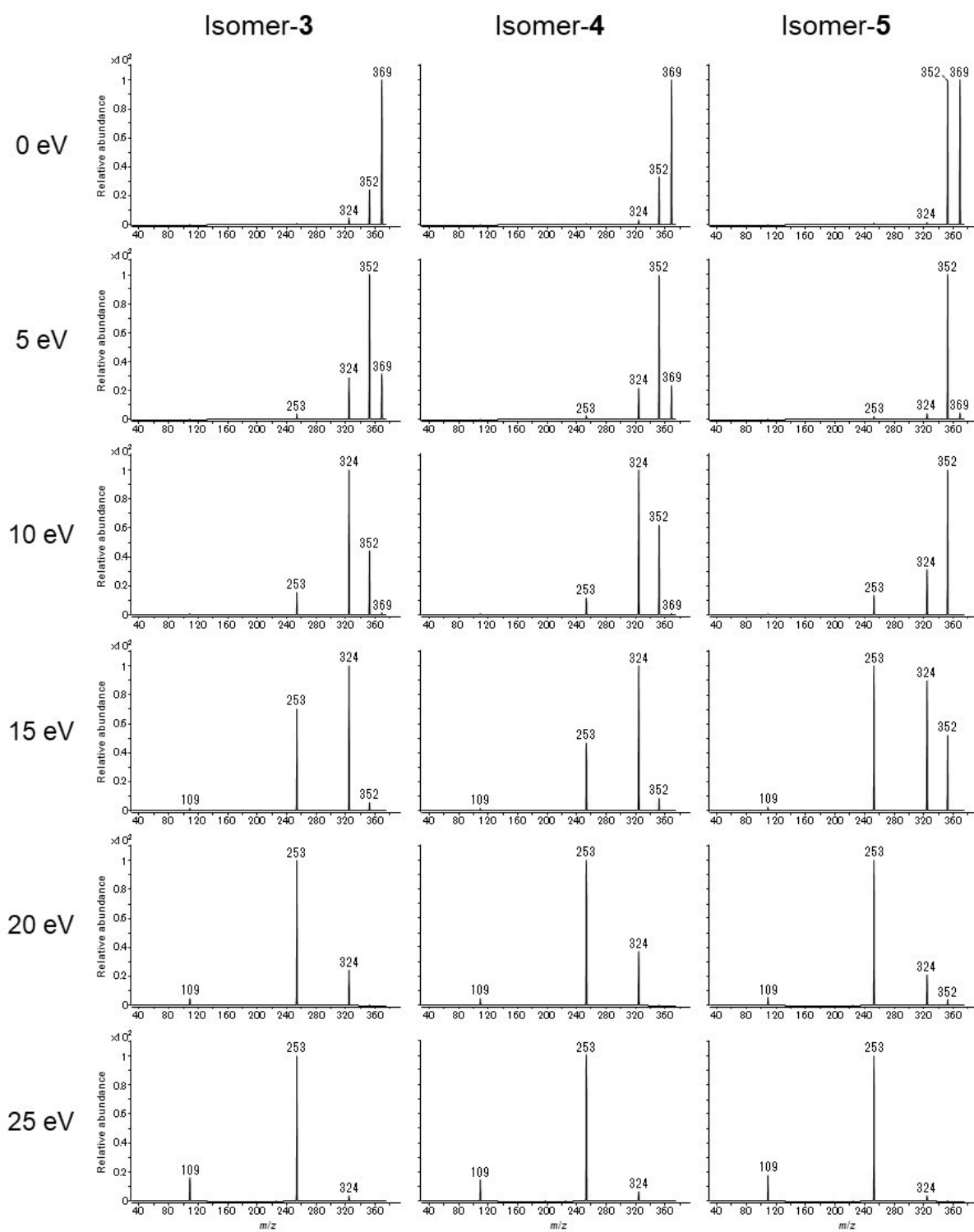


Fig. 4.5 Continued.

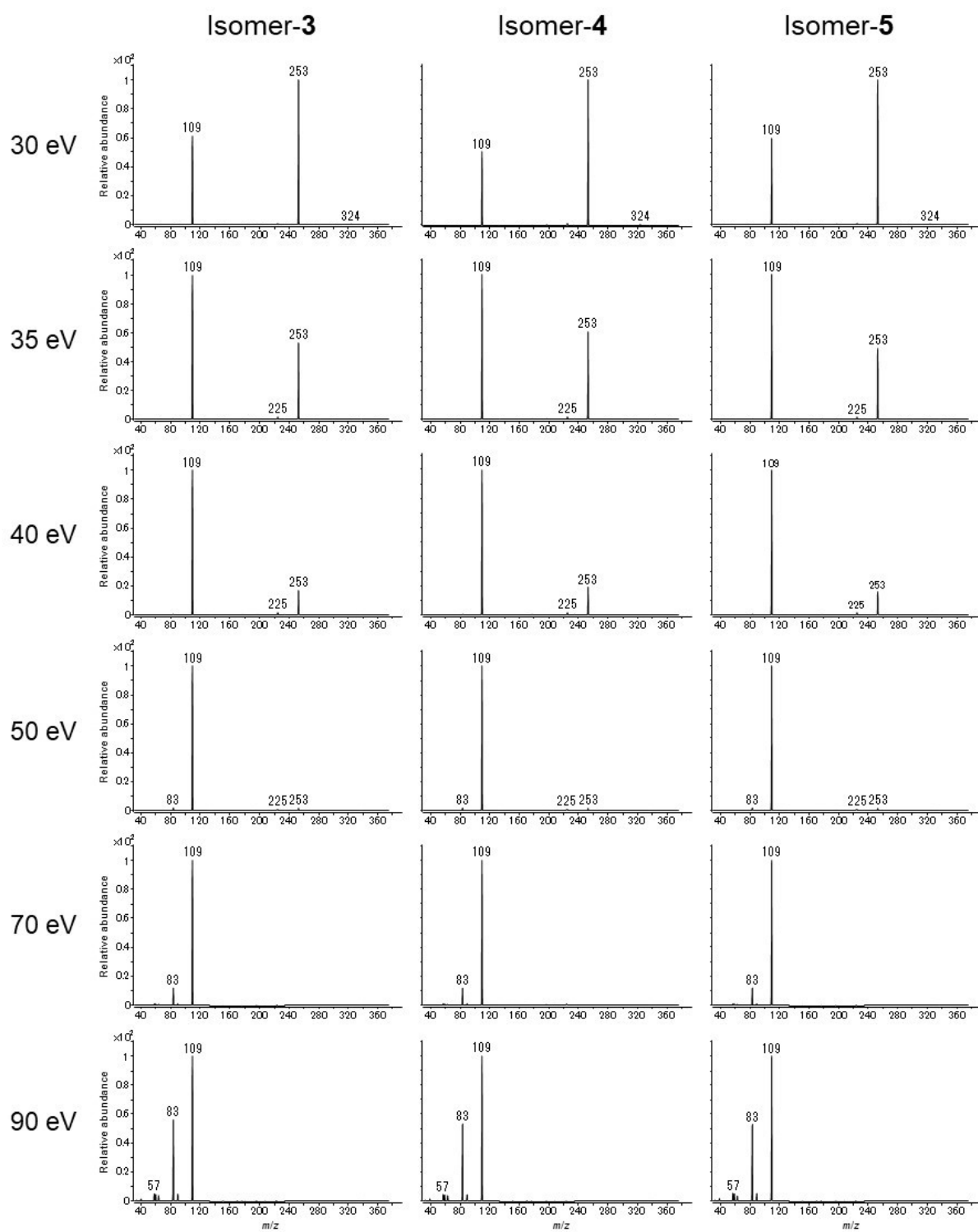


Fig. 4.5 Continued.

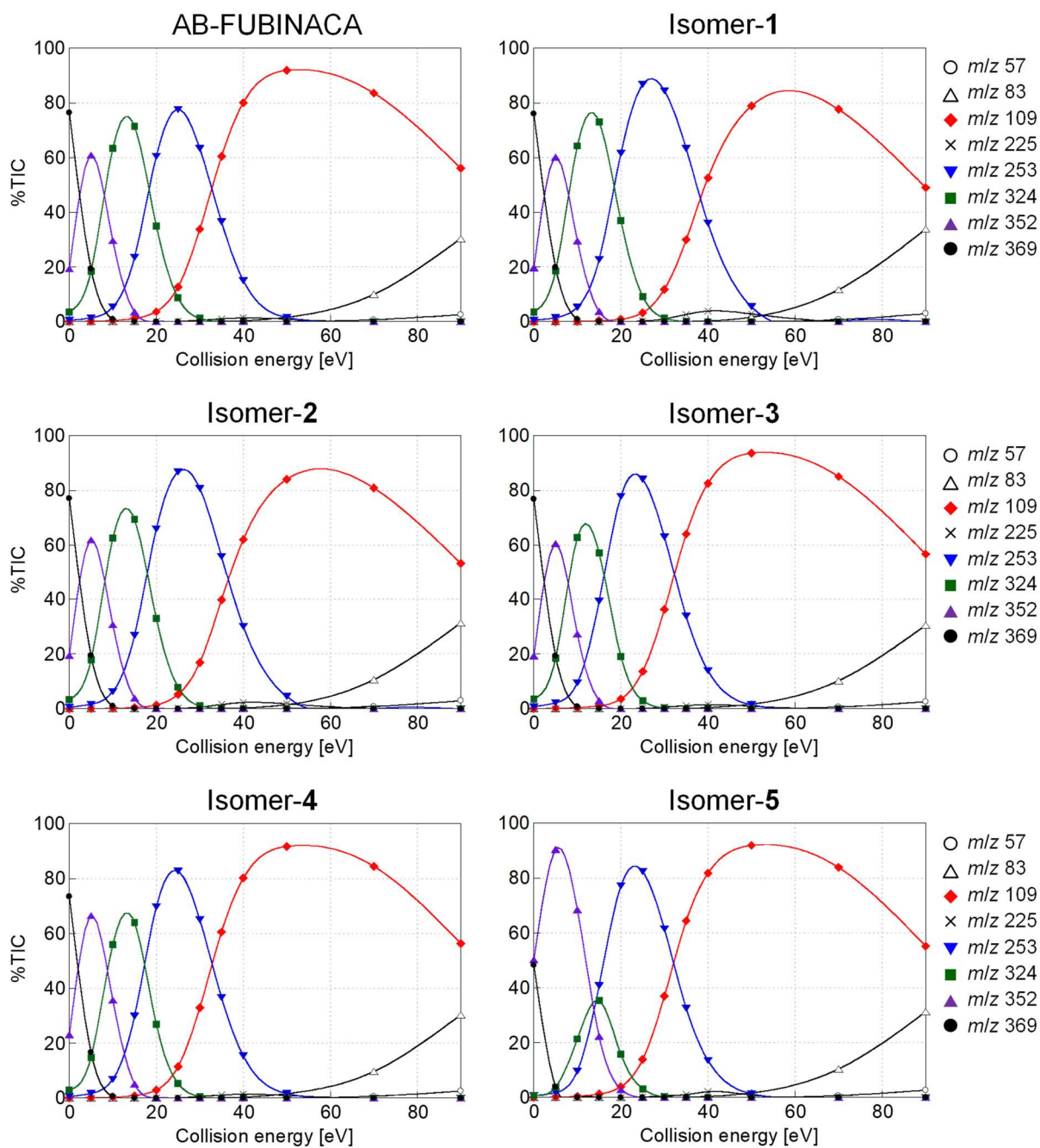


Fig. 4.6 Breakdown curves of AB-FUBINACA and its five positional isomers for the precursor ion at m/z 369.

To further clarify the abovementioned relationships, the natural logarithmic values of the abundance ratios of the product ions involved in CID reactions were plotted as a function of CE. First, the logarithmic values of the abundance ratio of the ion at m/z 352 to 369 [$\ln(A_{352}/A_{369})$] in the CE range of 0–10 eV for isomers-**3**, -**4**, and -**5** revealed the relation of isomer-**3** < isomer-**4** < isomer-**5** (Fig. 4.7a). To demonstrate significant differences among the $\ln(A_{352}/A_{369})$ values of the three isomers, the homogeneity of variance test, ANOVA, and multiple pairwise comparisons were performed. Bartlett's test for homogeneity of variances showed that the $\ln(A_{352}/A_{369})$ values at CEs of 0 and 5 eV were normally distributed (parametric) and the values at 10 eV were nonparametric. For the parametric data at 0 and 5 eV, one-way ANOVA showed significant differences in the $\ln(A_{352}/A_{369})$ values among the three isomers ($\alpha < 2.4 \times 10^{-17}$), and Tukey's test revealed low p values ($p < 1.7 \times 10^{-6}$) (Table 4.1). For the nonparametric data at 10 eV, the Kruskal-Wallis test followed by the Steel-Dwass test also showed that the three isomers were significantly different ($\alpha = 1.9 \times 10^{-3}$, $p < 2.5 \times 10^{-2}$, Table 4.1). Second, the logarithmic values of the product ion abundance ratio of m/z 324 to 352 [$\ln(A_{324}/A_{352})$] for isomers-**3**, -**4**, and -**5** were plotted in the CE range of 5–20 eV. The $\ln(A_{324}/A_{352})$ plots were also significantly separated in the order of isomer-**5** < isomer-**4** < isomer-**3** (Fig. 4.7b and Table 4.2). Third, the logarithmic values of the abundance ratio of m/z 253 to 324 [$\ln(A_{253}/A_{324})$] in 15–30 eV for AB-FUBINACA, isomer-**3**, and isomer-**4** were plotted and showed significant differences in the order of AB-FUBINACA < isomer-**4** < isomer-**3** (Fig. 4.7c and Table 4.3). Lastly, the logarithmic values of the abundance ratio of m/z 109 to 253 [$\ln(A_{109}/A_{253})$] for AB-FUBINACA, isomer-**1**, and isomer-**2** showed a significant relationship of isomer-**2** < isomer-**1** < AB-FUBINACA in the CE range of 20–50 eV (Fig. 4.7d and Table 4.4), which agrees with the previous analyses using GC/EI-QqQ-MS (Chapters 2 and 3), although the different ionization techniques were used [81,86]. The logarithmic values of the abundance ratio for the five isomers, except isomer-**5**,

revealed a linear relationship with the CE with high correlation coefficients (Fig. 4.7). The reliabilities of the data were ensured by good repeatability of the mass spectral data. The relative standard deviations of the abundances of the product ions were low (Tables 4.5–4.8), although some data such as m/z 369 at 10 eV for isomer-5 in Table 4.5, m/z 352 at 20 eV for isomer-3 in Table 4.6, and m/z 324 at 30 eV for isomer-3 in Table 4.7 were comparatively dispersed, because of their low abundance. Twice the standard deviations of the logarithmic values were also very low (Tables 4.5–4.8). Therefore, comparing the logarithmic values at each range of CEs enabled the six isomers to be differentiated clearly and reliably.

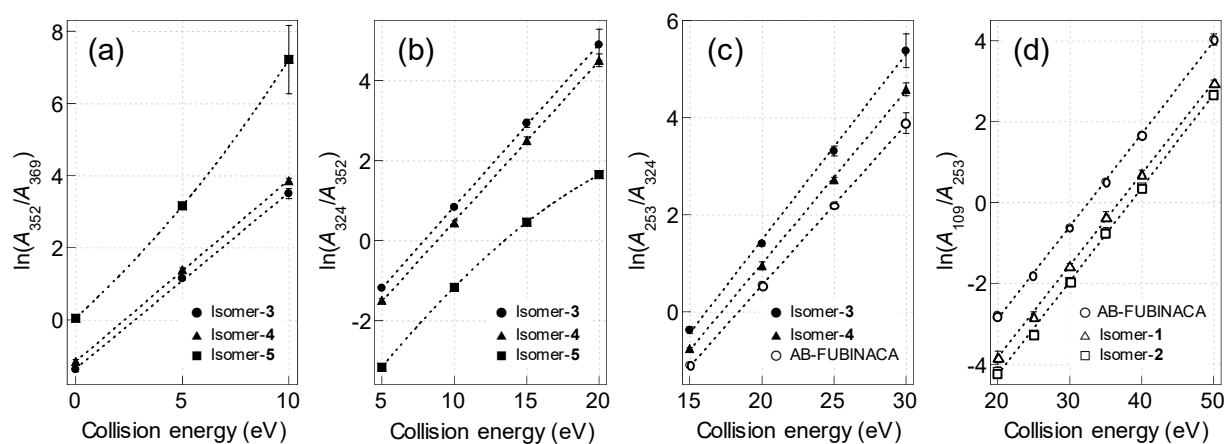


Fig. 4.7 Logarithmic plots of the abundance ratios of (a) m/z 352 to 369 at CEs of 0–10 eV for isomer-3, -4, and -5, (b) m/z 324 to 352 at 5–20 eV for isomer-3, -4, and -5, (c) m/z 253 to 324 at 15–30 eV for AB-FUBINACA, isomer-3, and isomer-4, and (d) m/z 109 to 253 at 20–50 eV for AB-FUBINACA, isomer-1, and isomer-2. Error bars represent twice the standard errors ($n = 5$).

Table 4.1 Analysis of variance (ANOVA) and multiple pairwise comparisons of the logarithmic values of the abundance ratio of m/z 352 to 369 [$\ln(A_{352}/A_{369})$] for isomers-**3**, **-4**, and **-5**.

CE (eV)	ANOVA ^a (α)	Multiple pairwise comparisons ^b (p)		
		Isomer- 3 \times -4	Isomer- 3 \times -5	Isomer- 4 \times -5
0	2.4×10^{-17}	1.8×10^{-6}	1.7×10^{-6}	1.7×10^{-6}
5	2.0×10^{-18}	2.0×10^{-6}	1.7×10^{-6}	1.7×10^{-6}
10	1.9×10^{-3}	2.5×10^{-2}	2.5×10^{-2}	2.5×10^{-2}

^a one-way ANOVA (0 and 5 eV), Kruskal-Wallis test (10 eV)

^b Tukey's test (0 and 5 eV), Steel-Dwass test (10 eV)

Table 4.2 Analysis of variance (ANOVA) and multiple pairwise comparisons of the logarithmic values of the abundance ratio of m/z 324 to 352 [$\ln(A_{324}/A_{352})$] for isomers-**3**, **-4**, and **-5**.

CE (eV)	ANOVA ^a (α)	Multiple pairwise comparisons ^b (p)		
		Isomer- 3 \times -4	Isomer- 3 \times -5	Isomer- 4 \times -5
5	1.7×10^{-18}	1.7×10^{-6}	1.7×10^{-6}	1.7×10^{-6}
10	2.9×10^{-20}	1.7×10^{-6}	1.7×10^{-6}	1.7×10^{-6}
15	1.5×10^{-17}	1.7×10^{-6}	1.7×10^{-6}	1.7×10^{-6}
20	1.9×10^{-3}	2.5×10^{-2}	2.5×10^{-2}	2.5×10^{-2}

^a one-way ANOVA (5, 10, and 15 eV), Kruskal-Wallis test (20 eV)

^b Tukey's test (5, 10, and 15 eV), Steel-Dwass test (20 eV)

Table 4.3 Analysis of variance (ANOVA) and multiple pairwise comparisons of the logarithmic values of the abundance ratio of m/z 253 to 324 [$\ln(A_{253}/A_{324})$] for AB-FUBINACA, isomer-3, and isomer-4.

CE (eV)	ANOVA ^a (α)	Multiple pairwise comparisons ^b (p)		
		AB-FUBINACA × isomer-3	AB-FUBINACA × isomer-4	Isomer-3 × -4
15	1.2×10^{-14}	1.7×10^{-6}	1.7×10^{-6}	1.7×10^{-6}
20	1.2×10^{-13}	1.7×10^{-6}	1.7×10^{-6}	1.7×10^{-6}
25	8.1×10^{-15}	1.7×10^{-6}	1.7×10^{-6}	1.7×10^{-6}
30	1.1×10^{-9}	1.7×10^{-6}	5.1×10^{-6}	2.6×10^{-6}

^a one-way ANOVA

^b Tukey's test

Table 4.4 Analysis of variance (ANOVA) and multiple pairwise comparisons of the logarithmic values of the abundance ratio of m/z 109 to 253 [$\ln(A_{109}/A_{253})$] for AB-FUBINACA, isomer-1, and isomer-2.

CE (eV)	ANOVA ^a (α)	Multiple pairwise comparisons ^b (p)		
		AB-FUBINACA × isomer-1	AB-FUBINACA × isomer-2	Isomer-1 × -2
20	9.6×10^{-14}	1.7×10^{-6}	1.7×10^{-6}	2.6×10^{-6}
25	4.5×10^{-16}	1.7×10^{-6}	1.7×10^{-6}	1.7×10^{-6}
30	4.2×10^{-15}	1.7×10^{-6}	1.7×10^{-6}	1.7×10^{-6}
35	7.1×10^{-14}	1.7×10^{-6}	1.7×10^{-6}	1.8×10^{-6}
40	2.9×10^{-16}	1.7×10^{-6}	1.7×10^{-6}	1.7×10^{-6}
50	2.3×10^{-14}	1.7×10^{-6}	1.7×10^{-6}	8.6×10^{-6}

^a one-way ANOVA

^b Tukey's test

Table 4.5 Relative standard deviations (RSDs) of the abundances of the m/z 352 and 369 ions and the logarithmic values of the abundance ratios [$\ln(A_{352}/A_{369})$] with twice the standard deviation (2SD) at CEs of 0–10 eV for isomers-**3**, **-4**, and **-5**.

CE (eV)	Isomer-3			Isomer-4			Isomer-5		
	RSD (%)		$\ln(A_{352}/A_{369})$ $\pm 2SD$	RSD (%)		$\ln(A_{352}/A_{369})$ $\pm 2SD$	RSD (%)		$\ln(A_{352}/A_{369})$ $\pm 2SD$
	m/z 352	m/z 369		m/z 352	m/z 369		m/z 352	m/z 369	
0	2.2	2.6	-1.38 ± 0.06	3.4	1.9	-1.15 ± 0.06	2.2	3.4	0.04 ± 0.05
5	2.2	3.0	1.15 ± 0.04	1.1	1.9	1.38 ± 0.06	1.5	4.9	3.15 ± 0.09
10	2.8	8.6	3.50 ± 0.14	2.4	3.6	3.86 ± 0.06	2.5	47	7.21 ± 0.95

Table 4.6 Relative standard deviations (RSDs) of the abundances of the m/z 324 and 352 ions and the logarithmic values of the abundance ratios [$\ln(A_{324}/A_{352})$] with twice the standard deviation (2SD) at CEs of 5–20 eV for isomers-**3**, **-4**, and **-5**.

CE (eV)	Isomer-3			Isomer-4			Isomer-5		
	RSD (%)		$\ln(A_{324}/A_{352})$ $\pm 2SD$	RSD (%)		$\ln(A_{324}/A_{352})$ $\pm 2SD$	RSD (%)		$\ln(A_{324}/A_{352})$ $\pm 2SD$
	m/z 324	m/z 352		m/z 324	m/z 352		m/z 324	m/z 352	
5	2.1	2.2	-1.19 ± 0.03	3.4	1.1	-1.50 ± 0.05	5.0	1.5	-3.16 ± 0.09
10	2.8	2.8	0.83 ± 0.03	2.6	2.4	0.45 ± 0.04	1.6	2.5	-1.17 ± 0.06
15	1.6	6.1	2.93 ± 0.10	2.9	2.4	2.50 ± 0.09	3.1	3.7	0.46 ± 0.09
20	3.0	20	4.96 ± 0.39	1.5	8.1	4.50 ± 0.16	2.8	4.4	1.65 ± 0.08

Table 4.7 Relative standard deviations (RSDs) of the abundances of the m/z 253 and 324 ions and the logarithmic values of the abundance ratios [$\ln(A_{253}/A_{324})$] with twice the standard deviation (2SD) at CEs of 15–30 eV for AB-FUBINACA, isomer-**3**, and isomer-**4**.

CE (eV)	AB-FUBINACA			Isomer-3			Isomer-4		
	RSD (%)		$\ln(A_{253}/A_{324})$ $\pm 2SD$	RSD (%)		$\ln(A_{253}/A_{324})$ $\pm 2SD$	RSD (%)		$\ln(A_{253}/A_{324})$ $\pm 2SD$
	m/z 253	m/z 324		m/z 253	m/z 324		m/z 253	m/z 324	
15	1.8	2.6	-1.11 ± 0.04	3.9	1.6	-0.38 ± 0.06	3.6	2.8	-0.76 ± 0.03
20	1.8	2.8	0.54 ± 0.07	2.1	3.0	1.40 ± 0.05	4.2	1.5	0.95 ± 0.08
25	1.6	1.1	2.18 ± 0.05	3.9	4.5	3.31 ± 0.10	2.1	0.9	2.72 ± 0.04
30	2.9	8.0	3.89 ± 0.21	2.4	16	5.37 ± 0.35	0.9	6.5	4.58 ± 0.13

Table 4.8 Relative standard deviations (RSDs) of the abundances of the m/z 109 and 253 ions and the logarithmic values of the abundance ratios [$\ln(A_{109}/A_{253})$] with twice the standard deviation (2SD) at CEs of 20–50 eV for AB-FUBINACA, isomer-1, and isomer-2.

CE (eV)	Isomer-3			Isomer-4			Isomer-5		
	RSD (%)		$\ln(A_{109}/A_{253})$ $\pm 2SD$	RSD (%)		$\ln(A_{109}/A_{253})$ $\pm 2SD$	RSD (%)		$\ln(A_{109}/A_{253})$ $\pm 2SD$
	m/z 109	m/z 253		m/z 109	m/z 253		m/z 109	m/z 253	
20	4.1	1.8	-2.78 ± 0.06	6.6	3.0	-3.82 ± 0.14	8.0	2.6	-4.17 ± 0.11
25	2.1	1.6	-1.81 ± 0.03	4.4	1.7	-2.79 ± 0.09	2.5	3.3	-3.26 ± 0.08
30	2.0	2.9	-0.63 ± 0.07	2.4	1.6	-1.55 ± 0.06	4.6	2.3	-1.96 ± 0.11
35	2.6	1.4	0.50 ± 0.03	6.4	1.5	-0.39 ± 0.11	4.2	4.4	-0.79 ± 0.12
40	3.2	2.1	1.67 ± 0.04	3.6	0.8	0.73 ± 0.08	3.8	3.4	0.38 ± 0.06
50	1.7	6.8	4.05 ± 0.14	1.3	5.2	2.93 ± 0.09	2.7	3.1	2.67 ± 0.04

4.4 Summary

Differences between AB-FUBINACA and its five positional isomers (two fluorine positional (*ortho* and *meta*) isomers on the phenyl ring and three methyl positional isomers in the carboxamide side chain) were investigated by LC/ESI-LIT-MS and LC/ESI-QqQ-MS. Excluding AB-FUBINACA and its *meta* isomer, four isomers were separated using an ODS column in isocratic mode. Multiple-stage MS using LIT in negative mode allowed the three isomers, namely, the *ortho*-fluorine isomer, the *N*-(1-amino-2-methyl-1-oxobutan-2-yl) isomer, and the *N*-(1-amino-1-oxobutan-2-yl)-*N*-methyl isomer, to be differentiated based on their characteristic product ions observed in the MS³ stage. ERMS, which employs QqQ-MS as a function of CE, revealed that the relative abundance of the product ions containing the positional isomeric moieties produced by CID reactions differed for all six isomers. Furthermore, all six isomers were clearly differentiated by the logarithmic values of their characteristic product ion abundance ratios as a function of CE. Based on these results, the combination of LC with ESI-QqQ-MS was effective for differentiation of a series of AB-FUBINACA positional isomers.

Chapter 5

Differentiation of the fluorine substitution position on the phenyl ring of fluoromethcathinones using energy-resolved mass spectrometry

5.1 Introduction

Fluoromethcathinone is a synthetic analog of β -ketomethylamphetamine (methcathinone), in which the aromatic ring contains a fluorine substituent. The two positional isomers, i.e. 4-fluoromethcathinone (flephedrone, *p*-FMC) and 3-fluoromethcathinone (*m*-FMC), were first reported to the EMCDDA in September and October 2008 in Denmark and the United Kingdom, respectively [88–90]. To avoid the prevalence of these isomeric compounds, as recommended by the UK home office from the ACMD, *o*-, *m*-, and *p*-FMCs have been controlled in the United Kingdom as class B drugs since April 2010 under the Misuse of Drugs Act 1971 by a blanket scheduling of synthetic cathinones through the introduction of a generic legislation based on modifications to certain core structures [91]. In Japan, *m*- and *p*-FMC were listed as “designated substances” under the Pharmaceutical and Medical Devices Act in May 2011 and October 2011, respectively. In January 2014, all FMC positional isomers, including *o*-FMC, were scheduled by a generic definition similar to the UK scheduling. Moreover, in the United States, the DEA temporarily scheduled the optical, positional, and geometric isomers of FMC into schedule I of the Controlled Substances Act (CSA) in March 2014 [92] and then determined to permanently control them as schedule I substances in March 2017 [93].

Although the FMC isomers are now all illegal in many countries, forensic analysts must differentiate between positional isomers, because they are required to guarantee the analytical reliability and accuracy by unambiguously identifying the exact structure in criminal procedures and in court. However, it is difficult to distinguish the three FMC positional

isomers, because they exhibit similar retention properties in chromatography and have almost identical mass spectra [94]. In addition, their differentiation is difficult even using ion mobility spectrometry due to their similar collision cross sections. To overcome these limitations, several research groups have attempted to develop spectroscopic, spectrometric, and/or chromatographic techniques for the differentiation of the isomers [39,90,95,96]. In Chapters 2–4, a procedure for differentiating the fluorine substitution position on the phenyl ring in synthetic cannabinoids was developed using ERMS based on the difference in the abundance ratios of characteristic product ions as a function of CE [81,86,97]. We expected that this method could also be applied to the differentiation of FMC positional isomers. Herein, ERMS was performed using GC/EI-QqQ-MS to differentiate the three FMC positional isomers and theoretical dissociation energy calculations along with additional ERMS measurements of methylnmethcathinones (MMCs) to determine the cause of the differences among the three FMC isomers obtained by ERMS. Furthermore, the effectiveness of the developed method was confirmed using actual forensic samples.

5.2 Material and Methods

5.2.1 Reagents

2-(Methylamino)-1-(2-, 3-, and 4-fluorophenyl)-1-propanones (2-, 3-, and 4-fluoromethcathinones; *o*-, *m*-, and *p*-FMCs) and 2-(methylamino)-1-(2-, 3-, and 4-methylphenyl)-1-propanones (2-, 3-, and 4-methylmethcathinones; *o*-, *m*-, and *p*-MMCs) were purchased as their hydrochloride salts (purity \geq 98%) from Cayman Chemical (Ann Arbor, MI, USA). Trifluoroacetic anhydride (TFAA, purity \geq 98%) was purchased from Wako Pure Chemical Industries (Osaka, Japan).

Standard stock solutions of FMC positional isomers, as their corresponding hydrochloride salts, were prepared in methanol at concentrations of 200 μ g/mL and were stored at -20°C

prior to use. The working standard solutions for the injections into the mass spectrometer were prepared according to the following procedure. One hundred microliters of each standard stock solution was diluted with 900 μL of distilled water and was alkalinized with a few drops of 15% sodium carbonate aqueous solution followed by shaking with 1 mL of ethyl acetate on the vortex for 1 min. After centrifugation, the organic layer was separated and dried over anhydrous sodium sulfate, and the solvent was evaporated to obtain a solid residue. For the free-base sample, the aforementioned residue was redissolved in 1 mL of methanol to obtain samples that were subjected to GC/MS analysis. For the trifluoroacetyl (TFA)-derivatized sample, the residue was dissolved in 200 μL of ethyl acetate and 200 μL of TFAA, and the mixture was heated for 20 min at 50°C. After cooling it to room temperature, the mixture was evaporated, and the residue was redissolved in 1 mL of ethyl acetate to obtain samples that were subjected to GC/MS analysis. The MMC positional isomers were also TFA-derivatized following the same procedure.

5.2.2 Instrumentation

Mass spectra were obtained on a Shimadzu GCMS-TQ8040 spectrometer (Shimadzu, Kyoto, Japan) using an SH-Rxi-5SilMS fused-silica capillary column (30 m \times 0.25 mm i.d., 0.25- μm film thickness; Shimadzu). The inlet temperature was set at 200°C, the injection mode was split (1:5), and the sample injection volume was 1 μL . The carrier gas was high-purity helium (six nine-grade) at a constant column flow rate of 45.1 cm/s. The temperature program consisted of an initial temperature of 100°C, which was ramped up to 250°C at 20°C/min, followed by a hold at 250°C for 1 min. The transfer line was maintained at 250°C. The mass spectrometer was operated in the EI mode at 70 eV using an ion source temperature of 200°C. The acquisition of the full scan mode was in the range of m/z 40–350. The acquisition of the product ion scan mode for FMC was in the range of m/z 40–123 for the

precursor ions at m/z 123, and that for MMC was in the range of m/z 40–119 for the precursor ions at m/z 119. The argon gas pressure of the CID reaction was set to 200 kPa. The mass spectrometer was tuned according to the instrument protocol provided by the manufacturer as needed to realize acceptable quality. To avoid the effect of spectral skewing, the abundances of selected ions in the product ion spectra were taken as the areas of the mass chromatographic peaks. Individual data were fitted using the Boltzmann sigmoidal function with nonlinear regression analysis (Subsection 2.2.4 of Chapter 2).

5.2.3 Statistical and theoretical calculations

Statistical analysis was performed using BellCurve for Excel ver. 2.02 (Social Survey Research Information Co., Ltd., Tokyo, Japan), which is an add-in software to Microsoft Excel 2010. The homogeneity of variance was calculated by performing Bartlett's test to determine if the obtained data were normally distributed (parametric, $p > 0.05$) or not (nonparametric, $p < 0.05$). If the data were parametric, one-way ANOVA was conducted, followed by multiple pairwise comparisons as post hoc analysis using the Tukey's test [69,82]. For nonparametric data, the Kruskal-Wallis test (nonparametric ANOVA) was performed, followed by multiple pairwise comparisons using the Steel-Dwass test [83].

Quantum chemical calculations were performed with Gaussian 09 Rev. D (Gaussian, Inc., Wallingford, CT, USA). The geometries of all the studied compounds were optimized using DFT at the B3LYP/6-31G(d,p) level [70,71,98]. Each optimized structure was confirmed by frequency calculation to be the true energy minimum with the absence of imaginary vibration frequencies. The self-consistent field convergence required both $< 10^{-6}$ energy change and $< 10^{-8}$ root mean square change in the density matrix. No symmetry constraint was imposed in the optimization. The optimized structures were displayed using the Winmostar program ver. 8.001 (X-Ability Co., Ltd., Tokyo, Japan) [74]. The dissociation energy can be given as the

difference between the total free energy of the dissociated species and those of the precursor species, including the electronic energy and zero-point corrections generated from a vibrational frequency calculation [75].

5.3 Results and discussion

5.3.1 Full scan mass spectrometry

The obtained EI-full scan mass spectra of the free bases of *o*-, *m*-, and *p*-FMCs only exhibited a few common fragment ions, specifically m/z 58 (base peak), 75, 95, and 123 (Fig. 5.1a), because of their low molecular weights, high polarities, and high volatilities. The fragmentation of all the three compounds was dominated by α -cleavage next to the nitrogen atom to produce the iminium cation (m/z 58). The fragment ions at m/z 95 and 123 corresponded to the fluorophenyl and fluorobenzoyl cations, respectively. The ion at m/z 75

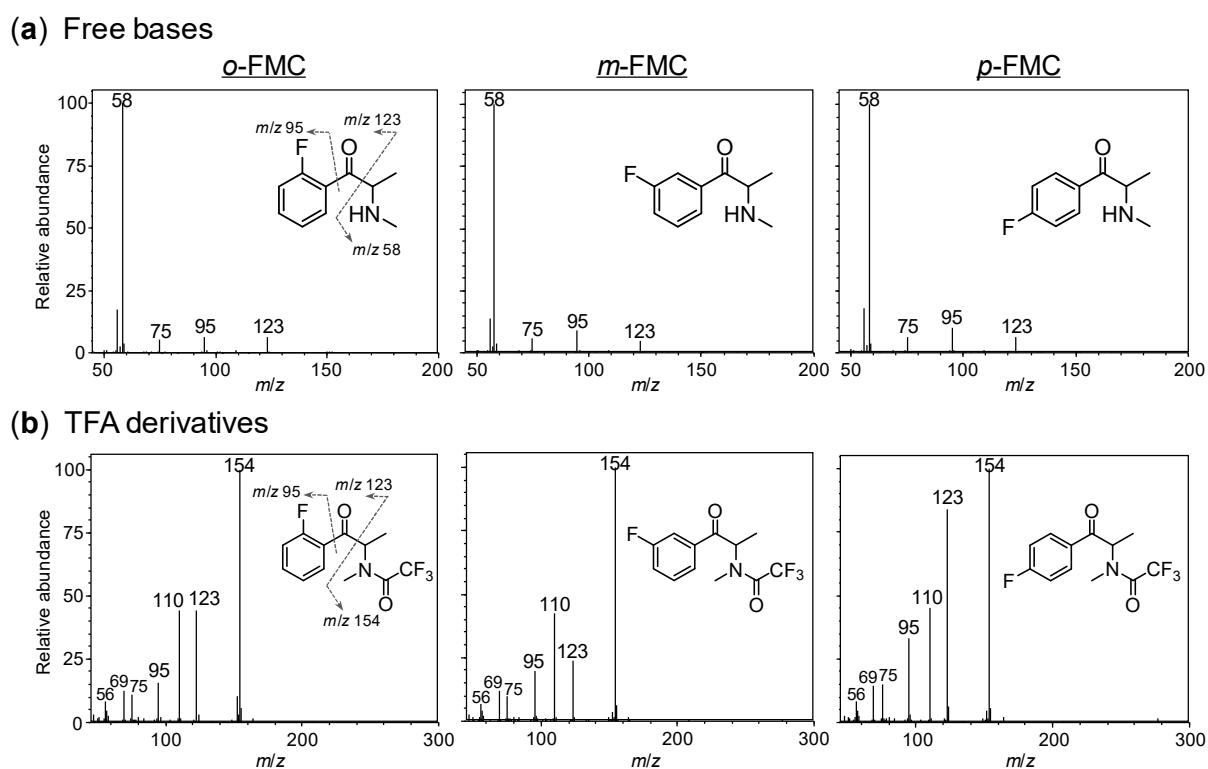


Fig. 5.1 EI-full scan mass spectra of (a) the free bases and (b) TFA derivatives of the FMC positional isomers.

could occur due to fluorine elimination from the m/z 95 ion. Notably, the three spectral patterns were very similar, and no diagnostic fragment ions were found that could be useful for differentiation.

Generally, derivatization can significantly enhance mass spectral sensitivity and alter fragmentation patterns by reducing the polarity and affecting the volatility [99,100]. Acylation techniques, such as trifluoroacetylation (TFA-derivatization), which is one of the most important derivatization techniques in forensic drug analysis, have been widely exploited for phenylethylamine-type drugs, including synthetic cathinones [101]. Full scan mass spectra of the TFA derivatives of the three FMC positional isomers exhibited the fragment ions at m/z 56, 69, 75, 95, 110, 123, and 154 (base peak), in which characteristic fragment ions, which enable differentiation of the isomers, were not found (Fig. 5.1b). However, the relative abundances of the ions at m/z 95 and 123 were varied among the three isomers, increasing in the following respective orders: *ortho* < *meta* < *para* and *meta* < *ortho* < *para*. These results indicated that the abundances of the peaks corresponding to the fluorophenyl and fluorobenzoyl cations depended on the fluorine substitution position on the phenyl ring.

5.3.2 Energy-resolved mass spectrometry

ERMS of the TFA derivatives of the three FMC positional isomers were performed for the precursor ions at m/z 123. The CE was 5 to 60 eV with increments of 5 eV. The obtained product ions were identical for the three isomers at all CEs, and no characteristic product ions were found for differentiation (Fig. 5.2). However, the three isomers differed from each other in terms of the relative abundances of the two ions at m/z 95 and 123 at the CEs of 5, 10, 15, and 20 eV.

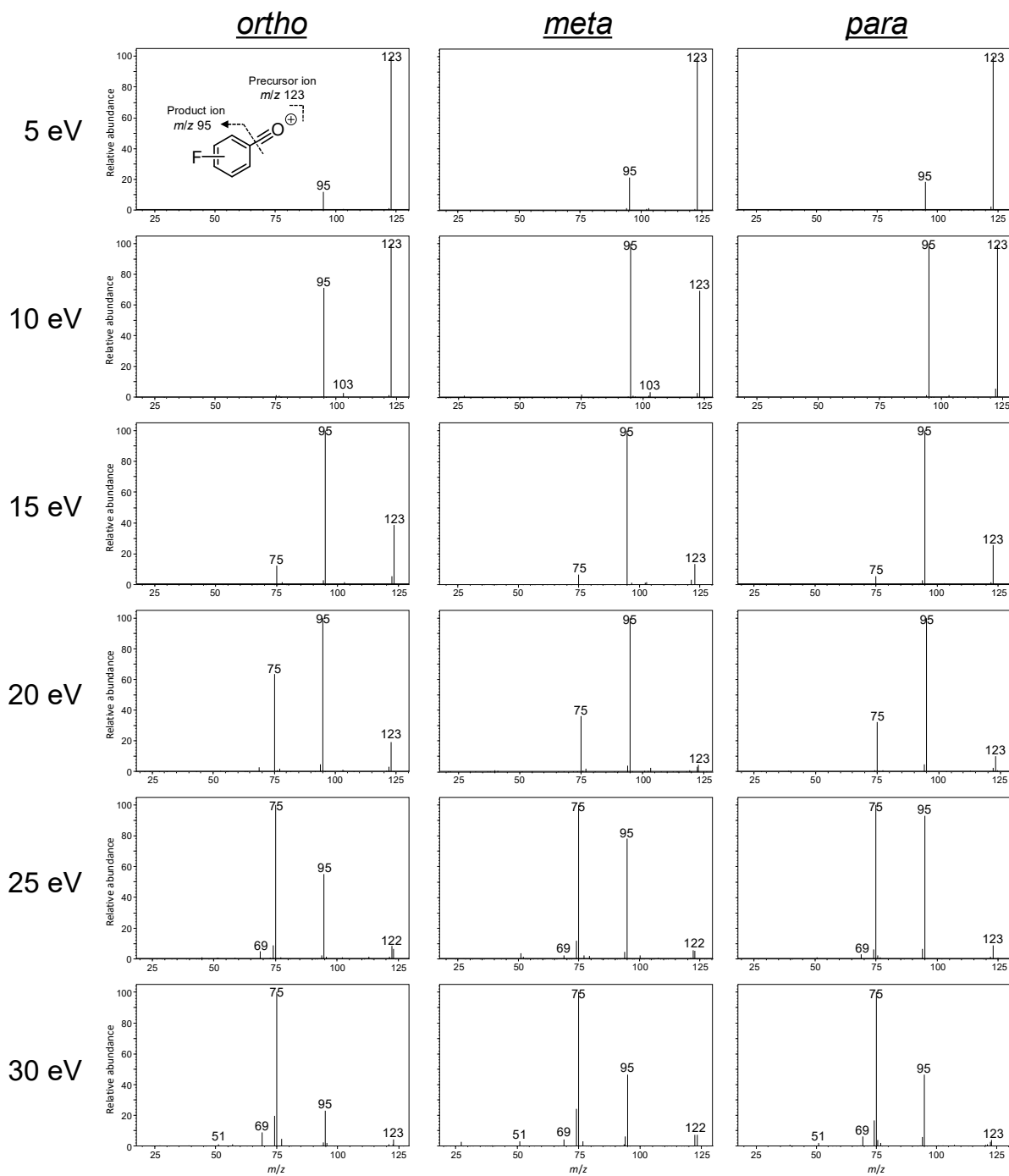


Fig. 5.2 Product ion spectra of the TFA derivatives of the FMC positional isomers. The precursor ion was set at m/z 123.

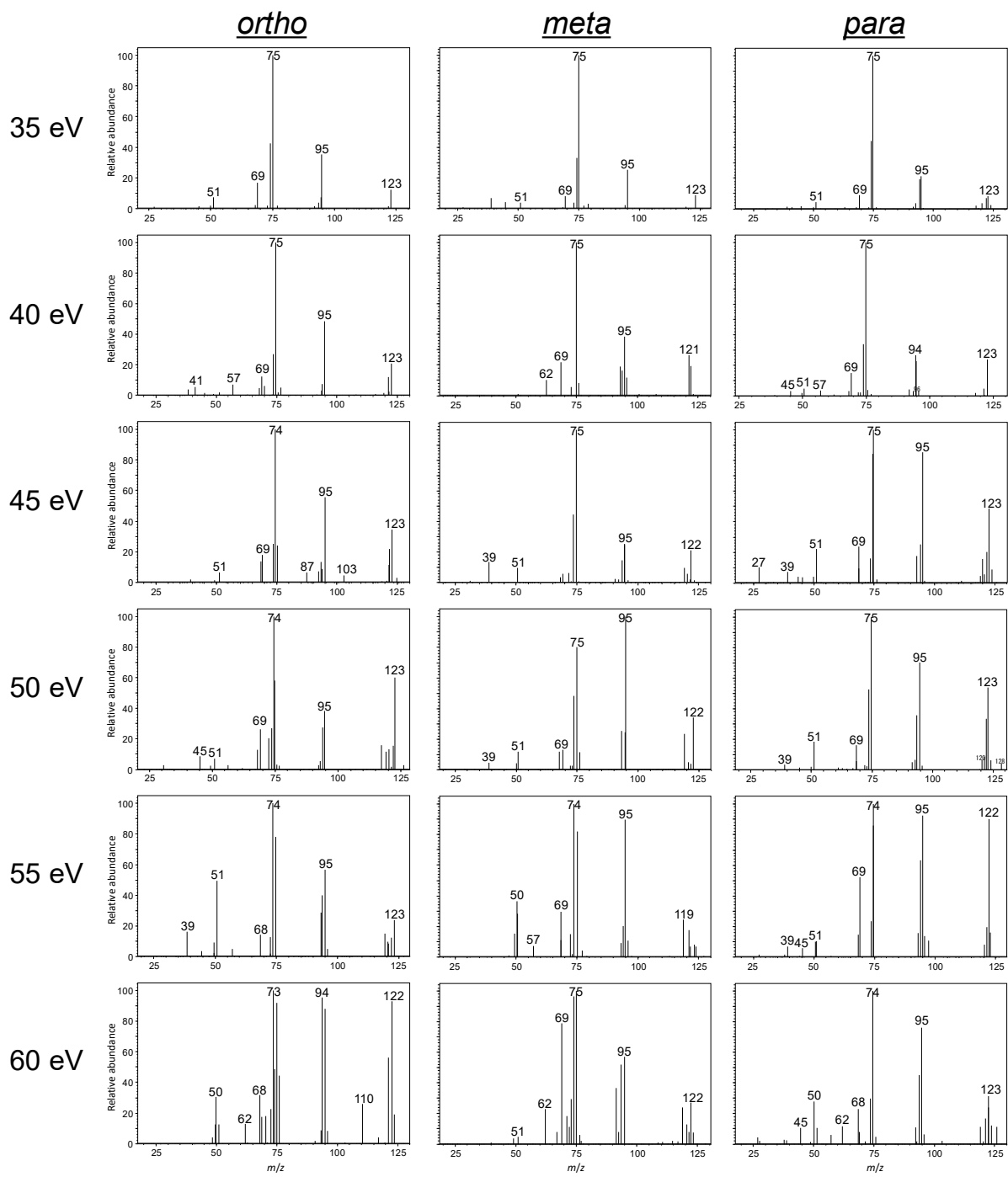


Fig. 5.2 Continued.

Based on the aforementioned results, the key ions for differentiation were m/z 95 and 123. To investigate the abundance differences in detail, ERMS was also performed with CE settings varying from 4 to 30 eV in increments of 2 eV. The breakdown curves showed that the CID reaction of the precursor ion at m/z 123 produced two major ions at m/z 75 and 95 (Fig. 5.3). The ion abundances at m/z 95 and 123 increased and decreased with increasing CE, respectively, and a further increase in CE to more than 16 eV resulted in a decrease in the abundance at m/z 95, leading to a simultaneous increase in the abundance at m/z 75. The abundances of the minor ions at m/z 51, 69, and 103 showed little changes in the CE range measured. These findings indicate that the CID reaction gave a consecutive reaction involving the elimination of CO and fluorine (m/z 123 \rightarrow m/z 95 \rightarrow m/z 75). The patterns of the three breakdown curves were similar, but the increase rate of m/z 95 and decrease rate of m/z 123 as a function of CE were different among the three isomers. This can also be understood from the differences in the CE values at the intersection point of the sigmoidal-shaped increase and decrease of the m/z 95 and m/z 123 curves. The breakdown curves were highly reproducible: The standard deviations of the two key ions at m/z 95 and 123, determined by the variabilities of the abundances (%TIC) at each CE, were < 3.6 and < 4.4 for intraday, and < 2.3 and < 2.8 for interday, respectively ($n = 6$, Tables 5.1 and 5.2).

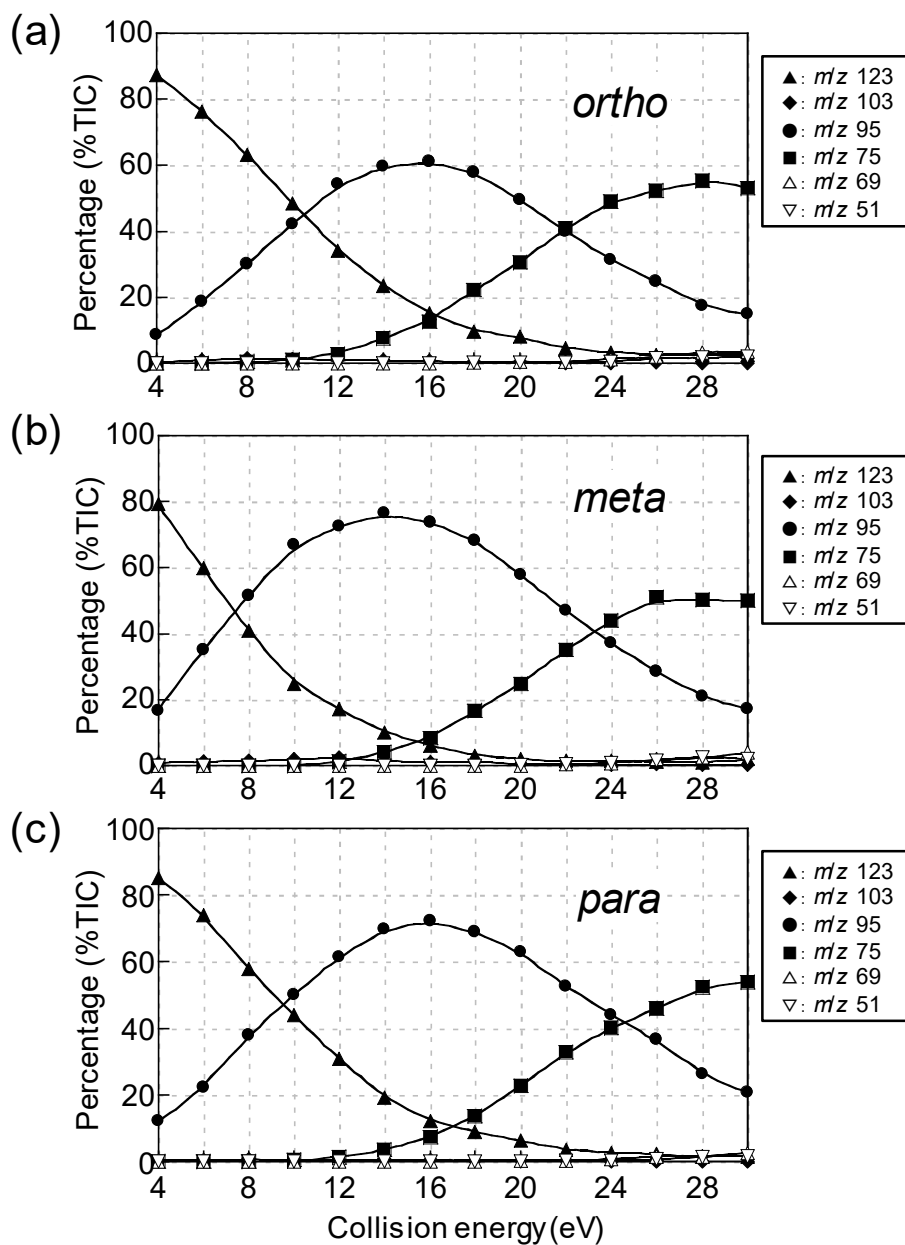


Fig. 5.3 Breakdown curves of the TFA derivatives of (a) *o*-FMC, (b) *m*-FMC, and (c) *p*-FMC in the CE range of 4 to 30 eV. The precursor ion was set at *m/z* 123.

Table 5.1 Standard deviations determined by the intraday variability of the abundances (%TIC) of the ions at m/z 95 and 123 of the TFA derivatives of the FMC positional isomers ($n = 6$).

CE (eV)	<i>Ortho</i>		<i>Meta</i>		<i>Para</i>	
	m/z 95	m/z 123	m/z 95	m/z 123	m/z 95	m/z 123
4	0.8	1.4	1.3	1.6	1.1	1.6
6	2.0	2.5	1.7	1.8	1.4	1.6
8	1.0	1.0	2.1	2.3	3.0	2.5
10	3.6	4.4	2.4	2.7	1.1	0.8
12	1.4	1.2	2.7	2.6	1.8	1.1
14	2.4	1.4	2.9	2.2	1.7	1.5
16	1.3	1.3	3.6	2.5	1.4	1.1

Table 5.2 Standard deviations determined by the interday variability of the abundances (%TIC) of the ions at m/z 95 and 123 of the TFA derivatives of the FMC positional isomers ($n = 6$).

CE (eV)	<i>Ortho</i>		<i>Meta</i>		<i>Para</i>	
	m/z 95	m/z 123	m/z 95	m/z 123	m/z 95	m/z 123
4	0.7	0.8	1.3	0.8	0.8	0.9
6	0.9	1.0	1.5	2.0	1.4	1.4
8	1.2	1.1	2.2	2.3	2.3	2.5
10	1.3	1.5	1.9	1.7	1.2	0.9
12	2.2	2.8	1.3	1.0	0.9	1.1
14	2.1	1.5	2.0	0.9	1.5	0.5
16	1.6	0.8	0.9	0.5	1.3	0.6

To further clarify the differences, the natural logarithmic values of the abundance ratio of the product ion to the precursor ion were plotted against the CE. The plots of the abundance ratio of the m/z 95 ion to the m/z 123 ion [$\ln(A_{95}/A_{123})$] in the CE range of 4 to 16 eV revealed the relationship of *ortho* < *para* < *meta* at any CE (Fig. 5.4), suggesting that the three fluorobenzoyl cations required different energies for the elimination of CO. To confirm that the $\ln(A_{95}/A_{123})$ values were significantly different among the three isomers, the homogeneity of variance test, ANOVA, and multiple pairwise comparisons were conducted (Table 5.3). Bartlett's test for homogeneity of variance showed that the $\ln(A_{95}/A_{123})$ values at CEs of 4 to 8 eV were normally distributed (parametric) and the values at 10 to 16 eV were nonparametric. The results of one-way ANOVA and the Kruskal-Wallis test showed significant differences in the $\ln(A_{95}/A_{123})$ values among the three isomers at each CE ($\alpha < 1.5 \times 10^{-3}$). Subsequent pairwise comparisons, such as the Tukey's test for parametric data and the Steel-Dwass test for nonparametric data, yielded low p values ($p < 1.8 \times 10^{-2}$) at each CE, except for the *ortho* \times *para* comparison at 10 eV. Although simply comparing the logarithmic values at a certain CE would enable the differentiation of the three isomers, such comprehensive comparisons at various CE values should be conducted for unambiguous and reliable differentiation, especially considering the case where the statistical calculation did not show significant difference (e.g., the abovementioned *ortho* \times *para* at 10 eV). Similar results were obtained from the analysis of the free base set of the FMC positional isomers (Figs. 5.5, 5.6, and Tables 5.4-5.6).

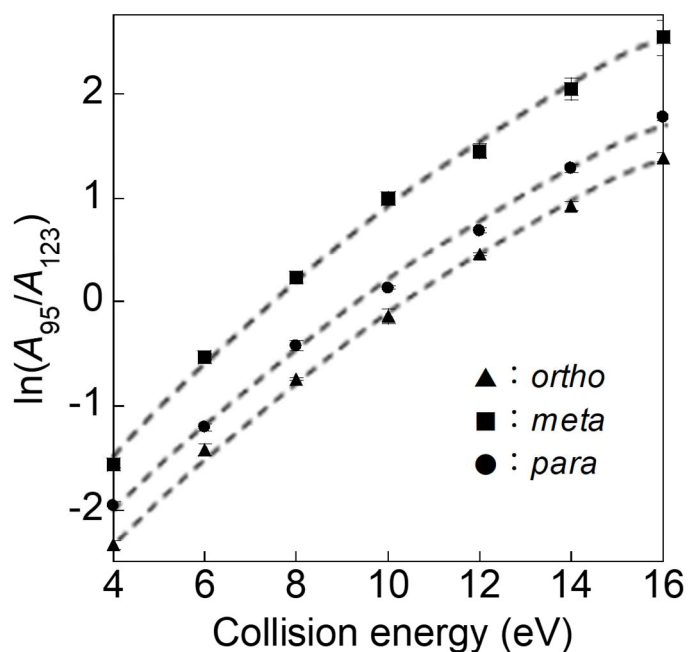


Fig. 5.4 Logarithmic plots of the abundance ratio of the m/z 95 ion to the m/z 123 ion [$\ln(A_{95}/A_{123})$] for the TFA derivatives of the FMC positional isomers in the CE range of 4 to 16 eV. The precursor ion was set at m/z 123. Error bars represent standard errors ($n = 6$).

Table 5.3 Analysis of variance (ANOVA) and multiple pairwise comparisons of the logarithmic values of the abundance ratio of the product ion at m/z 95 to the precursor ion at m/z 123 [$\ln(A_{95}/A_{123})$] of the TFA derivatives of the FMC positional isomers.

CE (eV)	ANOVA ^a (α)	Multiple pairwise comparisons ^b (p)		
		<i>ortho</i> × <i>meta</i>	<i>ortho</i> × <i>para</i>	<i>meta</i> × <i>para</i>
4	4.0×10^{-9}	1.2×10^{-6}	2.3×10^{-5}	1.7×10^{-5}
6	4.2×10^{-10}	1.2×10^{-6}	5.9×10^{-3}	1.3×10^{-6}
8	2.9×10^{-11}	1.2×10^{-6}	5.4×10^{-5}	1.3×10^{-6}
10	1.5×10^{-3}	1.1×10^{-2}	1.3×10^{-1}	1.1×10^{-2}
12	5.1×10^{-4}	1.1×10^{-2}	1.1×10^{-2}	1.1×10^{-2}
14	5.1×10^{-4}	1.1×10^{-2}	1.1×10^{-2}	1.1×10^{-2}
16	6.3×10^{-4}	1.1×10^{-2}	1.1×10^{-2}	1.8×10^{-2}

^a one-way ANOVA (4–8 eV), Kruskal-Wallis test (10–16 eV)

^b Tukey's test (4–8 eV), Steel-Dwass test (10–16 eV)

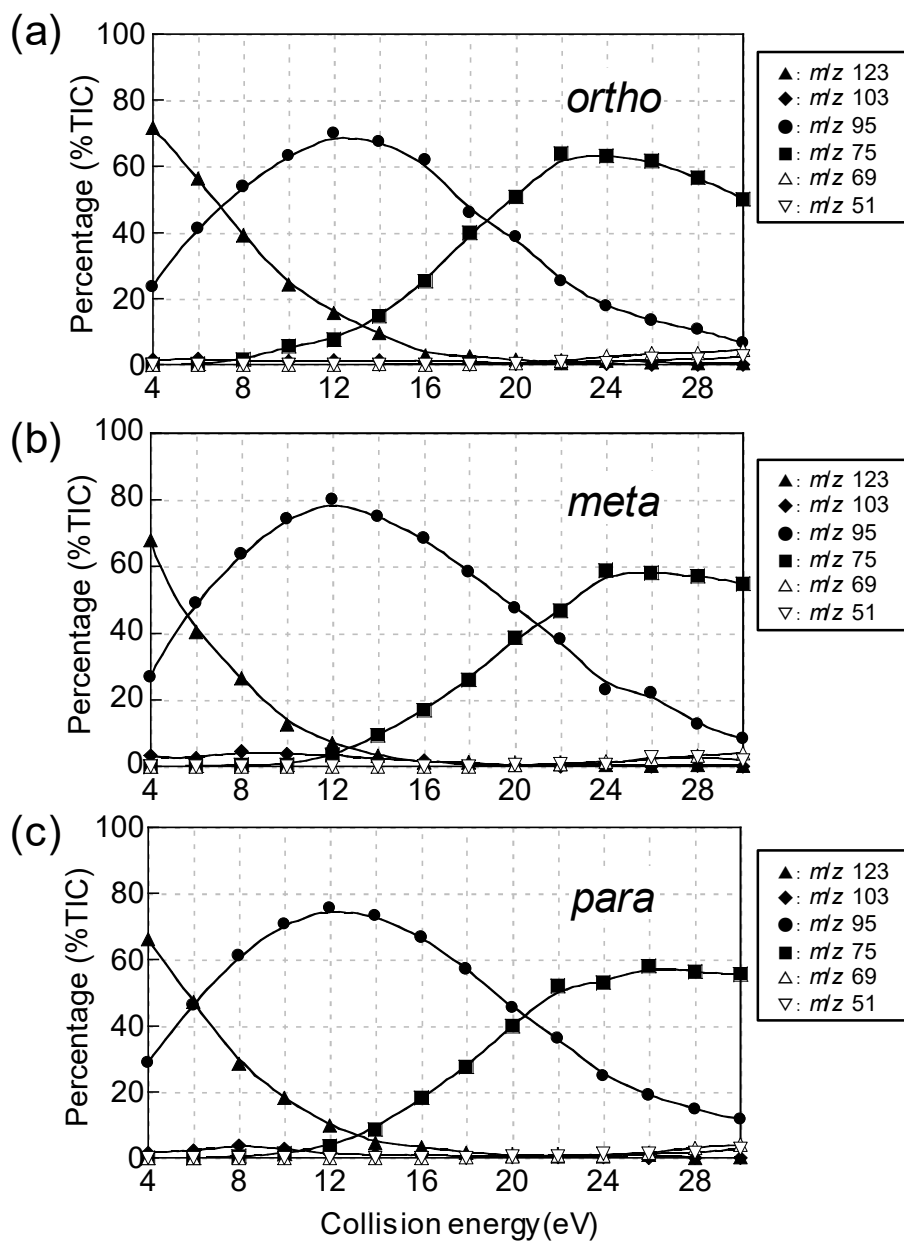


Fig. 5.5 Breakdown curves of the free bases of (a) *o*-FMC, (b) *m*-FMC, and (c) *p*-FMC in the CE range of 4 to 30 eV. The precursor ion was set at m/z 123.

Table 5.4 Standard deviations determined by the intraday variability of the abundances (%TIC) of the ions at m/z 95 and 123 of the free bases of the FMC positional isomers ($n = 6$).

CE (eV)	<i>Ortho</i>		<i>Meta</i>		<i>Para</i>	
	m/z 95	m/z 123	m/z 95	m/z 123	m/z 95	m/z 123
4	1.2	3.3	2.0	1.3	3.2	2.0
6	2.0	2.8	1.8	2.2	1.1	1.7
8	4.4	3.4	2.7	3.6	1.5	1.9
10	1.5	1.7	2.6	1.2	1.2	1.2
12	3.9	1.7	2.5	1.3	1.8	0.9
14	1.1	0.6	3.9	0.4	1.1	0.8
16	3.3	0.6	3.4	0.5	1.7	0.6

Table 5.5 Standard deviations determined by the interday variability of the abundances (%TIC) of the ions at m/z 95 and 123 of the free bases of the FMC positional isomers ($n = 6$).

CE (eV)	<i>Ortho</i>		<i>Meta</i>		<i>Para</i>	
	m/z 95	m/z 123	m/z 95	m/z 123	m/z 95	m/z 123
4	2.7	3.7	2.5	2.2	2.1	1.3
6	3.0	2.1	2.6	3.0	1.2	1.9
8	3.8	2.9	1.7	0.9	2.2	0.5
10	4.9	2.2	2.6	1.2	2.4	1.5
12	2.5	1.9	1.1	1.5	1.9	1.3
14	1.1	2.0	2.9	1.1	1.5	1.0
16	1.7	1.6	1.8	0.5	2.3	1.2

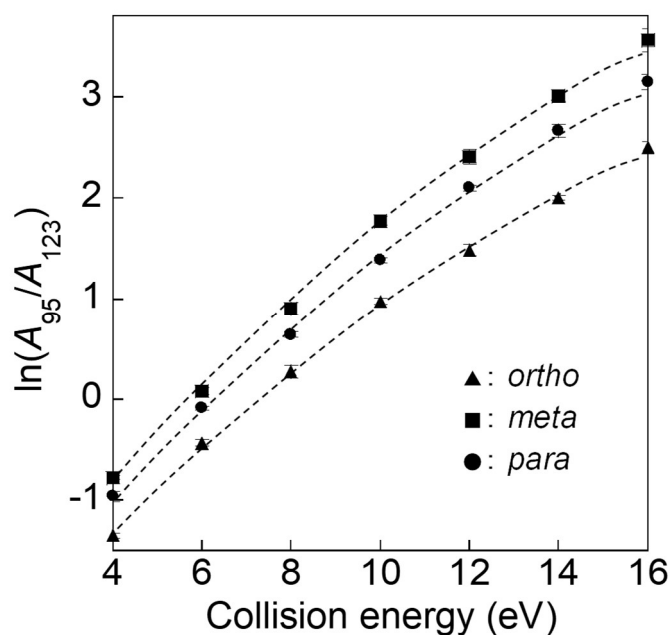


Fig. 5.6 Logarithmic plots of the abundance ratio of the m/z 95 ion to the m/z 123 ion [$\ln(A_{95}/A_{123})$] for the free bases of the FMC positional isomers in the CE range of 4 to 16 eV. The precursor ion was set at m/z 123. Error bars represent standard errors ($n = 6$).

Table 5.6 Analysis of variance (ANOVA) and multiple pairwise comparisons of the logarithmic values of the abundance ratio of the product ion at m/z 95 to the precursor ion at m/z 123 [$\ln(A_{95}/A_{123})$] of the free bases of the FMC positional isomers.

CE (eV)	ANOVA ^a (α)	Multiple pairwise comparisons ^b (p)		
		<i>ortho</i> \times <i>meta</i>	<i>ortho</i> \times <i>para</i>	<i>meta</i> \times <i>para</i>
4	4.2×10^{-7}	1.6×10^{-6}	3.9×10^{-5}	2.2×10^{-2}
6	4.2×10^{-8}	1.3×10^{-6}	6.6×10^{-6}	6.1×10^{-3}
8	1.5×10^{-5}	1.1×10^{-5}	2.2×10^{-3}	2.6×10^{-2}
10	1.9×10^{-9}	1.2×10^{-6}	8.5×10^{-6}	1.4×10^{-5}
12	9.4×10^{-8}	1.3×10^{-6}	1.3×10^{-5}	8.7×10^{-3}
14	4.2×10^{-9}	1.3×10^{-6}	2.1×10^{-6}	1.1×10^{-3}
16	5.1×10^{-4}	1.1×10^{-2}	1.1×10^{-2}	1.1×10^{-2}

^a one-way ANOVA (4–14 eV), Kruskal-Wallis test (16 eV)

^b Tukey's test (4–14 eV), Steel-Dwass test (16 eV)

5.3.3 Theoretical calculations of dissociation energy

The free energies of the molecules involved in the CID reaction were calculated at the B3LYP/6-31G(d,p) level. The CID reaction was presumed to induce minimal conformational changes and have no large reverse activation energies. The optimized structures, the geometries, and the calculated free energies are shown in Fig. 5.7, Tables 5.7, and 5.8, respectively. Predicted free energy diagrams of the CID reaction of the precursor *ortho*-, *meta*-, and *para*-fluorobenzoyl cations (m/z 123) are shown in Fig. 5.8. The calculated dissociation energies for the CO elimination reaction were in the order *meta* (69.4 kcal/mol) < *para* (75.5 kcal/mol) < *ortho* (82.5 kcal/mol). The differences in the dissociation energy might be derived from halogen electron-donating resonance effects: The fluorine substituent in the *ortho* and *para* positions could stabilize the positive charge on the phenyl ring, while the *meta* halogen substituent could not provide such stabilization. Further, the *ortho*- m/z 123 could have extra stabilization via electron delocalization due to the intermolecular interaction between fluorine and the carbonyl group. The described relationship among the three isomers indicates that the CID reactivity increased in the following order: *ortho* < *para* < *meta*, confirming the relationship obtained by ERMS analyses.

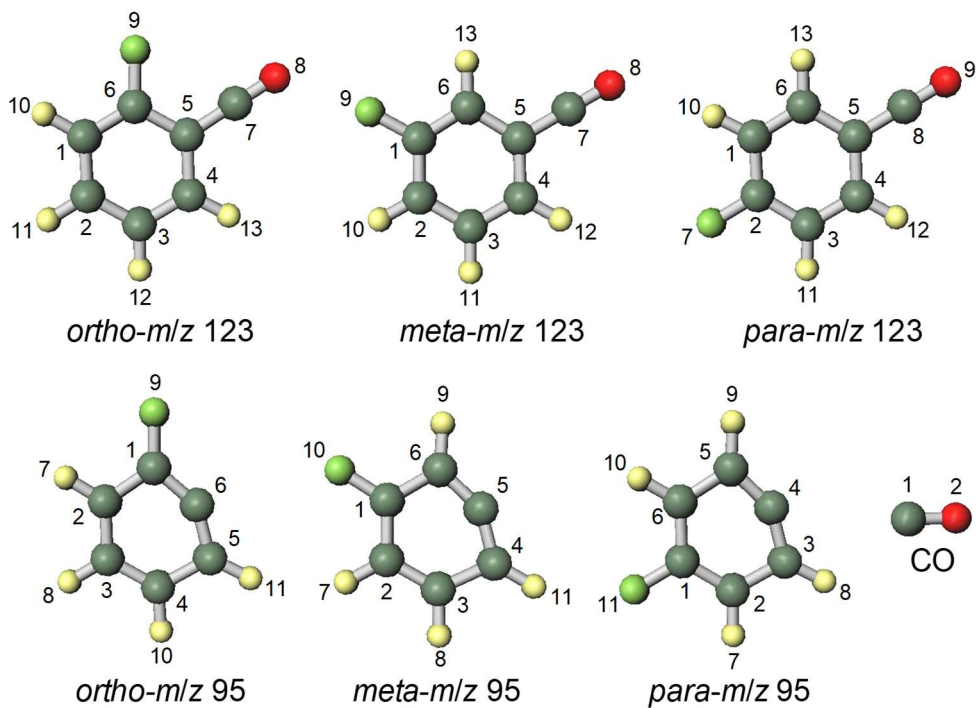


Fig. 5.7 Optimized structures of the *ortho*-, *meta*-, and *para*- m/z 123 and 95 ions and CO at the B3LYP/6-31G(d,p) level.

Table 5.7 Geometries of the *ortho*-, *meta*-, and *para*-*m/z* 123 and 95 ions and CO at B3LYP/6-31G(d,p) level.

ortho-m/z 123

Center number	Atom	Coordinates [Angstroms]		
		x	y	z
1	C	0.08808	-1.84622	0.00000
2	C	1.48266	-1.74689	0.00000
3	C	2.14733	-0.50443	0.00000
4	C	1.42615	0.67081	0.00000
5	C	0.00000	0.58462	0.00000
6	C	-0.65247	-0.68113	0.00000
7	C	-0.77880	1.72328	0.00000
8	O	-1.41176	2.66783	0.00000
9	F	-1.97501	-0.69439	0.00000
10	H	-0.42196	-2.80302	0.00000
11	H	2.06948	-2.66024	0.00000
12	H	3.23077	-0.46967	0.00000
13	H	1.91312	1.63955	0.00000

meta-m/z 123

Center number	Atom	Coordinates [Angstroms]		
		x	y	z
1	C	-0.44648	-1.46132	0.00000
2	C	0.93213	-1.71449	0.00000
3	C	1.84747	-0.65652	0.00000
4	C	1.40417	0.65789	0.00000
5	C	0.00000	0.88194	0.00000
6	C	-0.95142	-0.17360	0.00000
7	C	-0.48549	2.19003	0.00000
8	O	-0.82697	3.26517	0.00000
9	F	-1.28991	-2.48312	0.00000
10	H	1.27025	-2.74602	0.00000
11	H	2.91163	-0.86454	0.00000
12	H	2.09938	1.48966	0.00000
13	H	-2.02069	0.00398	0.00000

para-m/z 123

Center number	Atom	Coordinates [Angstroms]		
		x	y	z
1	C	1.23609	-1.06693	0.00000
2	C	-0.00006	-1.73337	0.00000
3	C	-1.23619	-1.06687	0.00000
4	C	-1.24795	0.31046	0.00000
5	C	0.00000	1.00327	0.00000
6	C	1.24795	0.31040	0.00000
7	F	-0.00010	-3.04819	0.00000
8	C	0.00004	2.38228	0.00000
9	O	0.00023	3.52102	0.00000
10	H	2.15435	-1.64324	0.00000
11	H	-2.15447	-1.64313	0.00000
12	H	-2.18394	0.85831	0.00000
13	H	2.18394	0.85820	0.00000

ortho-m/z 95

Center number	Atom	Coordinates [Angstroms]		
		x	y	z
1	C	-1.04568	-0.10235	0.00000
2	C	-0.34786	1.13292	0.00000
3	C	1.04426	1.20507	0.00000
4	C	1.83032	0.05458	0.00000
5	C	1.23324	-1.25169	0.00000
6	C	-0.07500	-1.04808	0.00000
7	H	-0.99649	2.01072	0.00000
8	H	1.52277	2.17830	0.00000
9	F	-2.34209	-0.22541	0.00000
10	H	2.91715	0.07415	0.00000
11	H	1.79971	-2.17712	0.00000

meta-m/z 95

Center number	Atom	Coordinates [Angstroms]		
		x	y	z
1	C	0.92993	-0.05048	0.00000
2	C	0.08750	-1.16817	0.00000
3	C	-1.28824	-0.98657	0.00000
4	C	-1.96010	0.29259	0.00000
5	C	-0.93319	1.12322	0.00000
6	C	0.39023	1.27275	0.00000
7	H	0.51785	-2.16268	0.00000
8	H	-1.96823	-1.83701	0.00000
9	H	0.99669	2.17255	0.00000
10	F	2.23672	-0.16647	0.00000
11	H	-3.03360	0.42539	0.00000

para-m/z 95

Center number	Atom	Coordinates [Angstroms]		
		x	y	z
1	C	-0.85291	0.00000	0.00000
2	C	-0.18083	1.22782	0.00000
3	C	1.24397	1.27611	0.00000
4	C	1.61865	0.00000	0.00000
5	C	1.24397	-1.27611	0.00000
6	C	-0.18083	-1.22782	0.00000
7	H	-0.72130	2.17083	0.00000
8	H	1.83035	2.18759	0.00000
9	H	1.83035	-2.18759	0.00000
10	H	-0.72130	-2.17083	0.00000
11	F	-2.17447	0.00000	0.00000

CO

Center number	Atom	Coordinates [Angstroms]		
		x	y	z
1	C	-0.65025	0.00000	0.00000
2	O	0.48769	0.00000	0.00000

Table 5.8 Calculated free energies (kcal/mol) of the *ortho*-, *meta*-, and *para*-*m/z* 123 and 95 ions and CO.

Compound	<i>Ortho</i>	<i>Meta</i>	<i>Para</i>
<i>m/z</i> 123	-278509.24	-278507.72	-278512.13
<i>m/z</i> 95	-207327.05	-207338.67	-207336.96
CO		-71099.66	

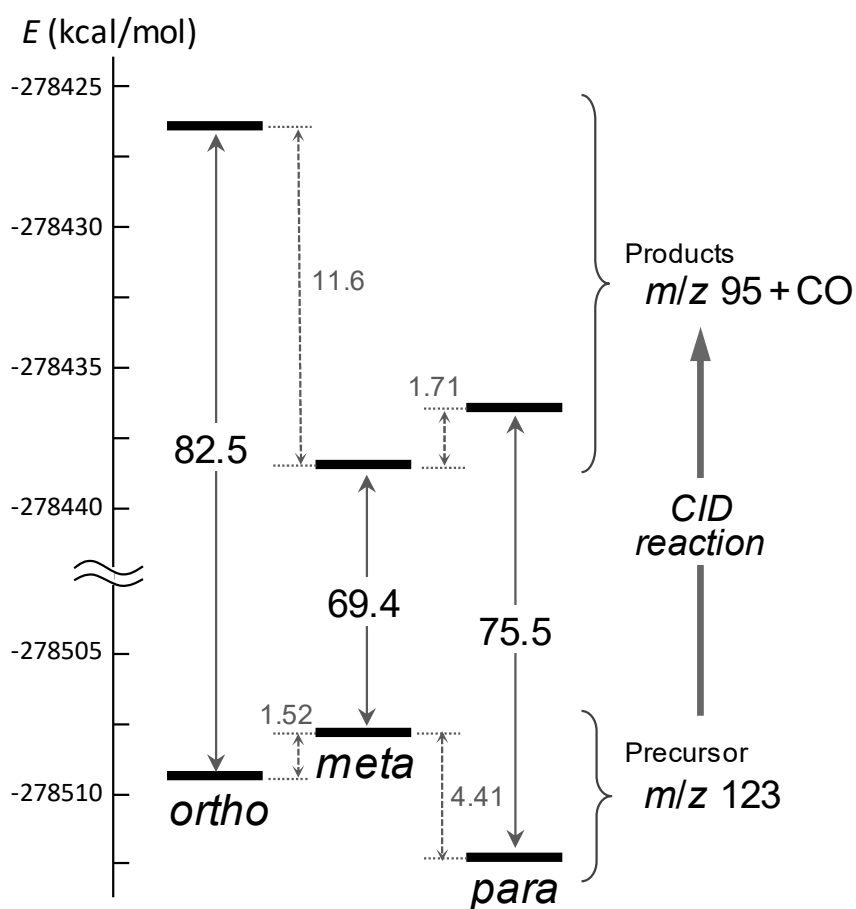


Fig. 5.8 Predicted free energy diagrams of the CID reactions for the precursor ions at *ortho*-, *meta*-, and *para*-*m/z* 123.

5.3.4 Comparisons with methcathinone positional isomers

MMC is a methcathinone containing a methyl group on the aromatic ring. For comparison with the results of FMCs, the present method was also applied to the *o*-, *m*-, and *p*-MMCs. The breakdown curves of the TFA derivatives for the precursor ion at *m/z* 119 (methylbenzoyl cation) with the CE setting varying from 4 to 30 eV in increments of 2 eV (Fig. 5.9). The

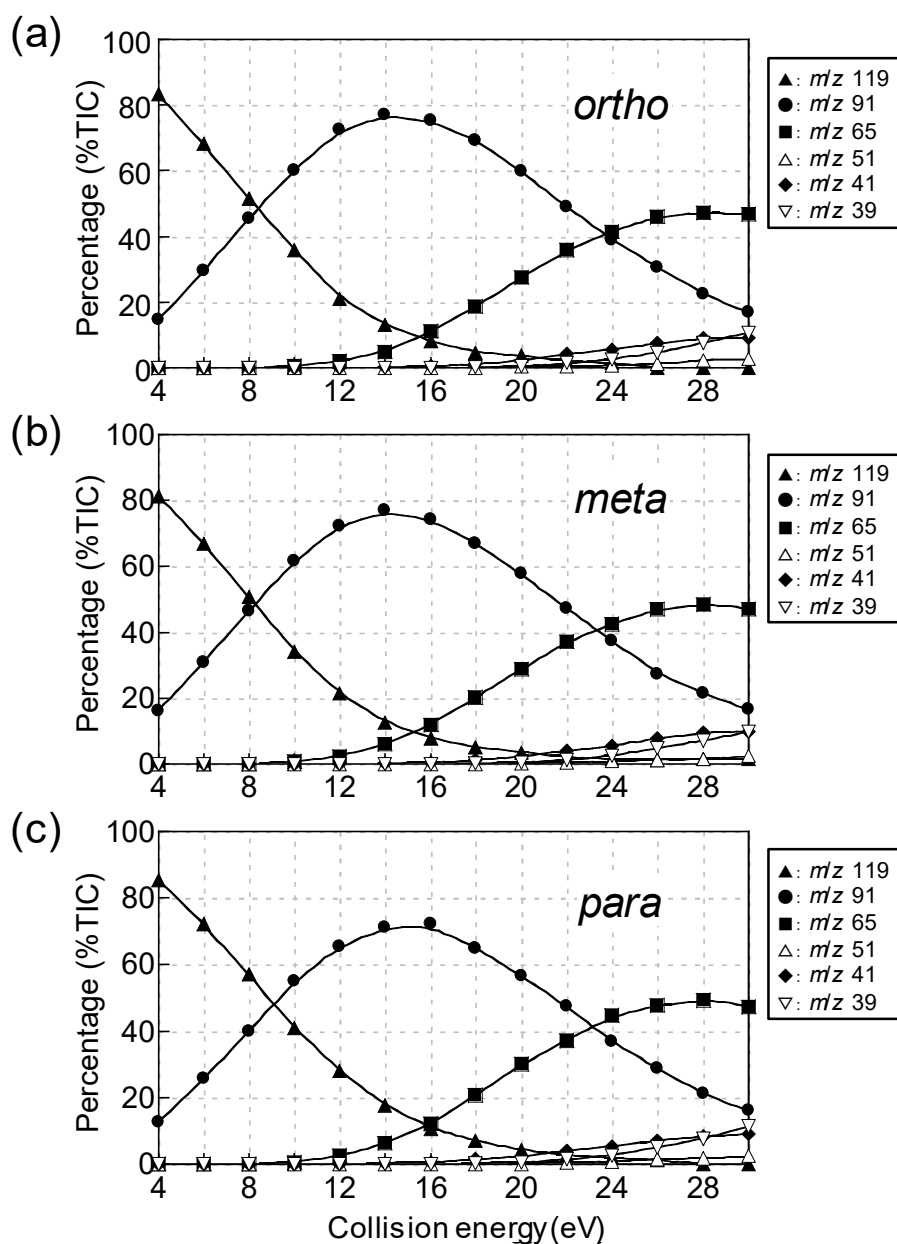


Fig. 5.9 Breakdown curves of the TFA derivatives of (a) *o*-MMC, (b) *m*-MMC, and (c) *p*-MMC in the CE range of 4 to 30 eV. The precursor ion was set at *m/z* 119.

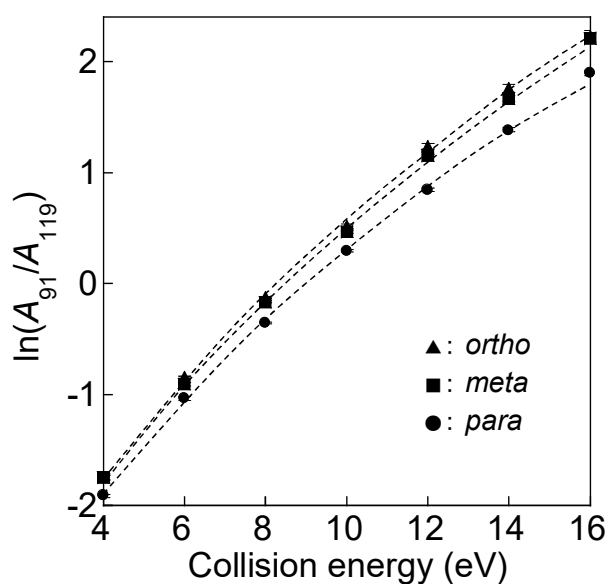


Fig. 5.10 Logarithmic plots of the abundance ratio of the m/z 91 ion to the m/z 119 ion [$\ln(A_{91}/A_{119})$] for the TFA derivatives of the MMC positional isomers in the CE range of 4 to 16 eV. Error bars represent standard errors ($n = 6$).

obtained product ions were identical, and the relative abundance behaviors among the three isomers were very similar. Although the logarithmic values of the abundance ratio of the m/z 91 ion (methylphenyl cation) to the m/z 119 ion [$\ln(A_{91}/A_{119})$] were in the order $para < meta \leq ortho$ (Fig. 5.10), the differences in the values among the three MMC isomers, especially between the *ortho* and *meta* isomers, were not as obvious as those obtained for the FMC isomers. This is because the MMC positional isomers have similar dissociation energies: The predicted CO dissociation energies from the m/z 119 ions were 65.9 kcal/mol for *ortho*, 66.1 kcal/mol for *meta*, and 70.7 kcal/mol for *para* (Figs. 5.11 and 5.12, and Tables 5.9 and 5.10). We initially speculated that the calculated dissociation energies for the MMC positional isomers could follow an order inverse to that followed for the FMC positional isomers ($meta < para < ortho$, as described in Subsection 5.3.3), because the methyl substituent has a positive inductive effect, while the fluorine has a negative inductive effect. However, it appeared that this effect did not have a significant impact on the dissociation energies. Thus,

it is plausible that the resonance effect, rather than the inductive effect, is the dominant factor in determining the dissociation energies. Therefore, it is concluded that the differences in dissociation energies among the FMC positional isomers arose from the halogen-induced resonance effect.

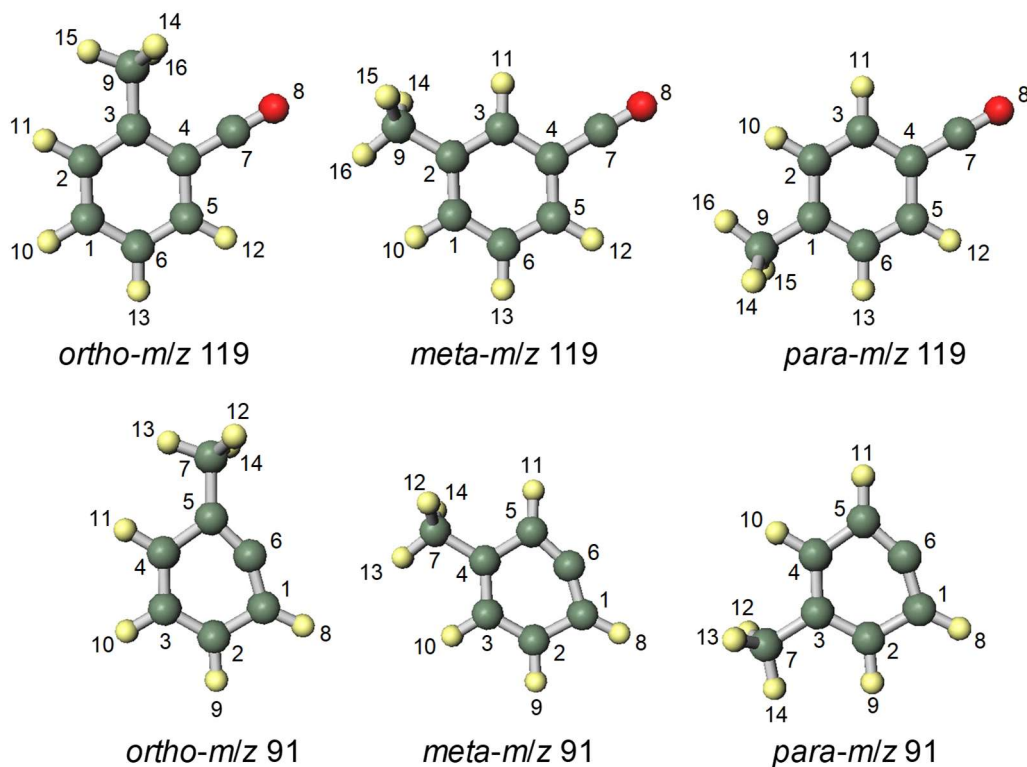


Fig. 5.11 Optimized structures of the *ortho*-, *meta*-, and *para*-*m/z* 119 and 91 ions at the B3LYP/6-31G(d,p) level.

Table 5.9 Geometries of the *ortho*-, *meta*-, and *para*-*m/z* 119 and 91 ions at the B3LYP/6-31G(d,p) level.

<i>ortho-m/z</i> 119					<i>meta-m/z</i> 119					<i>para-m/z</i> 119				
Center number	Atom	Coordinates [Angstroms]			Center number	Atom	Coordinates [Angstroms]			Center number	Atom	Coordinates [Angstroms]		
		x	y	z			x	y	z			x	y	z
1	C	2.31356	0.03786	-0.00014	1	C	-1.65731	0.96181	-0.00018	1	C	1.72830	0.00810	0.00017
2	C	1.43744	1.12922	-0.00041	2	C	-1.45568	-0.43362	-0.00024	2	C	1.01026	1.22424	0.00013
3	C	0.05714	0.95535	-0.00023	3	C	-0.14402	-0.89831	-0.00019	3	C	-0.36914	1.24479	0.00002
4	C	-0.39540	-0.40686	0.00007	4	C	0.92381	0.04164	0.00009	4	C	-1.06187	-0.00011	0.00001
5	C	0.48843	-1.52820	0.00029	5	C	0.70887	1.44861	0.00016	5	C	-0.36150	-1.24296	0.00002
6	C	1.84652	-1.28673	0.00022	6	C	-0.60228	1.88594	0.00004	6	C	1.01548	-1.21442	0.00014
7	C	-1.75064	-0.66260	-0.00005	7	C	2.22240	-0.43137	0.00005	7	C	-2.43938	-0.00292	-0.00001
8	O	-2.86883	-0.88098	-0.00033	8	O	3.29190	-0.82097	-0.00004	8	O	-3.57901	-0.00529	-0.00012
9	C	-0.90415	2.11063	0.00039	9	C	-2.61501	-1.39799	0.00016	9	C	3.22558	-0.00070	-0.00013
10	H	3.38350	0.22250	-0.00033	10	H	-2.67660	1.33720	-0.00043	10	H	1.55293	2.16361	0.00022
11	H	1.83749	2.13773	-0.00078	11	H	0.06831	-1.96270	-0.00041	11	H	-0.91664	2.18096	0.00001
12	H	0.09268	-2.53806	0.00039	12	H	1.54336	2.14061	0.00023	12	H	-0.90472	-2.18157	0.00001
13	H	2.54447	-2.11625	0.00031	13	H	-0.81409	2.94950	0.00000	13	H	1.56395	-2.15101	0.00023
14	H	-1.55532	2.09168	-0.88138	14	H	-2.59090	-2.03699	0.88848	14	H	3.60294	-0.53162	-0.88208
15	H	-0.36575	3.05900	-0.00711	15	H	-2.58046	-2.05104	-0.87743	15	H	3.60375	-0.54066	0.87586
16	H	-1.54378	2.09926	0.89075	16	H	-3.56949	-0.86908	-0.00953	16	H	3.64350	1.00662	0.00462

<i>ortho-m/z</i> 91					<i>meta-m/z</i> 91					<i>para-m/z</i> 91				
Center number	Atom	Coordinates [Angstroms]			Center number	Atom	Coordinates [Angstroms]			Center number	Atom	Coordinates [Angstroms]		
		x	y	z			x	y	z			x	y	z
1	C	-1.26640	-1.26389	-0.00012	1	C	2.01350	-0.27946	0.00002	1	C	1.32481	1.26671	0.00010
2	C	-1.91256	0.00776	0.00026	2	C	1.36949	1.00215	0.00007	2	C	-0.10918	1.20927	-0.00020
3	C	-1.14991	1.17740	-0.00001	3	C	-0.01609	1.14717	-0.00010	3	C	-0.82741	0.00615	-0.00020
4	C	0.24033	1.12557	-0.00022	4	C	-0.88519	0.04716	-0.00018	4	C	-0.11842	-1.20645	-0.00009
5	C	1.01522	-0.10078	0.00000	5	C	-0.32429	-1.28710	-0.00007	5	C	1.31031	-1.27542	-0.00007
6	C	0.03932	-0.99831	-0.00010	6	C	0.98899	-1.12233	0.00006	6	C	1.69617	-0.00490	0.00023
7	C	2.51721	-0.17650	0.00014	7	C	-2.38907	0.16474	0.00009	7	C	-2.33734	0.00560	0.00013
8	H	-1.77846	-2.21852	-0.00030	8	H	3.08372	-0.43821	0.00006	8	H	1.90135	2.18308	0.00001
9	H	-2.99886	0.00808	0.00039	9	H	2.03940	1.85918	0.00016	9	H	-0.60652	2.17638	-0.00036
10	H	-1.64284	2.14323	0.00004	10	H	-0.43591	2.14683	-0.00018	10	H	-0.62700	-2.16816	-0.00008
11	H	0.85240	2.02606	-0.00021	11	H	-0.91720	-2.19343	-0.00009	11	H	1.88169	-2.19506	-0.00002
12	H	2.86734	-0.70999	0.88774	12	H	-2.81861	-0.31621	-0.88385	12	H	-2.72305	-0.50560	0.88723
13	H	2.93367	0.83065	0.00184	13	H	-2.67789	1.21779	-0.00343	13	H	-2.72375	-0.51708	-0.87989
14	H	2.86756	-0.70704	-0.88916	14	H	-2.81750	-0.30992	0.88801	14	H	-2.73641	1.02067	-0.00625

Table 5.10 Calculated free energies (kcal/mol) of the *ortho*-, *meta*-, and *para*-*m/z* 119 and 91 ions and CO.

Compound	<i>ortho</i>	<i>meta</i>	<i>para</i>
<i>m/z</i> 119	-240900.66	-240899.31	-240901.87
<i>m/z</i> 91	-169735.12	-169733.58	-169731.48
CO		-71099.66	

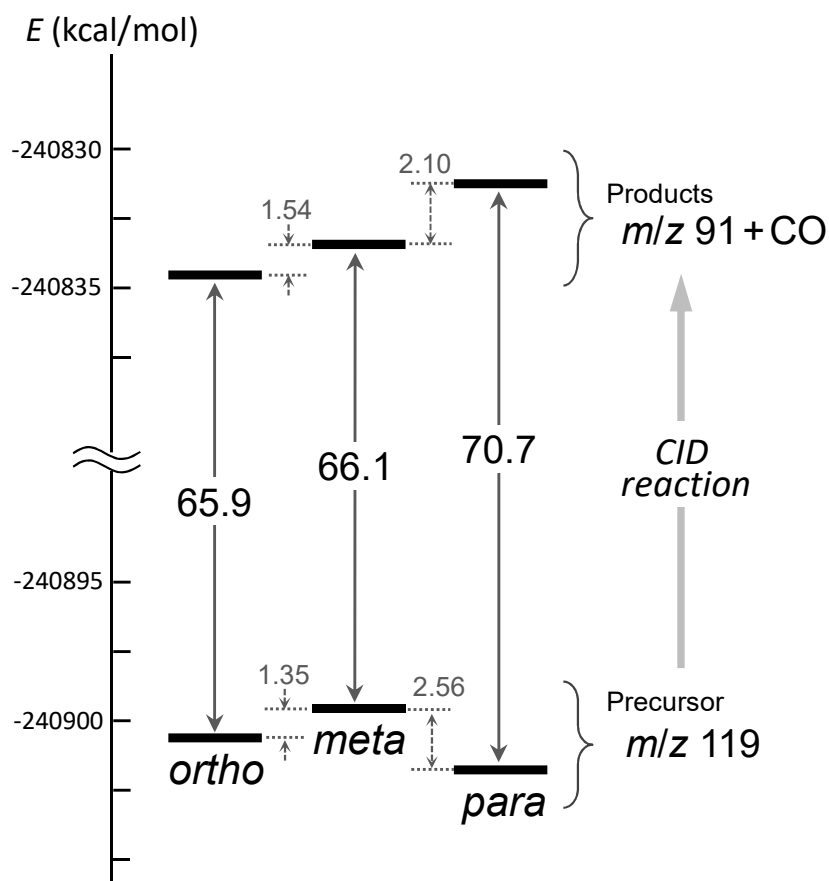


Fig. 5.12 Predicted free energy diagrams of the CID reactions for the precursor ions at *ortho*-, *meta*-, and *para*-*m/z* 119.

5.3.5 Application of the present method to forensic samples

To demonstrate the effectiveness of the differentiation method, three seized real forensic samples were tested. The three forensic samples, which were in the form of dark brown (samples **1** and **2**) and white (sample **3**) powder in 1.5-mL polypropylene microtubes, were seized from suspects of drug possession. In preliminary GC/MS analysis, the following compounds other than FMC were detected in the forensic samples: 2-(1-pyrrolidinyl)-1-(2-naphthalenyl)-1-pentanone (naphyrone), 5,6-methylenedioxy-2-aminoindane (MDAI), and 2-(1-pyrrolidinyl)-1-(3,4-methylenedioxyphenyl)-1-butanone (MDPBP) in sample **1**; 2-(methylamino)-1-(4-methoxyphenyl)-1-propanone (methedrone), 2-(methylamino)-1-phenyl-1-butanone (buphedrone), 2-(methylamino)-1-phenyl-1-pentanone (pentedrone), MDAI, and MDPBP in sample **2**; 2-(methylamino)-1-(3,4-methylenedioxyphenyl)-1-propanone (methylone) and 1,3,7-trimethylpurine-2,6-dione (caffeine) in sample **3**. The ERMS for the TFA derivatives of the samples **1–3** and the set of standard *o*-, *m*-, and *p*-FMC positional isomers were conducted under the same instrumental conditions. The $\ln(A_{95}/A_{123})$ plots of the three samples corresponded well to that of the standard *p*-FMC at each CE (Fig. 5.13); thus, the position of fluorine substitution in FMC was elucidated to be *para* in the samples **1**, **2**, and **3**. This method was not affected even if forensic samples were subjected to the analysis, because chromatographic baseline separations were achieved among the FMCs and other compounds present in the samples. These results indicated that the fluorine substitution position on the phenyl ring of FMC in forensic samples could be identified easily and distinctively by collating the $\ln(A_{95}/A_{123})$ plots of the standard FMC positional isomers.

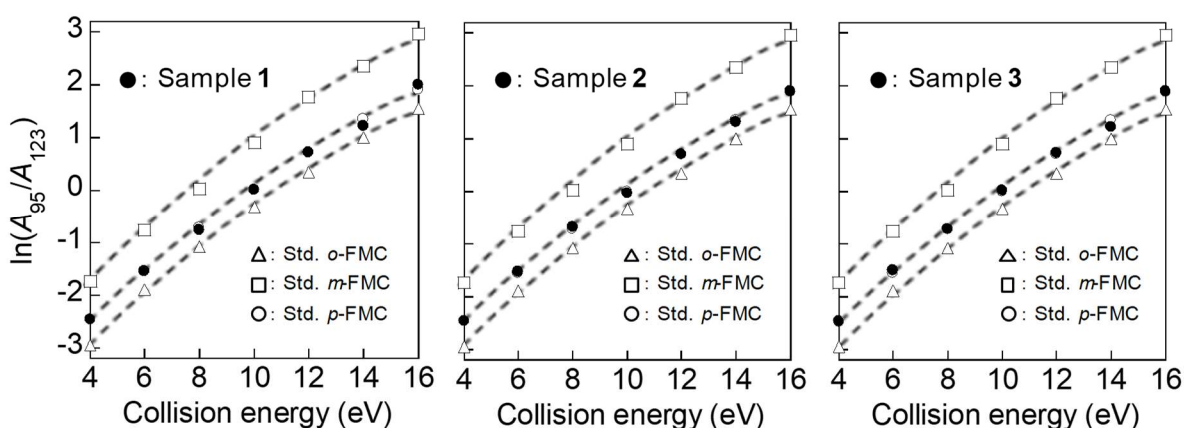


Fig. 5.13 Collations of the $\ln(A_{95}/A_{123})$ plots of the TFA derivatives of the forensic samples 1, 2, and 3 with those of a set of the standard *o*-, *m*-, and *p*-FMC positional isomers.

5.4 Summary

ERMS using EI-QqQ-MS exhibited successful differentiation between *o*-, *m*-, and *p*-FMCs based on the product ion abundances of the fluorophenyl and fluorobenzoyl cations (m/z 95 and 123). The logarithmic plots of the abundance ratios of the two cations [$\ln(A_{95}/A_{123})$] were in the order *ortho* < *para* < *meta* at each CE. The isomeric differences could be attributed to the difference in the dissociation energy during CID due to the halogen substitution resonance effect. The ERMS differentiation method can be applicable to all ring-fluorinated synthetic cathinones because the fluorophenyl and fluorobenzoyl ions are common fragment ions in their full scan and product ion spectra [94,96]. Furthermore, including the results obtained for the synthetic cannabinoids in Chapters 1–4 [81,86,97], it was determined that the ERMS method developed herein can be applied to differentiate almost all ring-fluorinated positional isomers in major classes of NPSs.

Chapter 6

Differentiation of 2-, 3-, and 4-fluoro- α -pyrrolidinopropiophenones by Triton B-mediated one-pot reaction

6.1 Introduction

Ortho-, *meta*-, and *para*-ring-fluorinated positional isomers of synthetic cathinones exhibit similar chromatographic properties and nearly identical mass spectra, rendering their differentiation difficult [94]. Several research groups have attempted to discriminate between these isomers by using different column types, column-temperature programs, and ion sources [39,95,96]. However, these reported methods require specialized analytical conditions and only show subtle differences among the positional isomers. Therefore, a more convenient and definite differentiation method is required. To address this issue, as discussed in Chapters 2–5, we developed a positional isomer differentiation method for *o*-, *m*-, and *p*-fluorinated isomers of synthetic cathinones (in addition to synthetic cannabinoids) using ERMS [81,86,97,102]. This study was performed to develop other reliable positional isomer differentiation methods based on different concepts of the ERMS method.

Meshram et al. reported that aryl halides can be converted to aryl alkyl ethers via a one-pot nucleophilic aromatic substitution (S_NAr) reaction with aliphatic alcohols catalyzed by benzyltrimethylammonium hydroxide (Triton B) [103]. It was expected that this reaction could be applied for the differentiation of the ring-fluorinated synthetic cathinones based on the hypothesis described in Subsection 6.3.2. The three positional isomers of synthetic cathinone, 2-, 3-, and 4-fluoro- α -pyrrolidinopropiophenones (*o*-, *m*-, and *p*-FPPPs), were reacted with methanol (MeOH) in the presence of Triton B and the applicability of this protocol for positional isomer differentiation was evaluated based on the chromatographic and mass spectral analyses of the corresponding reaction products.

6.2 Materials and methods

6.2.1 Reagents

Standard reagents of *o*-, *m*-, and *p*-FPPPs were synthesized as described below. Triton B (as 40 wt% solution in MeOH), pyrrolidine, and 4-fluoropropiophenone were obtained from Tokyo Chemical Industry Co., Ltd. (Tokyo, Japan). All the solvents used were of high-purity grade.

6.2.2 Syntheses

2-Bromo-1-(2-, 3-, and 4-fluorophenyl)-1-propanones

N-Bromosuccinimide (7.9 mmol) and *p*-toluenesulfonic acid monohydrate (1.3 mmol) were added to a solution of 4-fluoropropiophenone (6.6 mmol) in anhydrous acetonitrile (12 mL) at room temperature. The reaction mixture was heated to 60°C, stirred for 4 h, diluted with ethyl acetate, and successively washed with distilled water, saturated NaHCO₃ solution, and brine, followed by drying over anhydrous Na₂SO₄. The obtained solution was evaporated under reduced pressure to afford crude 2-bromo-1-(4-fluorophenyl)-1-propanone (6.1 mmol, 92% yield) that was subsequently purified by silica gel column chromatography using isocratic elution with ethyl acetate/hexane (1:9, *v/v*). 2-Bromo-1-(2- and 3-fluorophenyl)-1-propanones were synthesized by the same procedure in yields of 91 and 83%, respectively.

2-, 3-, and 4-fluoro- α -pyrrolidinopropiophenones (o-, m-, and p-FPPPs)

A solution of 2-bromo-1-(4-fluorophenyl)-1-propanone (4.4 mmol) in anhydrous acetonitrile (20 mL) was slowly added to pyrrolidine (13.1 mmol) and K₂CO₃ (10.1 mmol) in anhydrous acetonitrile (20 mL) at 0°C, and the reaction mixture was stirred for 16 h at the same temperature. Volatile materials were removed under reduced pressure, and the residue was redissolved in ethyl acetate. The organic layer was successively washed with distilled

water and brine, dried over anhydrous Na₂SO₄, and concentrated under reduced pressure to give the crude product, which was purified by basic silica gel column chromatography using isocratic elution with ethyl acetate/hexane (2:98, v/v) to afford *p*-FPPP (4.3 mmol, 98% yield) as a slightly yellow viscous liquid. *o*- and *m*-FPPPs were synthesized by the same procedure in yields of 75 and 94%, respectively.

6.2.3 Synthetic procedures for optimization of Triton B-mediated reaction condition

A representative experimental procedure is described for entry 2 of Table 6.1. Entries 1 and 3–7 follow the same procedure except for the Triton B amounts, solvents, reaction temperature, and reaction time. A screw cap vial was charged with *p*-FPPP (0.22 mmol) and 40 wt% Triton B solution in MeOH (0.26 mL, i.e. Triton B, 0.66 mmol; MeOH, 5.3 mmol) at room temperature (25°C), and the resulting mixture was stirred for 24 h. Reaction progress was monitored by basic thin layer chromatography using ethyl acetate/hexane (5:95, v/v) as the mobile phase. After the reaction was completed, MeOH was removed under reduced pressure, and the residue was redissolved in ethyl acetate. The organic layer was successively washed with distilled water and saturated brine, dried over anhydrous Na₂SO₄, and concentrated under reduced pressure to give the crude product, which was subsequently purified by basic silica gel column chromatography using isocratic elution with ethyl acetate/hexane (5:95, v/v) to afford 4-methoxy- α -pyrrolidinopropiophenone (*p*-MeOPPP, 0.10 mmol, 46% yield) as a yellow viscous liquid.

6.2.4 Extraction procedure for instrumental analysis of reaction products

A screw cap vial was charged with *o*-, *m*-, or *p*-FPPP (0.11 mmol) and 40 wt% Triton B solution in MeOH (0.13 mL, i.e. Triton B, 0.33 mmol; MeOH, 2.7 mmol) at room temperature (25°C), and the reaction mixture was stirred and sampled (aliquot volume, 20 μ L)

after 0, 3, 15, and 24 h. The withdrawn samples were diluted with aqueous Na₂CO₃ solution (pH 10) and extracted with ethyl acetate. The organic extract was evaporated under reduced pressure, and the residue was reconstituted with MeOH (500 μL) and filtered through an Ultrafree®-MC GV centrifugal filter unit with Durapore® PVDF 0.22-μm membrane (Millipore, Bedford, MA, USA). The filtrate was diluted 20-, 400-, and 4000-fold with MeOH and analyzed by GC/EI-QqQ-MS, LC/ESI-LIT-MS, and LC/ESI-TOF-MS, respectively.

6.2.5 Instrumental analysis of reaction products

GC/EI-QqQ-MS was performed on a SCION TQ (Bruker Daltonics, Billerica, MA, US), equipped with a non-polar fused-silica capillary BR-5ms column (30 m × 0.25 mm i.d., 0.25-μm film thickness; Bruker Daltonics). GC parameters were as follows: injection volume, 1 μL; inlet temperature, 200°C; injection mode, split (10:1); carrier gas, high-purity helium (six nine-grade); flow rate, 45.1 cm/s (constant); column-temperature program, initial temperature at 80°C held for 1 min, ramped up to 280°C at 10°C/min; and transfer line temperature, 280°C. The MS parameters were as follows: ionization mode, EI (70 eV); ion-source temperature, 230°C; acquisition mode, full scan and product ion scan (precursor ion, *m/z* 123); and collision gas, argon (1.5 mTorr).

LC/ESI-LIT-MS was performed on a Prominence ultrafast liquid chromatograph (Shimadzu, Kyoto, Japan), linked to an LXQ mass spectrometer (Thermo Fisher Scientific, Waltham, MA, US) equipped with an ESI source. The analytes were separated using an L-column2 ODS column (150 × 1.5 mm i.d., 5-μm particle size; Chemicals Evaluation and Research Institute, Tokyo, Japan) at a column oven temperature of 40°C. The LC parameters were as follows: injection volume, 1 μL; flow rate, 0.1 mL/min; and elution mode, gradient using 10 mM ammonium acetate solution in MeOH/distilled water (5:95, *v/v*) (A) and 10 mM ammonium acetate solution in MeOH/distilled water (95:5, *v/v*) (B) (elution solvent

composition was varied from 100% A to 100% B over 15 min, followed by isocratic elution with 100% B for 10 min). The MS parameters were as follows: ionization mode, ESI; polarity, positive; acquisition mode, full scan and product ion scan; activation type, CID; collision gas, helium; normalized CE, 35.0%; and activation time, 30 ms.

LC/ESI-TOF-MS was performed on an UltiMate 3000 high performance liquid chromatograph (Thermo Fisher Scientific), linked to a micrOTOF II mass spectrometer (Bruker Daltonics) equipped with an ESI source. A Unison UK-Phenyl column (150 × 1.5 mm i.d., 5- μ m particle size; Imtakt, Kyoto, Japan) and a column oven temperature of 40°C were used. The LC parameters were as follows: injection volume, 1 μ L; flow rate, 0.4 mL/min; and elution mode, gradient using 10 mM ammonium acetate solution in distilled water (A) and MeOH (B) (the elution solvent composition was varied from 95% A to 95% B over 30 min, followed by isocratic elution with 95% B for 10 min). The MS parameters were as follows: ionization mode, ESI; polarity, positive; and acquisition mode, full scan.

6.3 Results and discussion

6.3.1 Chromatographic and mass spectral properties of *o*-, *m*-, and *p*-FPPPs

It is difficult to distinguish positional isomers of ring-fluorinated synthetic cathinones by chromatographic and mass spectral techniques. Herein, the results of analyzing *o*-, *m*-, and *p*-FPPPs using GC/EI-QqQ-MS and LC/ESI-LIT-MS are shown in Figs. 6.1 and 6.2. The GC peaks of *m*- and *p*-FPPPs were slightly separated using the non-polar 5ms column, but baseline separation was difficult (Fig. 6.1a). The corresponding EI-full scan and product ion spectra recorded were very similar to each other (Figs. 6.1b). The peak corresponding to *o*-FPPP could not be detected at all; instead, the broad peak was observed, attributed to a thermal degradation product, 5-methyl-1,2,3,10*b*-tetrahydropyrrolo[2,1-*a*]isoquinolin-6-one, produced by intramolecular cyclization via loss of HF from *o*-FPPP [39] (Figs. 6.1a and 6.1c). This thermal decomposition could not be suppressed by controlling the inlet temperature and the split ratio. In LC/ESI-LIT-MS, the three isomers could not be separated on an ODS column (Fig. 6.2a) and all three multiple-stage mass spectra, viz. ESI-full scan mass spectra

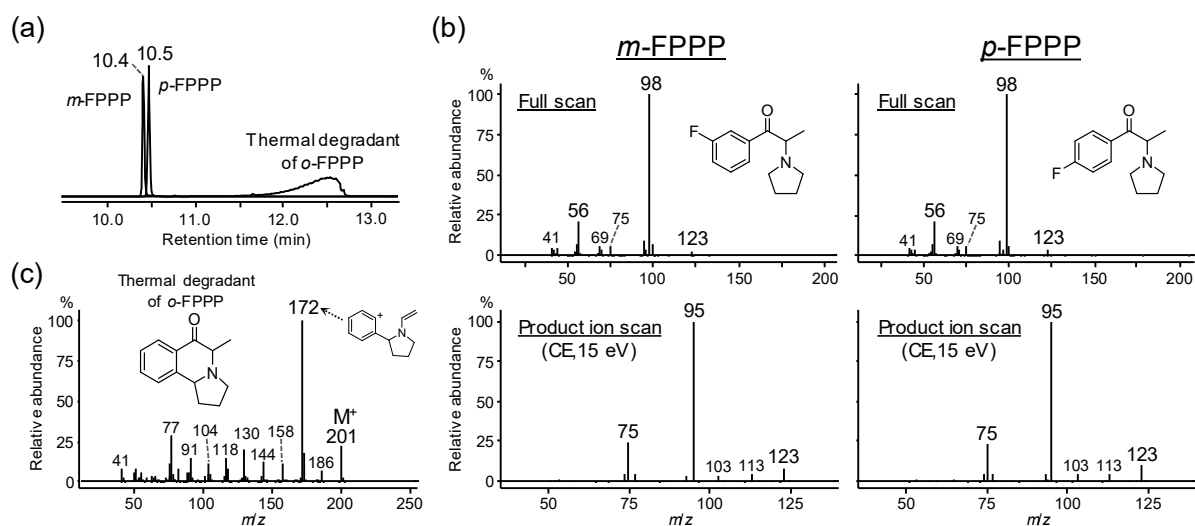


Fig. 6.1 (a) Total ion current chromatograms of *o*-, *m*-, and *p*-FPPPs, (b) full scan and product ion spectra (precursor ion, *m/z* 123; collision energy (CE), 15 eV) of *m*- and *p*-FPPPs, and (c) full scan mass spectrum of the *o*-FPPP thermal degradant, obtained using GC/EI-QqQ-MS.

(MS¹), 1st-generation product ion spectra (MS²; precursor ion, m/z 222), and 2nd-generation product ion spectra (MS³; precursor ion, m/z 205), were remarkably similar (Fig. 6.2b). Thus, GC/EI-QqQ-MS and LC/ESI-LIT-MS were found to be unsuitable for the differentiation of *o*-, *m*-, and *p*-FPPPs.

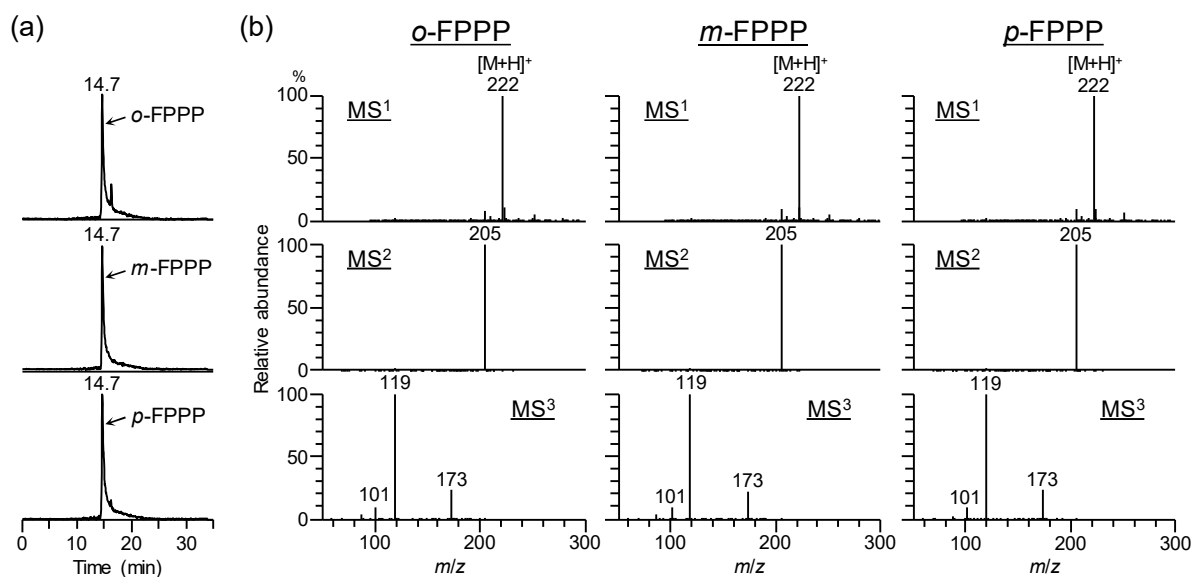
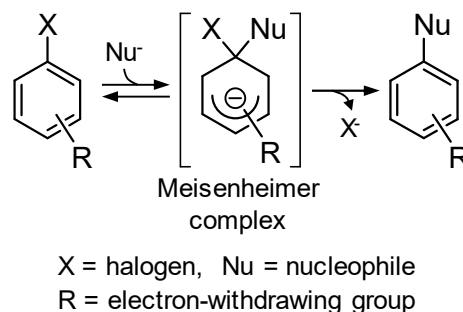


Fig. 6.2 (a) Extracted ion chromatograms ($[M+H]^+$, m/z 222) and (b) full scan mass spectra (MS¹), 1st-generation product ion spectra (MS²; precursor ion, m/z 222), and 2nd-generation product ion spectra (MS³; precursor ion, m/z 205) of *o*-, *m*-, and *p*-FPPPs, obtained using LC/ESI-LIT-MS.

6.3.2 Optimization of Triton B-mediated reaction condition

According to Meshram et al., 4-fluoroacetophenone can be alkoxyated by aliphatic alcohols in the presence of Triton B to afford the corresponding 4-alkoxyacetophenones in high yields (76–86%) [103]. Typically, S_NAr reactions proceed as shown in Scheme 6.1 [104,105]. A nucleophile attacks the



Scheme 6.1 S_NAr reaction.

substrate at the leaving group (e.g. halogen)-bearing carbon to form a σ -adduct (known as a

Meisenheimer complex), with subsequent halogen elimination affording the final product. The resonance-stabilized complex can only be formed when the leaving group is located *ortho* or *para* to the electron-withdrawing group, i.e., only *o*- and *p*-halobenzenes undergo S_NAr reactions. Since FPPPs contain ring-attached fluoride (leaving group) and carbonyl (electron-withdrawing group) groups, *o*- and *p*-FPPPs should undergo S_NAr reactions. If MeOH is used as a nucleophile in this reaction, the FPPPs should be methoxylated to afford 2- and 4-methoxy- α -pyrrolidinopropiophenones (*o*- and *p*-MeOPPPs), respectively, while *m*-FPPP should not react. Importantly, the *o*-, *m*-, and *p*-isomers of ring-methoxylated phenylethylamines, including *o*-, *m*-, and *p*-MeOPPPs, can be easily discriminated by chromatography and product ion spectrometry [56,106,107] (Fig. 6.3). Therefore, we

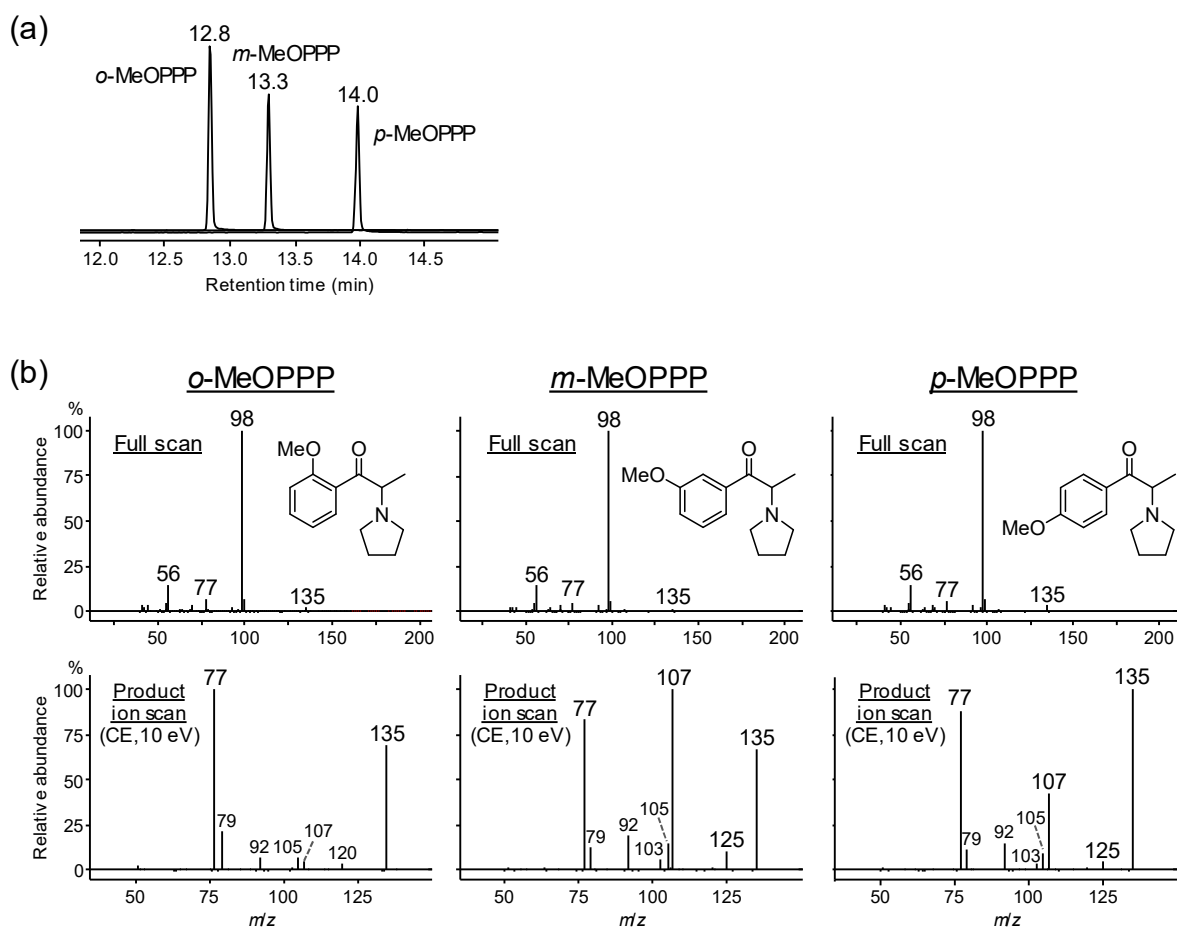
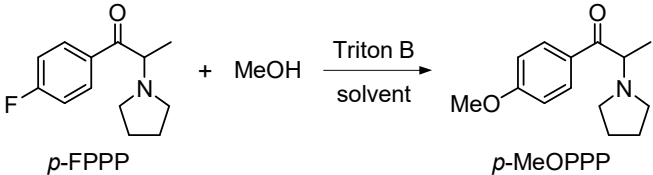


Fig. 6.3 (a) Total ion current chromatograms and (b) full scan and product ion spectra (precursor ion, *m/z* 135; CE, 10 eV) of *o*-, *m*-, and *p*-MeOPPPs, obtained using GC/EI-QqQ-MS.

expected that the Triton B-mediated reaction should be able to unequivocally differentiate among these three isomers by chromatographic and mass spectrometric analyses of their S_NAr reaction products (*o*-MeOPPP, *m*-FPPP, and *p*-MeOPPP).

After confirming that 4-fluoropropiophenone can be converted to 4-methoxypropylphenone in 91% yield by Triton B-mediated S_NAr reactions, we started optimization of the reaction conditions. The initial reaction was carried out by treating *p*-FPPP with MeOH (7.8 equiv.) in the presence of Triton B (1.0 equiv.) at room temperature for 24 h, which afforded the expected product (*p*-MeOPPP) in low yield (< 10%; entry 1 in Table 6.1). To make the reaction proceed more efficiently, three-fold higher quantities of Triton B and MeOH were used, and the yield increased to 46% (entry 2). No unreacted *p*-FPPP remained in the reaction mixture (i.e., *p*-FPPP was completely consumed), which indicated that a side reaction occurred alongside the desired methoxylation reaction. Considering that 4-fluoropropiophenone was methoxylated in good yield, it was assumed that the side reaction involved the amine moiety of FPPP and concluded that the reaction yield cannot be further increased by increasing the amount of Triton B. Moreover, no improvements were achieved by altering the temperature (0 and 50°C; entries 3 and 4) and solvent (Et₂O, THF, and neat; entries 5–7). In the solvent changing experiments, Triton B (1.5 equiv., after evaporation of MeOH) and MeOH (1.1 equiv.) were separately added to solutions of *p*-FPPP in Et₂O and THF or to neat *p*-FPPP. Therefore, the optimized condition of Triton B-mediated reaction was found to be those of entry 2.

Table 6.1 Optimization of Triton B-mediated reaction conditions.

Entry	Triton B (equiv.)	Solvent	Temperature (°C)	Reaction time (h)	Isolated yield (%)
1	1.0	MeOH	rt	24	< 10
2	3.0	MeOH	rt	24	46
3	3.0	MeOH	0	15	0
4	3.0	MeOH	50	8	34
5	1.5	Et ₂ O	rt	16	15
6	1.5	THF	rt	12	0
7	1.5	neat	rt	5	0

6.3.3 Application to positional isomer differentiation

In the same manner as described in section 6.3.2 (analyte: *p*-FPPP), both *o*- and *m*-FPPPs were reacted with methanolic solution of Triton B under the optimized conditions (entry 2 in Table 6.1). *m*-FPPP was not methoxylated, as expected, but *o*-FPPP was also not methoxylated. Alternatively, the corresponding characteristic reaction products ($[M+H]^+$, m/z 289) were observed by LC/ESI-LIT-MS. Interestingly, the reaction products of *o*- and *m*-FPPPs showed different retention times (20.4 and 20.9 min, respectively; Fig. 6.4a), and some mass spectral differences between them were observed in MS² and MS³ for the precursor ions at m/z 289 and 220, respectively (Fig. 6.4b). The abundance of the m/z 218 product ion in MS² for the *meta*-product was higher than that observed for the *ortho*-product. The MS³ featured markedly different abundances of product ions, with m/z 135, 192, 200, and 202. Characteristic ions at m/z 109 and 158 were observed for the *ortho*-product. ESI-TOF-MS showed that the exact mass of the $[M+H]^+$ ions equaled 289.1717, and thus, they were identified as C₁₇H₂₂FN₂O (mass error = -0.6 mDa; mSigma value obtained with the

SigmaFit algorithm = 2.4). Figure 6.5 shows the yields of the *ortho*-, *meta*-, and *para*-reaction products ($[M+H]^+$, m/z 289.1717) obtained after different reaction times (0, 3, 15, and 24 h), demonstrating that the reactivity of this reaction depends on the fluorine substitution pattern on the phenyl ring. Specifically, the yield of the *ortho*-product was approximately four-fold larger than that of the *meta*-product, while the *para*-product was hardly observed. Moreover, EI-full scan mass spectra of the *ortho*- and *meta*-products differed in the fragment ion abundances at m/z 70, 96, 123, and 202 (Fig. 6.6). Additionally, the mass spectrum of the *ortho*-product contained a characteristic ion peak at m/z 172, derived from thermally induced intramolecular cyclization and successive CO elimination, same as the ion observed in Fig. 6.1c. According to the instrumental data and previous reports on the fragmentation patterns of synthetic cathinones [38,39,106,108], it can be assumed that the *ortho*- and *meta*-reaction products were FPPP-enamine-pyrrolidine adducts (Fig. 6.6 inset, including possible fragmentation), where pyrrolidine was bonded to the main backbone in the corresponding FPPP oxidized at the 2,3-C-C bond (2,3-enamine). Although the pyrrolidine scaffold was probably produced by FPPP degradation [36], the detailed reaction mechanism remains unclear.

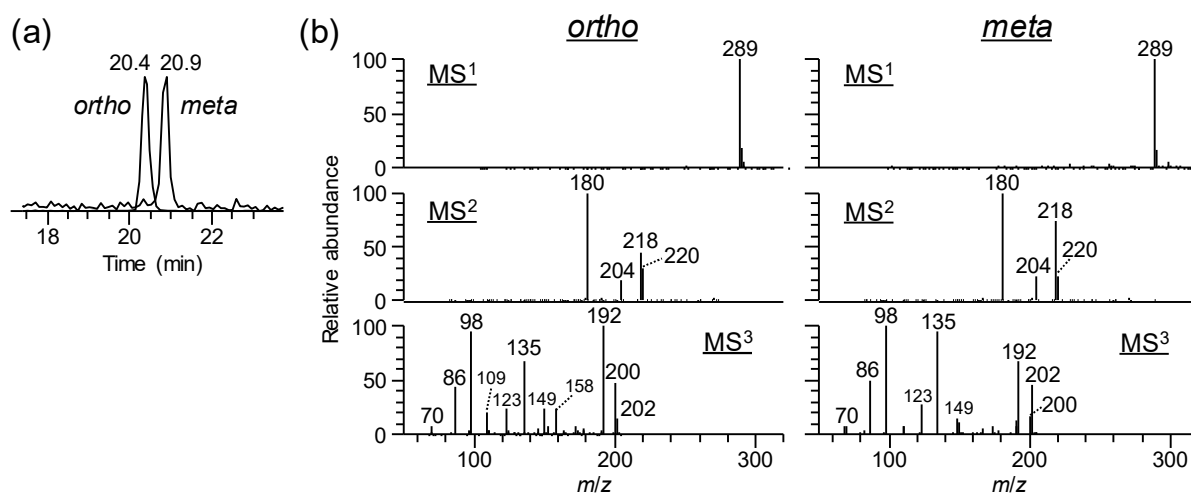


Fig. 6.4 (a) Extracted ion chromatograms ($[M+H]^+$, m/z 289) and (b) MS¹, MS² (precursor ion, m/z 289), and MS³ (precursor ion, m/z 220) mass spectra of the *ortho*- and *meta*-reaction products, obtained using LC/ESI-LIT-MS.

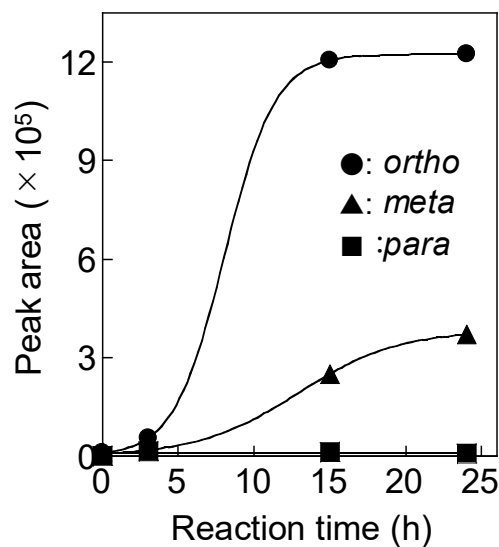


Fig. 6.5 Yields (extracted ion chromatographic peak area) of the *ortho*-, *meta*-, and *para*-reaction products ($[M+H]^+$, m/z 289.1717), determined at reaction times of 0, 3, 15, and 24 h using LC/ESI-TOF-MS

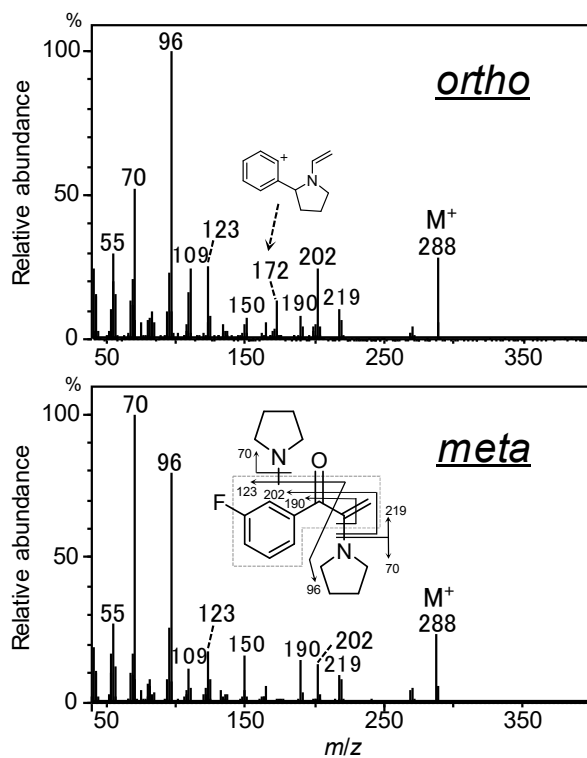


Fig. 6.6 EI-full scan mass spectra of *ortho*- and *meta*-reaction products.

Based on the above results, Triton B-mediated one-pot reaction successfully allowed the differentiation of *o*-, *m*-, and *p*-FPPPs. The differentiation procedure is summarized as follows: When *p*-MeOPPP is afforded in the reaction, the original analyte corresponds to *p*-FPPP. Otherwise, the fluorine substitution pattern (*ortho* or *meta*) of the reaction products, which were presumed to be FPPP-enamine–pyrrolidine adducts, should be distinguished using LC/MS and GC/MS, corresponding to that of the original analyte. Note that since the proposed differentiation method results in structural destruction of the original analyte, the presence of FPPP in forensic samples should be confirmed in advance.

6.4 Summary

Triton-B-mediated one-pot reaction with MeOH can be used to differentiate between *o*-, *m*-, and *p*-FPPPs. In particular, only *p*-FPPP was methoxylated to afford *p*-MeOPPP, whereas *o*- and *m*-FPPPs yielded corresponding characteristic products, possibly FPPP-enamine–pyrrolidine adducts. Chromatographic and mass spectral analyses of the reaction products allowed the positional isomers of FPPP to be definitely assigned.

Chapter 7

Molecularly imprinted polymer solid-phase extraction of synthetic cathinones from urine and whole blood samples

7.1 Introduction

Highly efficient and class-selective methods for extraction of abused drugs from biological specimens are required in both clinical and forensic analyses. However, conventional extraction methods like hydrophilic polymer-based solid-phase extraction (SPE) and liquid-liquid extraction (LLE) are unsuitable for the extraction of synthetic cathinones. In particular, hydrophilic polymer-based SPE, which is often used in forensic toxicological drug extraction, does not exclude the biological matrices sufficiently due to the sorbent affinities for various compounds. LLE runs a risk of target analyte loss during extraction for basified samples, because synthetic cathinones are easily decomposed under alkaline extraction condition [36].

Molecularly imprinted polymers (MIPs) are functional polymers with molecular-level cavities that exhibit selective binding [109]. These polymers are synthesized by copolymerization of functional and cross-linking monomers in the presence of template molecules [110]. Initially, the functional monomers form a complex with the templates via covalent and/or noncovalent interactions, and after polymerization, the monomer–template assemblies are held in position by a highly cross-linked three-dimensional rigid structure. Subsequent removal of the imprinted molecules leaves cavities with size, shape, and chemical functionality complementary to those of the template species used in their synthesis. Upon the introduction of target molecules that are compatible with the MIP cavities, they are trapped due to affinity imparted by the imprinted morphology of the cavities and through electrostatic interactions. Thus, the use of an MIP as an SPE sorbent could enable highly class-selective

extraction with fewer matrices [111–119]. In addition, MIPs are advantageous in that they can bind even polar molecules if the molecule itself fits the MIP cavity. Already, MIPs are commercially available as SPE cartridges for various target molecules (e.g., β -agonists, β -blockers, nonsteroidal anti-inflammatory agents, nitrosamines, and polycyclic aromatic hydrocarbons). An MIP-SPE cartridge, marketed as AFFINILUTE MIP-Amphetamine, has a high affinity for amphetamine, MA, and MDMA, and its usefulness as an extractive pretreatment method has been reported [120–123]. Since synthetic cathinones are structurally very similar to amphetamines, we envisaged that the MIP-SPE cartridge will be applicable for the extraction of synthetic cathinones from biological samples. Thus, we examined the applicability of the MIP-SPE method using the AFFINILUTE cartridge for 11 synthetic cathinones, as shown in Fig. 7.1, present in urine and whole blood samples. The extraction efficiency and class selectivity were evaluated by quantitation using LC/ESI-QqQ-MS, and the results were compared with those obtained using conventional hydrophilic polymer-based

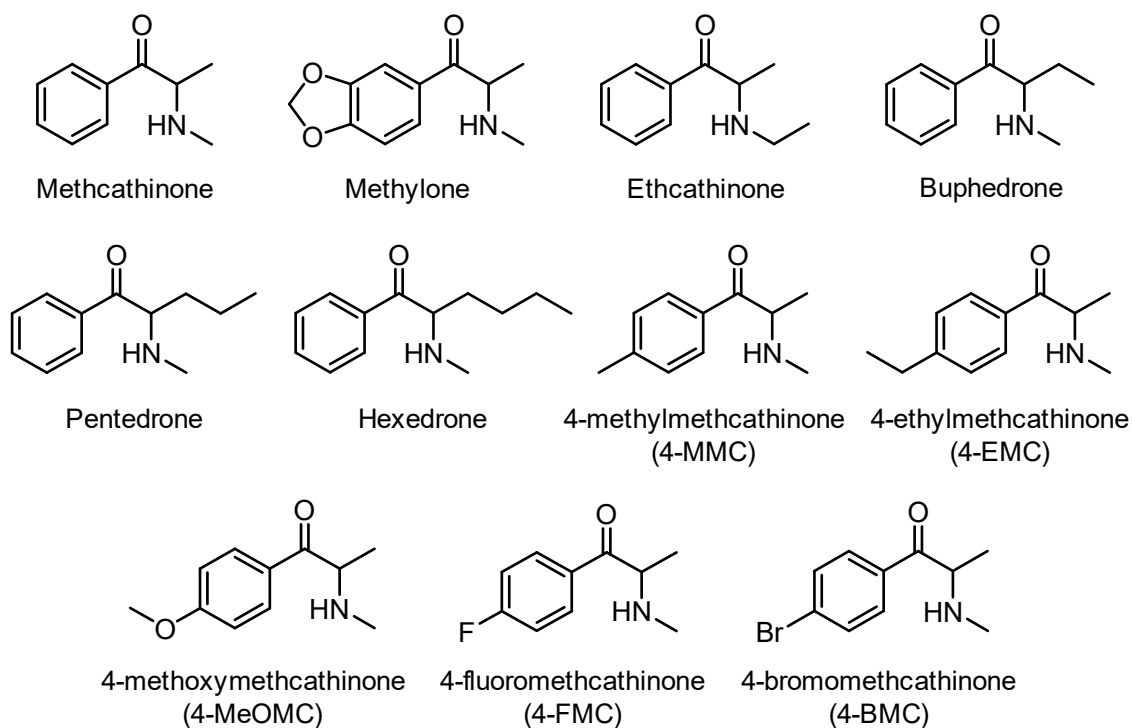


Fig. 7.1 Chemical structures of the 11 synthetic cathinones.

SPE and LLE methods. This study is the first successful application of MIP-SPE to the selective extraction of synthetic cathinones from biological samples.

7.2 Material and methods

7.2.1 Reagents

2-(Methylamino)-1-phenyl-1-propanone (methcathinone) monohydrochloride salt was synthesized as described below. 2-(Methylamino)-1-(1,3-benzodioxol-5-yl)-1-propanone (methylone), 2-(ethylamino)-1-phenyl-1-propanone (ethcathinone), 2-(methylamino)-1-phenyl-1-butanone (buphedrone), 2-(methylamino)-1-phenyl-1-pentanone (pentedrone), 2-(methylamino)-1-phenyl-1-hexanone (hexedrone), 2-(methylamino)-1-(4-methylphenyl)-1-propanone (mephedrone, 4-methylmethcathinone, 4-MMC), 2-(methylamino)-1-(4-ethylphenyl)-1-propanone (4-ethylmethcathinone, 4-EMC), 2-(methylamino)-1-(4-methoxyphenyl)-1-propanone (methedrone, 4-methoxymethcathinone, 4-MeOMC), 2-(methylamino)-1-(4-fluorophenyl)-1-propanone (flephedrone, 4-fluoromethcathinone, 4-FMC), and 2-(methylamino)-1-(4-bromophenyl)-1-propanone (brephedrone, 4-bromomethcathinone, 4-BMC) were purchased as their hydrochloride salts (purity \geq 98%) from Cayman Chemical (Ann Arbor, MI, USA). The internal standard (IS), (S)-(-)-1-phenylethylamine (1-PEA, purity \geq 98%) was purchased from Tokyo Chemical Industry (Tokyo, Japan). Normal urine from pooled human donors was purchased from Lee Biosolutions (Maryland Heights, MO, USA). Horse whole blood (hemolyzed) was purchased from Cosmo Bio (Tokyo, Japan).

7.2.2 Synthesis of methcathinone hydrochloride

Methylamine in methanol was added to a solution of 2-bromopropiophenone in methanol, and the resulting mixture was stirred at room temperature for 1 h, followed by the addition of

distilled water ($10 \times$ volume). The mixture was subsequently acidified with concentrated hydrochloric acid and washed twice with diethyl ether. The aqueous layer was basified with sodium carbonate and extracted three times with diethyl ether. The combined organic extracts were washed three times with brine, dried over anhydrous sodium sulfate, and the solvent was evaporated under reduced pressure. Methanolic hydrochloric acid was added dropwise to the residue, and the solvent was evaporated to yield the crude hydrochloride salt. Methcathinone hydrochloride was obtained by recrystallization (diethyl ether/methanol) as a white crystalline solid (yield: 27%).

7.2.3 Sample preparation

Individual stock standard solutions of the 11 synthetic cathinones and the IS were prepared separately by dissolving an appropriate quantity of each compound in methanol to give a concentration of 200 $\mu\text{g/mL}$, and the resulting solutions were stored at -20°C . Neat working standard mixture solution (each at 1000 ng/mL) was prepared in distilled water by appropriate dilution of the 200- $\mu\text{g/mL}$ individual stock standard solutions. Working standard solutions of concentrations 1, 10, and 100 ng/mL were prepared by serial dilution of the 1000 ng/mL working standard solution. Biological standard mixture sample (each at 1000 ng/mL) was prepared by spiking drug-free human urine or drug-free horse whole blood (18.8 mL) with each 200- $\mu\text{g/mL}$ individual stock standard solution of the 11 synthetic cathinones and the IS (each 100 μL). Biological standard samples of concentrations 1, 10, and 100 ng/mL were prepared in drug-free human urine or drug-free horse whole blood by serial dilution of the 1000 ng/mL biological standard sample.

7.2.4 Molecularly imprinted polymer solid-phase extraction procedures

The analytes were extracted using an AFFINILUTE MIP-Amphetamine SPE cartridge (25 mg/3 mL; Biotage AB, Uppsala, Sweden), which sorbent was designed by MIP Technologies AB (Lund, Sweden, a subsidiary of Biotage). The MIP-SPE process was performed on a Preppy 12-port vacuum manifold (Sigma-Aldrich, St. Louis, MO, USA). An aliquot (200 μ L) of the analyte-spiked neat solution (for Subsections 7.3.1 and 7.3.2) or biological (urine or whole blood) sample (for Subsection 7.3.3) was added to a 10 mM ammonium acetate buffer (2.8 mL, pH 4, 5, 6, 7, 8, 9, and 10 for Subsection 7.3.1, pH 6 for Subsections 7.3.2 and 7.3.3), and the resulting solution was vortex-mixed and centrifuged at $12,000 \times g$ for 5 min at 4°C. The MIP-SPE cartridge was activated with methanol (1 mL) and equilibrated with the same pH-adjusted 10 mM ammonium acetate buffer (1 mL). Subsequently, the supernatant of the prepared sample solution was applied to the cartridge under gravity (0.5 mL/min), and the cartridge was washed twice with distilled water (1 mL \times 2) and with acetonitrile/distilled water (60:40, v/v; 1 mL). After drying the cartridge by aspiration at -30 kPa for 10 min, it was washed with acetic acid/acetonitrile (1:99, v/v; 1 mL) and redried at -10 kPa for 30 s. The analytes were then eluted twice with formic acid/methanol (1:99, v/v; 1 mL \times 2), and the cartridge was aspirated at -30 kPa for 30 s between each elution. The combined eluents were evaporated under reduced pressure, and reconstituted with methanol/distilled water (1:1, v/v; 200 μ L) prior to analysis by LC/ESI-QqQ-MS.

7.2.5 Hydrophilic polymer-based solid-phase extraction procedure

The analytes were extracted using an Oasis HLB cartridge (60 mg/3 mL; Waters, Milford, MA, USA) according to the manufacturer's instructions, which is commonly used for drug-extraction from biological samples in forensic toxicological field. The SPE procedure was carried out using a Preppy 12-port vacuum manifold (Sigma-Aldrich). An aliquot of a

spiked urine sample (200 μL) was diluted with distilled water (1.8 mL), and the sample solution was vortex-mixed and centrifuged at $12,000 \times g$ for 5 min at 4°C . The Oasis HLB cartridge was activated using methanol (1 mL) and equilibrated with distilled water (1 mL). The diluted sample was applied to the cartridge under gravity, and the cartridge was washed with methanol/distilled water (5:95, v/v ; 1 mL). Subsequently, the analytes were eluted using methanol (1 mL). Finally, the eluent was evaporated under reduced pressure, and reconstituted with methanol/distilled water (1:1, v/v ; 200 μL) prior to analysis by LC/ESI-QqQ-MS.

7.2.6 Liquid-liquid extraction procedure

The LLE method employed here was based on the Stas-Otto method for classical drug and poison screening. An aliquot of a spiked urine sample (200 μL) was diluted with distilled water (1.8 mL) and the pH was adjusted to approximately 10 using Na_2CO_3 . The resulting mixture was extracted three times with chloroform/2-propanol (3:1, v/v ; 1 mL \times 3), and the combined organic extracts were dried over anhydrous sodium sulfate, evaporated under reduced pressure, and reconstituted with methanol/distilled water (1:1, v/v ; 200 μL) prior to the analysis by LC/ESI-QqQ-MS.

7.2.7 Instrumentation

LC/ESI-QqQ-MS was performed on an Agilent 1260 Infinity LC system linked to a 6470A triple-quad LC/MS tandem mass spectrometer (Agilent Technologies, Santa Clara, CA, USA) equipped with an Agilent Jet Stream (AJS) ESI source. Instrumental control, data acquisition, and analysis were performed using Mass Hunter software ver. B.07.00 (Agilent Technologies). A Unison UK-Phenyl column (150 mm \times 3 mm id, 3- μm particle size; Imtakt, Kyoto, Japan) was used with a column oven temperature of 40°C . The injection volume was 1

μL and the flow rate was 0.4 mL/min. A gradient elution mode was employed using a 10 mM ammonium acetate solution in distilled water (A) and methanol (B). The solvent gradient involved transition from 95% A to 95% B over 30 min, followed by isocratic elution using the final solvent composition over 10 min. The AJS-ESI conditions were as follows: nebulizing gas temperature, 300°C; nebulizing gas flow, 12 L/min; nebulizer pressure, 55 psi; sheath gas temperature, 300°C; and sheath gas flow, 12 L/min. The MS parameters were as follows: polarity, positive; operating mode, multiple reaction monitoring (MRM); cell accelerator voltage, 4 eV; and collision gas, nitrogen. The MRM transition parameters were optimized as detailed in Table 7.1.

Table 7.1 MRM transition parameters for 11 synthetic cathinones and for 1-PEA (the IS).

Compound	Transition (m/z)	Fragmentor voltage (V)	CE (eV)
Methcathinone	164.1 > 146.1	100	9
Methylone	208.1 > 160.0	90	17
Ethcathinone	178.1 > 160.1	90	13
Buphedrone	178.1 > 160.1	100	9
Pentedrone	192.1 > 174.1	100	9
Hexedrone	206.2 > 188.1	100	13
4-MMC	178.1 > 160.1	100	9
4-EMC	192.1 > 174.1	100	9
4-MeOMC	194.1 > 176.1	100	13
4-FMC	182.1 > 164.1	100	13
4-BMC	242.0 > 145.1	90	17
1-PEA	122.1 > 105.0	60	9

7.2.8 Recovery, matrix effect, and linear regression

Recovery and matrix effect can be determined as follows:

$$\text{Recovery (\%)} = A / B \times 100$$

$$\text{Matrix effect (\%)} = (A - C) / C \times 100$$

where A is the peak area of prespiked analytes (spiked before extraction) in the final extract, B is the peak area of postspiked analytes (spiked after extraction) in the final extract, and C is the peak area of analytes in the methanol/distilled water (1:1, v/v) solution.

The regression equation for each synthetic cathinone extracted from the urine/whole blood sample was obtained by linearly fitting a plot of the ratios of the peak area of the analyte to that of the IS versus the analyte concentration. The limit of detection (LOD) was defined as the lowest concentration of analyte spiked in the urine/whole blood sample that could be detected with a signal-to-noise ratio ≥ 3 .

7.3 Results and discussion

7.3.1 Optimization of the sample solution pH

MIP-SPE was performed using an AFFINILUTE MIP-Amphetamine cartridge, as described in the protocol for amphetamine-extraction recommended by the manufacturer and described in previous reports [121–123]. Theoretical calculations revealed that the acidity constant (K_a) values of the synthetic cathinones were approximately two orders of magnitude lower than those of amphetamines [124–126]. Thus, the pH of the sample solution loaded onto the MIP-SPE cartridge was presumed to have a critical effect on the recovery. To determine the optimal pH for maximizing the interactions between the analyte and the MIP,

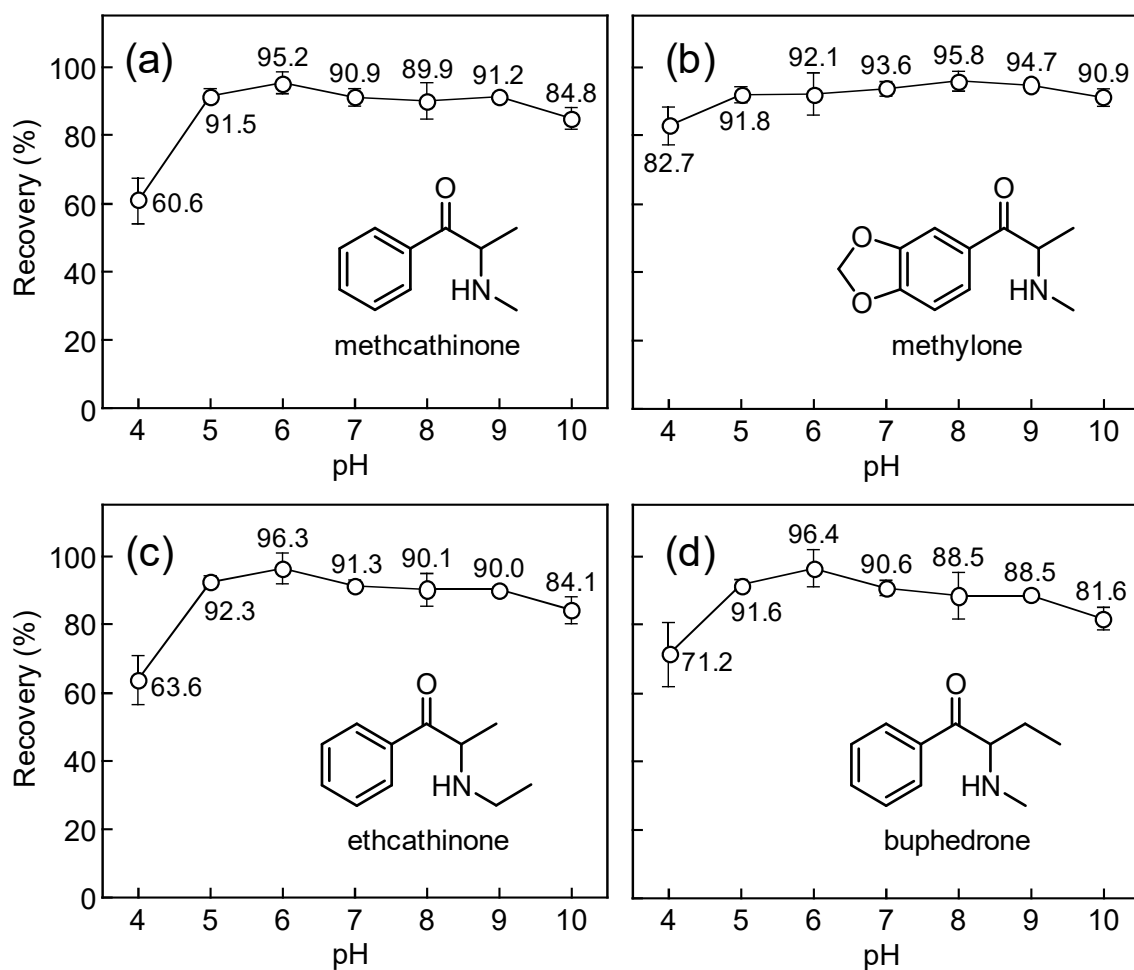


Fig. 7.2 Effect of loading solution pH on the recoveries (mean \pm SD, $n = 3$) of (a) methcathinone, (b) methyldone, (c) ethcathinone, and (d) buphedrone.

the recoveries of four synthetic cathinones (methcathinone, methylone, ethcathinone, and buphedrone; each at 100 ng/mL) were compared in neat solutions at pH ranging from 4 to 10. Figure 7.2 shows that the lowest recoveries were obtained for all the compounds at pH 4 (60.6–82.7%), while the maximum recoveries were obtained at pH 6 (92.1–96.4%). A further increase in pH to 10 had a detrimental effect on the recoveries. At pH 6, synthetic cathinones are positively charged due to protonation of their amine moieties, resulting in effective interactions with the MIP cavities via hydrogen bonding and electrostatic interactions. Hence, a pH of 6, at which the synthetic cathinones are at no risk of decomposition [36], was selected as the optimal pH for initial sample loading. This result is consistent with the fact that the differences between the optimal loading pH of synthetic cathinones and amphetamines corresponded to the differences in their pK_a values, with the optimal pH for amphetamine-extraction using the AFFINILUTE MIP-Amphetamine cartridge being 8 [123].

7.3.2 Influence of synthetic cathinone molecular structure on extraction efficiency

To investigate the influence of the synthetic cathinone molecular structure on the MIP-SPE recovery, nine synthetic cathinones (methcathinone, buphedrone, pentedrone, hexedrone, 4-MMC, 4-EMC, 4-MeOMC, 4-FMC, and 4-BMC) were extracted from the neat solutions (each at 100 ng/mL). The recoveries for methcathinone, buphedrone, pentedrone, and hexedrone, which bear alkyl side chains of different lengths, were 95.2, 96.4, 88.7, and 84.3%, respectively, while those for methcathinone, 4-MMC, 4-EMC, 4-MeOMC, 4-FMC, and 4-BMC, which have different *para* substituents on their aromatic rings, were 95.2, 92.1, 91.8, 92.1, 92.5, 90.5, and 90%, respectively. To prove the dependence of extraction recovery on the analyte structure, the relationship between the recovery and the Taft's steric substituent constant (E_s) [127] of each substituent in the analyte structure was determined. It should be noted that E_s becomes more negative with increasing size of the substituent and was

normalized as $H = 0$. The recovery–structure relationship for methcathinone, buphedrone, pentedrone, and hexedrone ($R_1 = H, Me, Et, \text{ and } nPr$, respectively, $R_2 = H$) (Fig. 7.3a) indicated that the presence of an alkyl side chain longer than $R_1 = Me$ ($E_s = -1.24$) resulted in slightly diminished recovery. By contrast, the recovery–structure relationship obtained for methcathinone, 4-MMC, 4-EMC, 4-MeOMC, 4-FMC, and 4-BMC ($R_1 = H, R_2 = H, Me, Et, OMe, F, \text{ and } Br$, respectively) (Fig. 7.3b) demonstrated that the differences in the steric bulk of the *para* substituents on the phenyl ring ($E_s = -1.31-0$) had no effect on recovery. These results together confirmed that the MIP employed in this study could be applied to the extraction of the prevailing synthetic cathinones with good extraction efficiency, except for *N*-pyrrolidine-type synthetic cathinones [14].

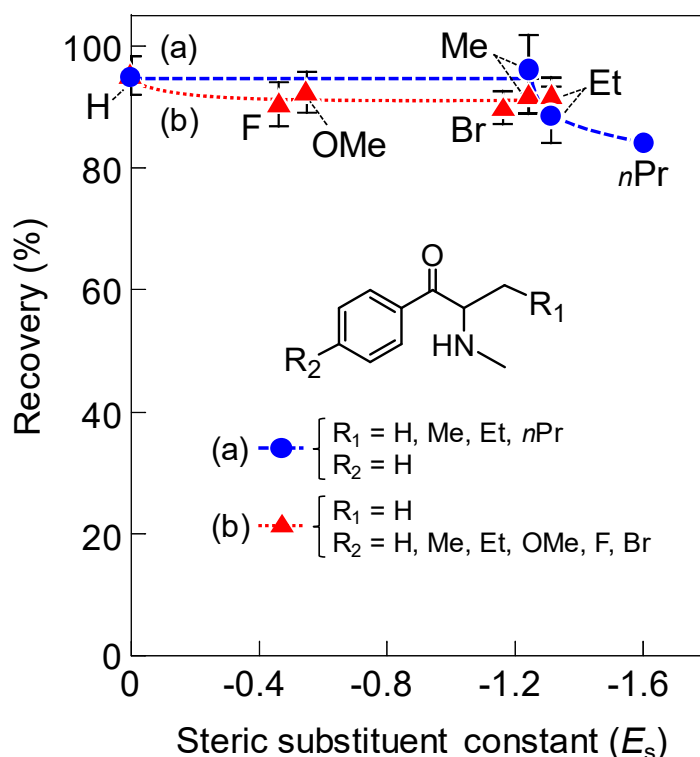


Fig. 7.3 Relationship between the extraction recoveries (mean \pm SD, $n = 3$) and the steric substituent constant (E_s) of the synthetic cathinones categorized based on structure into groups (a) and (b). E_s is normalized by $H = 0$.

7.3.3 Extraction of synthetic cathinones from urine and whole blood samples

The MIP-SPE recoveries of the 11 synthetic cathinones from urine samples (at concentrations of 10 and 1000 ng/mL) are summarized in Table 7.2, where they are also compared with the recoveries obtained using the two conventional extraction methods, hydrophilic polymer-based SPE and LLE. It is apparent that the MIP-SPE intraday recoveries of synthetic cathinones from urine samples ranged from 60.5 to 84.2% (mean: 73.2%) at a concentration of 10 ng/mL and from 67.7 to 89.3% (mean: 78.9%) at 1000 ng/mL. The interday recoveries were in the 64.9–88.5% range (mean: 79.8%) at 10 ng/mL and in the 70.3–90.8% range (mean: 81.2%) at 1000 ng/mL. These recoveries were significantly higher than those obtained using the two conventional methods: hydrophilic polymer-based SPE afforded recovery of 12.3–78.6% (mean: 58.1%) at 10 ng/mL and 24.9–90.8% (mean: 65.5%) at 1000 ng/mL, whereas LLE resulted in 8.3–79.2% (mean: 38.4%) recovery at 10 ng/mL and 26.2–92.5% (mean: 53.1%) recovery at 1000 ng/mL. The intraday and interday reproducibilities (RSDs) of the MIP-SPE recoveries were determined to be 0.9–13.9% and 1.7–9.5%, respectively, and were comparable with the reproducibilities obtained using the two conventional methods. Examination of the matrix effect revealed that it is less pronounced for MIP-SPE than for hydrophilic polymer-based SPE, and is similar to that measured for LLE (Table 7.3). These results indicate that the MIP-SPE method afforded enhanced extraction efficiency and matrix-removal capability compared to the two conventional methods, attributed to the high selectivity of MIP for synthetic cathinones. The regression equations, correlation coefficients, and LODs for the 11 synthetic cathinones are shown in Table 7.4. Each regression relationship exhibited favorable linearity with high correlation coefficient, and the LODs were determined to be 0.011–0.13 ng/mL, which highlights the viability of highly sensitive analysis by LC/ESI-QqQ-MS.

Table 7.2 Mean recoveries and relative standard deviations (RSDs) obtained for the MIP-SPE, hydrophilic polymer-based SPE, and LLE methods for 11 synthetic cathinones (10 and 1000 ng/mL) extracted from urine ($n = 3$).

Compound	Added conc. (ng/mL)	MIP-SPE				Hydrophilic polymer-based SPE		LLE	
		Intraday		Interday		Intraday		Intraday	
		Mean (%)	RSD (%)	Mean (%)	RSD (%)	Mean (%)	RSD (%)	Mean (%)	RSD (%)
Methcathinone	10	73.6	7.0	81.1	4.1	44.1	1.1	22.5	10.8
	1000	79.0	2.1	82.0	5.4	51.6	7.8	36.0	10.6
Methylone	10	82.1	13.9	86.7	7.5	78.6	5.0	79.2	1.2
	1000	89.3	1.4	90.8	2.7	90.8	4.3	92.5	2.0
Ethcathinone	10	70.5	8.2	80.4	8.6	49.3	1.7	23.3	12.7
	1000	74.9	1.9	77.4	5.4	58.3	2.7	36.5	11.8
Buphedrone	10	70.8	10.2	82.2	9.5	72.0	0.4	33.7	7.0
	1000	75.0	1.5	77.7	4.0	81.8	10.1	46.1	13.1
Pentedrone	10	68.5	9.0	76.7	5.5	70.1	0.4	33.4	6.2
	1000	80.4	1.5	83.1	3.2	73.2	6.0	51.5	11.3
Hexedrone	10	73.4	9.0	79.1	2.9	71.6	2.1	41.3	4.8
	1000	75.5	1.9	78.1	3.2	71.0	5.4	56.1	10.4
4-MMC	10	79.6	9.7	85.5	1.7	62.2	2.7	42.7	7.9
	1000	84.4	1.4	86.6	3.1	70.2	2.1	58.3	4.2
4-EMC	10	70.4	10.4	74.3	3.8	50.7	4.1	40.3	7.0
	1000	76.9	1.0	78.6	2.6	57.5	7.1	56.2	3.8
4-MeOMC	10	84.2	11.0	88.5	5.0	73.6	5.1	74.6	1.6
	1000	88.8	0.9	90.0	3.0	85.2	4.4	86.3	1.6
4-FMC	10	71.3	8.9	78.7	4.0	54.7	1.3	23.4	12.5
	1000	76.0	2.5	78.7	5.1	56.7	5.1	38.1	11.2
4-BMC	10	60.5	12.4	64.9	4.3	12.3	3.6	8.3	25.8
	1000	67.7	2.2	70.3	9.4	24.9	39.2	26.2	13.8

Table 7.3 Matrix effects observed for the MIP-SPE, hydrophilic polymer-based SPE, and LLE methods for 11 synthetic cathinones (10 and 1000 ng/mL) extracted from urine.

Compound	Added conc. (ng/mL)	MIP-SPE (%)	Hydrophilic polymer-based SPE (%)	LLE (%)
Methcathinone	10	19.8	6.9	1.5
	1000	3.4	8.2	-0.9
Methylone	10	3.4	12.8	4.0
	1000	4.0	15.7	2.4
Ethcathinone	10	0.9	14.6	4.1
	1000	2.8	16.7	1.7
Buphedrone	10	0.6	12.9	5.2
	1000	1.4	20.2	4.1
Pentedrone	10	3.5	15.3	4.2
	1000	5.4	21.4	0.1
Hexedrone	10	5.9	17.8	4.6
	1000	5.2	21.4	0.9
4-MMC	10	0.4	8.8	5.0
	1000	1.7	8.8	2.7
4-EMC	10	0.9	17.1	6.6
	1000	1.7	18.0	2.9
4-MeOMC	10	2.6	15.4	4.5
	1000	1.2	19.1	2.7
4-FMC	10	4.3	-12.3	0.01
	1000	3.9	6.6	-1.0
4-BMC	10	4.7	8.5	3.2
	1000	7.9	6.9	-9.1

Table 7.4 Regression equations, correlation coefficients, and limit of detections (LODs) determined for 11 synthetic cathinones extracted from urine.

Compound	Equation	Correlation coefficient (R)	LOD (ng/mL)
Methcathinone	$y = 0.0116x - 0.0142$	0.9999	0.027
Methylone	$y = 0.0147x - 0.0627$	0.9997	0.011
Ethcathinone	$y = 0.0088x - 0.0031$	0.9999	0.037
Buphedrone	$y = 0.0054x - 0.0116$	0.9999	0.064
Pentedrone	$y = 0.0058x - 0.0040$	0.9999	0.13
Hexedrone	$y = 0.0067x - 0.0148$	0.9999	0.045
4-MMC	$y = 0.0143x - 0.0507$	0.9999	0.029
4-EMC	$y = 0.0163x - 0.0581$	0.9998	0.038
4-MeOMC	$y = 0.0135x - 0.0544$	0.9998	0.052
4-FMC	$y = 0.0084x - 0.0127$	0.9999	0.099
4-BMC	$y = 0.0077x - 0.0356$	0.9998	0.032

The recoveries obtained for synthetic cathinones from whole blood samples (10 and 1000 ng/mL) are summarized in Table 7.5. The intraday recoveries were 52.4–73.6% (mean: 65.5%) at 10 ng/mL and 60.1–84.3% (mean: 75.2%) at 1000 ng/mL. The interday recoveries were 60.1–79.5% (mean: 68.5%) and 64.6–87.2% (mean: 74.8%) at 10 ng/mL and 1000 ng/mL, respectively. This performance is comparable to that determined for the urine samples. Considering that whole blood samples intrinsically include more matrix components than urine, these results further corroborate the high selectivity of the MIP-SPE method. The extraction recoveries and RSDs were similar to those obtained for the urine samples, i.e. 0.4–17.9% for intraday and 1.7–17.0% for interday recoveries. Furthermore, the regression equation for each compound afforded high correlation coefficient with low LOD at ppt levels (0.015–0.15 ng/mL, Table 7.6), which corresponds to a sensitivity similar to that observed for the urine samples.

Synthetic cathinones can have significant toxicological effects in humans. In fatal cases, the concentrations of 4-MMC in urine and blood were reported to be 144–198 and 0.04–22 $\mu\text{g/mL}$, respectively [128–132], and those of methylone were 0.22–38 and 0.06–6.6 $\mu\text{g/mL}$, respectively [130,133]. In non-fatal therapeutic cases, the blood concentrations of 4-MMC and 4-FMC were reported to be 0.013–0.412 and 0.136 $\mu\text{g/mL}$, respectively [132,134,135]. Considering these results in the context of the LODs obtained in the present work, MIP-SPE method can be used in therapeutic, clinical, and forensic toxicology analyses.

Table 7.5 Mean recoveries and relative standard deviations (RSDs) of 11 synthetic cathinones (10 and 1000 ng/mL) extracted from whole blood using the MIP-SPE method ($n = 3$).

Compound	Added conc. (ng/mL)	Intraday		Interday	
		Mean (%)	RSD (%)	Mean (%)	RSD (%)
Methcathinone	10	73.0	5.9	75.0	4.7
	1000	82.4	2.8	79.9	4.7
Methylone	10	73.6	12.0	79.5	12.0
	1000	84.3	5.4	87.2	6.2
Ethcathinone	10	63.5	7.9	65.3	9.2
	1000	71.7	1.2	70.5	2.1
Buphedrone	10	52.4	17.9	60.1	17.0
	1000	60.1	10.8	64.6	11.6
Pentedrone	10	71.3	8.0	74.2	9.4
	1000	81.9	1.9	81.1	2.4
Hexedrone	10	69.1	9.4	72.2	11.1
	1000	78.7	2.4	78.9	3.1
4-MMC	10	62.6	6.3	64.1	7.0
	1000	72.2	0.6	71.2	1.9
4-EMC	10	65.9	7.1	68.4	7.7
	1000	78.3	0.4	77.3	2.1
4-MeOMC	10	67.3	7.9	69.6	8.6
	1000	77.4	1.2	77.4	1.7
4-FMC	10	63.6	5.9	63.4	6.5
	1000	72.3	3.5	69.5	5.9
4-BMC	10	58.1	9.9	61.6	9.8
	1000	67.3	2.5	65.3	4.5

Table 7.6 Regression equations, correlation coefficients, and limit of detections (LODs) determined for 11 synthetic cathinones extracted from whole blood.

Compound	Equation	Correlation coefficient (R)	LOD (ng/mL)
Methcathinone	$y = 0.0101x - 0.0288$	0.9999	0.024
Methylone	$y = 0.0129x - 0.0420$	0.9999	0.015
Ethcathinone	$y = 0.0070x - 0.0319$	0.9999	0.085
Buphedrone	$y = 0.0047x - 0.0238$	0.9999	0.089
Pentedrone	$y = 0.0045x - 0.0159$	0.9999	0.11
Hexedrone	$y = 0.0064x - 0.0144$	0.9999	0.10
4-MMC	$y = 0.0124x - 0.0384$	0.9999	0.033
4-EMC	$y = 0.0150x - 0.0330$	0.9999	0.043
4-MeOMC	$y = 0.0118x - 0.0392$	0.9999	0.041
4-FMC	$y = 0.0062x - 0.0288$	0.9998	0.15
4-BMC	$y = 0.0053x - 0.0184$	0.9999	0.036

7.4 Summary

Extraction capabilities of the MIP-SPE method utilizing the AFFINILUTE MIP-Amphetamine cartridge for 11 synthetic cathinones, namely methcathinone, methylone, ethcathinone, buphedrone, pentedrone, hexedrone, 4-MMC, 4-EMC, 4-MeOMC, 4-FMC, and 4-BMC, from urine and whole blood samples were demonstrated. The pH for initial sample loading was optimized (pH 6). In regard to the relationship between the synthetic cathinone molecular structure and MIP-SPE recovery, substituent variation on the aromatic ring showed no effects while the longer alkyl side-chains slightly reduced extraction efficiency. The recoveries of the 11 synthetic cathinones from urine, obtained using the MIP-SPE method, were higher than those obtained using the conventional hydrophilic polymer-based SPE and LLE methods. The matrix effect was less significant for the MIP-SPE method than for hydrophilic polymer-based SPE, and was comparable to the matrix-removal capacity of the

LLE process. The recoveries of the synthetic cathinones from whole blood were comparable to those from urine. Therefore, MIP-SPE represents a new tool that can be exploited for the detection and quantitation of synthetic cathinones in crude biological samples.

Chapter 8 Conclusion

The first objective of this thesis was to clearly and reliably differentiate the fluorine positional isomers of synthetic cannabinoids and synthetic cathinones which are difficult to distinguish by conventional chromatographic and mass spectral analyses. The second objective was to develop a class-selective sample clean-up method for the extraction of synthetic cathinones from biological samples. The results obtained in each chapter can be summarized as follows.

In Chapter 1, the current situation and challenges regarding NPS analysis and the objectives of this study were described.

In Chapter 2, AB-FUBINACA (*para*) and its two fluorine positional (*ortho* and *meta*) isomers on the phenyl ring were differentiated via GC/EI-QqQ-MS. ERMS showed that the three isomers differed in relative abundances of the ions at m/z 109 (fluorobenzyl cation) and 253 ($[M-NHCHiPrCONH_2]^+$), although the observed product ions were identical at any CE tested. The logarithmic values of the abundance ratio of m/z 109 to m/z 253 ions [$\ln(A_{109}/A_{253})$] followed the order *meta* < *ortho* < *para* at each CE. In addition, the relationship between $\ln(A_{109}/A_{253})$ and CE was linear with high correlation coefficients for all analytes. Theoretical free energy calculations showed that the differences in abundances could be attributed to the differences in dissociation reactivity between the fluorobenzyl group and indazole moiety due to the halogen-positional effect on the phenyl ring, which confirmed the relationship of the three isomers obtained by ERMS. The present methodology allowed the three positional isomers to be clearly and reliably differentiated.

In Chapter 3, a practical method for elucidating the *o*-, *m*-, or *p*-fluorine substitution pattern of indazole-type synthetic cannabinoids containing a fluorobenzyl group at the N-1 position was described. This method expanded the application coverage of the ERMS

differentiation methodology developed in Chapter 2. The three positional isomeric model compounds of synthetic cannabinoids, *o*-, *m*-, and *p*-FUBINAEs, were synthesized. ERMS analysis showed that the three isomers differed in their $\ln(A_{109}/A_{253})$ values, following the order *meta* < *ortho* < *para*, and increased linearly with increasing CE. Comparison of the $\ln(A_{109}/A_{253})$ plots of the FUBINAE isomers as a function of CE with similar plots of the three AB-FUBINACA isomers revealed that the FUBINAE isomers behaved similarly to the AB-FUBINACA isomers in response to the fluorine substitution position on the phenyl ring. Moreover, the plots of other indazole-type synthetic cannabinoids with a *p*-fluorobenzyl group, i.e., ADB-FUBINACA, FUB-AMB, FUB-APINACA, FUB-NPB-22, and FU-PX-2, corresponded with that of *p*-FUBINAE, as did the extract of the herbal product containing AB-FUBINACA. Therefore, it was concluded the fluorine substitution position on the phenyl ring in fluorobenzyl group-containing indazole-type synthetic cannabinoids can be distinguished by collating data sets of model compounds according to the logarithmic plots of their mass spectral abundance ratios as a function of CE.

In Chapter 4, the differences between AB-FUBINACA and its five positional isomers (two fluorine positional (*ortho* and *meta*) isomers on the phenyl ring and three methyl positional isomers in the carboxamide side chain) were investigated using LC/ESI-LIT-MS and LC/ESI-QqQ-MS. Four of the positional isomers, excluding AB-FUBINACA and its *meta* isomer, were chromatographically separated using an ODS column in isocratic mode. The ESI-LIT-MS in negative ion mode could differentiate between the *ortho*-fluorine isomer, the *N*-(1-amino-2-methyl-1-oxobutan-2-yl) isomer, and the *N*-(1-amino-1-oxobutan-2-yl)-*N*-methyl isomer, based on their characteristic product ions observed in the MS³ stage. ERMS strategy using ESI-QqQ-MS clearly differentiated all six isomers by comparison of the logarithmic values of the product ion abundance ratios containing the positional isomeric moieties involved in CID reactions. This demonstrated that the ERMS methodology could be

used in combination with LC and ESI as well as GC and EI.

In Chapter 5, the developed ERMS differentiation methodology was applied to *o*-, *m*-, and *p*-FMCs. The three positional isomers exhibited differences in relative abundances of both *m/z* 95 (fluorophenyl cation) and 123 (fluorobenzoyl cation) in the product ion spectra. The logarithmic plots of the abundance ratios of these cations [$\ln(A_{95}/A_{123})$] followed the order of *ortho* < *para* < *meta* at every CE tested, which allowed the three isomers to be unambiguously differentiated. Theoretical dissociation energy calculations confirmed the relationship obtained by the ERMS analyses. Additional ERMS measurements of *o*-, *m*-, and *p*-MMCs showed that abundance differences among the FMCs could be attributed to the differences in their CID reactivities arising from the halogen-induced electron-donating resonance effects on the phenyl ring. Moreover, the developed differentiation method was successfully applied to actual seized samples of illicit drugs.

In Chapter 6, *o*-, *m*-, and *p*-FPPPs were differentiated using Triton-B-mediated one-pot S_NAr reaction with methanol at an ambient temperature, followed by chromatographic and mass spectral analyses of the corresponding products. In *p*-FPPP, fluorine was nucleophilically substituted by the methoxy group to afford *p*-MeOPPP, while the *o*- and *m*-FPPPs yielded the corresponding FPPP-enamine-pyrrolidine adducts, which allowed for unambiguous identification of the FPPP positional isomers by comparing the reaction product chromatograms and mass spectra. This approach, which does not require excess heating or use of metallic catalysts, features the advantages of simplicity and convenience.

In Chapter 7, a highly class-selective sample clean-up method for extracting synthetic cathinones from biological samples with a MIP-SPE cartridge was described. The optimal pH of the sample solution loaded onto the MIP-SPE cartridge was 6. In terms of the influence of the synthetic cathinone molecular structure on extraction recovery, substituent variation on the aromatic ring showed no effects, whereas the longer alkyl side-chains slightly reduced

extraction efficiency. MIP-SPE of 11 synthetic cathinones from urine samples yielded higher recoveries than two conventional methods (hydrophilic-polymer-based SPE and LLE), and a reduced matrix effect was observed compared to that observed using the hydrophilic polymer-based SPE. Recoveries of MIP-SPE from whole blood samples were comparable to those of the urine samples. The proposed MIP-SPE method can be applicable for the extraction and quantitative determination of synthetic cathinones in forensic biological samples.

In this thesis, a novel and practical positional isomer differentiation method using ERMS was developed for NPSs, including synthetic cannabinoid and synthetic cathinones. S_NAr derivatization reaction was also useful for differentiation of the positional isomers of synthetic cathinones. In addition, a highly class-selective extraction method for synthetic cathinones via MIP-SPE was developed. We hope that the described methods will contribute significantly to reliable structural identification and efficient extraction for NPSs, and will find broad application in the forensic, therapeutic, and clinical fields.

References

- [1] Lewin, A. H.; Seltzman, H. H.; Carroll, F. I.; Mascarella, S. W.; Reddy, P. A. Emergence and properties of spice and bath salts: a medicinal chemistry perspective. *Life Sci.* **2014**, *97*, 9–19.
- [2] Khullar, V.; Jain, A.; Sattari, M. Emergence of new classes of recreational drugs—synthetic cannabinoids and cathinones. *J Gen Intern Med.* **2014**, *29*, 1200–1204.
- [3] Dart, R. C.; Bronstein, A. C.; Spyker, D. A.; Cantilena, L. R.; Seifert, S. A.; Heard, S. E.; Krenzelok, E. P. Poisoning in the United States: 2012 emergency medicine report of the National Poison Data System. *Ann. Emerg. Med.* **2015**, *65*, 416–422.
- [4] United Nations Office on Drugs and Crime (UNODC). UNODC Early Warning Advisory (EWA) on New Psychoactive Substances (NPS). <https://www.unodc.org/LSS/Home/NPS> (accessed May 30, 2019).
- [5] UNODC. The challenge of new psychoactive substances Global SMART Programme. <https://www.unodc.org/unodc/en/scientists/the-challenge-of-new-psychoactive-substances---global-smart-programme.html> (accessed May 30, 2019).
- [6] European Monitoring Center for Drugs and Drug Addiction (EMCDDA). European Drug Report 2018: Trends and Developments. http://www.emcdda.europa.eu/publications/edr/trends-developments/2018_en (accessed May 30, 2019).
- [7] Aung, M. M.; Griffin, G.; Huffman, J. W.; Wu, M. J.; Keel, C.; Yang, B.; Showalter, V. M.; Abood, M. E.; Martin, B. R. Influence of the N-1 alkyl chain length of cannabimimetic indoles upon CB₁ and CB₂ receptor binding. *Drug Alcohol Depend.* **2000**, *60*, 133–140.
- [8] Huffman, J. W.; Szklennik, P. V.; Almond, A.; Bushell, K.; Selley, D. E.; He, H.; Cassidy, M. P.; Wiley, J. L.; Martin, B. R. 1-Pentyl-3-phenylacetylindoles, a new class of cannabimimetic indoles. *Bioorg. Med. Chem. Lett.* **2005**, *15*, 4110–4113.
- [9] Makriyannis, A.; Deng, H. (University of Connecticut, USA). Cannabimimetic indole derivatives. US Patent US6900236B1, May 31, 2005.
- [10] Castaneto, M. S.; Gorelick, D. A.; Desrosiers, N. A.; Hartman, R. L.; Pirard, S.; Huestis, M. A. Synthetic cannabinoids: epidemiology, pharmacodynamics, and clinical implications. *Drug Alcohol Depend.* **2014**, *144*, 12–41.
- [11] Auwärter, V.; Dresen, S.; Weinmann, W.; Müller, M.; Pütz, M.; Ferreiros, N. Spice and other herbal blends: harmless incense or cannabinoid designer drugs? *J. Mass Spectrom.* **2009**, *44*, 832–837.
- [12] Uchiyama, N.; Kikura-Hanajiri, R.; Kawahara, N.; Haishima, Y.; Goda, Y. Identification of a cannabinoid analog as a new type of designer drug in a herbal product. *Chem. Pharm. Bulletin (Tokyo)* **2009**, *57*, 439–441.
- [13] Deluca, P.; Davey, Z.; Corazza, O.; Furia, L. D.; Farre, M.; Flesland, L. H.; Mannonen,

- M.; Majava, A.; Peltoniemi, T.; Pasinetti, M.; Pezzolesi, C.; Scherbaum, N.; Siemann, H.; Skutle, A.; Torrens, M.; van der Kreeft P.; Iversen, E.; Schifano, F. Identifying emerging trends in recreational drug use; outcomes from the Psychonaut Web Mapping Project. *Prog. Neuropsychopharmacol. Biol. Psychiatry* **2012**, *39*, 221–226.
- [14] EMCDDA. Synthetic cathinones drug profiles. <http://www.emcdda.europa.eu/publications/drug-profiles/synthetic-cathinones> (accessed May 30, 2019).
- [15] Coppola, M.; Mondola, R. Synthetic cathinones: chemistry, pharmacology and toxicology of a new class of designer drugs of abuse marketed as "bath salts" or "plant food". *Toxicol. Lett.* **2012**, *211*, 144–149.
- [16] Miotto, K.; Striebel, J.; Cho, A. K.; Wang, C. Clinical and pharmacological aspects of bath salt use: a review of the literature and case reports. *Drug Alcohol Depend.* **2013**, *132*, 1–12.
- [17] German, C. L.; Fleckenstein, A. E.; Hanson, G. R. Bath salts and synthetic cathinones: an emerging designer drug phenomenon. *Life Sci.* **2014**, *97*, 2–8.
- [18] Shuji, K. Acute drug consumption and motor vehicle collision: A systematic review of 96 cases in Japan 2012-2014, *Jpn. J. Forensic Sci. Tech.* **2017**, *22*, 49–59. (in Japanese)
- [19] Kikura-Hanajiri, R.; Uchiyama, N.; Kawamura, M.; Ogata, J.; Goda, Y. Prevalence of new designer drugs and their legal status in Japan, *Yakugaku Zasshi* **2013**, *133*, 31–40. (in Japanese)
- [20] Kikura-Hanajiri, R. Changes in the prevalence of new psychoactive substances and their legal status in Japan, *Nihon Yakurigaku Zasshi* **2017**, *150*, 129–134. (in Japanese)
- [21] UNODC. Global SMART Update 2017 Vol. 17. <https://www.unodc.org/unodc/en/scientists/global-smart-update-2017-vol-17.html> (accessed May 30, 2019).
- [22] Cuypers, E.; Bonneure, A.-J.; Tytgat, J. The use of presumptive color tests for new psychoactive substances. *Drug Test. Anal.* **2016**, *8*, 136–140.
- [23] Toole, K.; Philp, M.; Krayem, N.; Fu, S.; Shimmon, R.; Taflaga, S. Color tests for the preliminary identification of new psychoactive substances. *Methods Mol. Biol.* **2018**, *1810*, 1–11.
- [24] Barnes, A. J.; Spinelli, E.; Young, S.; Martin, T. M.; Kleete, K. L.; Huestis, M. A. Validation of an ELISA synthetic cannabinoids urine assay. *Ther. Drug Monit.* **2015**, *37*, 661–669.
- [25] Kanai, K.; Takekawa, K.; Kumamoto, T.; Ishikawa, T.; Ohmori, T. Simultaneous analysis of six phenethylamine-type designer drugs by TLC, LC-MS, and GC-MS. *Forensic Toxicol.* **2008**, *26*, 6–12.
- [26] Jones, L. E.; Stewart, A.; Peters, K. L.; McNaul, M.; Speers, S. J.; Fletcher, N. C.; Bell, S. E. J. Infrared and raman screening of seized novel psychoactive substances: a large scale study of >200 samples. *Analyst* **2016**, *141*, 902–909.

- [27] Miller, J. M. *Chromatography: Concepts and Contrasts*, 2nd edition; John Wiley & Sons: Hoboken, 2009.
- [28] Gross, J. H. *Mass Spectrometry: A Textbook*, Third edition; Springer: Berlin, 2017.
- [29] Gwak, S.; Arroyo-Mora, L. E.; Almirall, J. R.; Qualitative analysis of seized synthetic cannabinoids and synthetic cathinones by gas chromatography triple quadrupole tandem mass spectrometry. *Drug Test. Anal.* **2015**, *7*, 121–130.
- [30] Ibanez, M.; Bijlsma, L.; van Nuijs, A. L.; Sancho, J. V.; Haro, G.; Covaci, A.; Hernandez, F. Quadrupole-time-of-flight mass spectrometry screening for synthetic cannabinoids in herbal blends. *J. Mass Spectrom.* **2013**, *48*, 685–694.
- [31] Peters, J. R.; Keasling, R.; Brown, S. D.; Pond, B. B. Quantification of synthetic cathinones in rat brain using HILIC-ESI-MS/MS. *J. Anal. Toxicol.* **2016**, *40*, 718–725.
- [32] Pan, M.; Xiang, P.; Yu, Z.; Zhao, Y.; Yan, H.; Development of a high-throughput screening analysis for 288 drugs and poisons in human blood using Orbitrap technology with gas chromatography-high resolution accurate mass spectrometry. *J. Chromatogr. A* **2019**, *1587*, 209–226.
- [33] Scientific Working Group for the Analysis of Seized Drugs (SWGDRUG). SWGDRUG Recommendations Edition 7.1 (2016-June-09). <http://swgdrug.org/approved.htm> (accessed May 30, 2019).
- [34] Hudson, S.; Ramsey, J. The emergence and analysis of synthetic cannabinoids. *Drug Test. Anal.* **2011**, *3*, 466–478.
- [35] Majchrzak, M.; Celiński, R.; Kuś, P.; Kowalska, T.; Sajewicz, M. The newest cathinone derivatives as designer drugs: an analytical and toxicological review. *Forensic Toxicol.* **2018**, *36*, 33–50.
- [36] Tsujikawa, K.; Mikuma, T.; Kuwayama, K.; Miyaguchi, H.; Kanamori, T.; Iwata, Y. T.; Inoue, H. Degradation pathways of 4-methylmethcathinone in alkaline solution and stability of methcathinone analogs in various pH solutions. *Forensic Sci. Int.* **2012**, *220*, 103–110.
- [37] Grigoryev, A.; Kavanagh, P.; Melnik, A.; Savchuk, S.; Simonov, A. Gas and liquid chromatography-mass spectrometry detection of the urinary metabolites of UR-144 and its major pyrolysis product. *J. Anal. Toxicol.* **2013**, *37*, 265–276.
- [38] Kerrigan, S.; Savage, M.; Cavazos, C.; Bella, P. Thermal degradation of synthetic cathinones: implications for forensic toxicology. *J. Anal. Toxicol.* **2016**, *40*, 1–11.
- [39] Tsujikawa, K.; Mikuma, T.; Kuwayama, K.; Miyaguchi, H.; Kanamori, T.; Iwata, Y. T.; Inoue, H. Identification and differentiation of methcathinone analogs by gas chromatography-mass spectrometry. *Drug Test. Anal.* **2013**, *5*, 670–677.
- [40] Collins, M.; Donnelly, C.; Cameron, S.; Tahtouh, M.; Salouros, H. Identification and characterization of N-tert-butoxycarbonyl-MDMA: a new MDMA precursor. *Drug Test. Anal.* **2017**, *9*, 399–404.

- [41] Wiley, J. L.; Marusich, J. A.; Lefever, T. W.; Grabenauer, M.; Moore, K. N.; Thomas, B. F. Cannabinoids in disguise: Δ^9 -tetrahydrocannabinol-like effects of tetramethylcyclopropyl ketone indoles. *Neuropharmacology* **2013**, *75*, 145–154.
- [42] Gurney, S. M. R.; Scott, K. S.; Kacinko, S. L.; Presley, B. C.; Logan, B. K. Pharmacology, toxicology, and adverse effects of synthetic cannabinoid drugs. *Forensic Sci. Rev.* **2014**, *26*, 53–78.
- [43] Gatch, M. B.; Forster, M. J. Δ^9 -Tetrahydrocannabinol-like effects of novel synthetic cannabinoids in mice and rats. *Psychopharmacology* **2016**, *233*, 1901–1910.
- [44] Ashton, J. C. Synthetic cannabinoids as drugs of abuse. *Curr. Drug Abuse Rev.* **2012**, *5*, 158–168.
- [45] GOV.UK. ACMD report on the major cannabinoid agonists. <https://www.gov.uk/government/publications/acmd-report-on-the-major-cannabinoid-agonists> (accessed May 30, 2019).
- [46] GOV.UK. Forensic early warning system (FEWS) annual report. <https://www.gov.uk/government/publications/forensic-early-warning-system-fews-annual-report> (accessed May 30, 2019).
- [47] GOV.UK. ACMD: further consideration of the synthetic cannabinoids. <https://www.gov.uk/government/publications/acmd-further-consideration-of-the-synthetic-cannabinoids> (accessed May 30, 2019)
- [48] Shanks, K. G.; Dahn, T.; Behonik, G.; Terrell, A. Analysis of first and second generation legal highs for synthetic cannabinoids and synthetic stimulants by ultra-performance liquid chromatography and time of flight mass spectrometry. *J. Anal. Toxicol.* **2012**, *36*, 360–371.
- [49] Uchiyama, N.; Matsuda, S.; Wakana, D.; Kikura-Hanajiri, R.; Goda, Y. New cannabimimetic indazole derivatives, *N*-(1-amino-3-methyl-1-oxobutan-2-yl)-1-pentyl-1*H*-indazole-3-carboxamide (AB-PINACA) and *N*-(1-amino-3-methyl-1-oxobutan-2-yl)-1-(4-fluorobenzyl)-1*H*-indazole-3-carboxamide (AB-FUBINACA) identified as designer drugs in illegal products. *Forensic Toxicol.* **2013**, *31*, 93–100.
- [50] Castaneto, M. S.; Wohlfarth, A.; Pang, S.; Zhu, M.; Scheidweiler, K. B.; Kronstrand R.; Huestis, M. A. Identification of AB-FUBINACA metabolites in human hepatocytes and urine using high-resolution mass spectrometry. *Forensic Toxicol.* **2015**, *33*, 295–310.
- [51] Buchler, I. P.; Hayes, M. J.; Hegde, S. G.; Hockerman, S. L.; Jones, D. E.; Kortum, S. W.; Rico, J. G.; Tenbrink, R. E.; Wu, K. K. (Pfizer Inc., USA). Indazole derivatives. US Patent CA2714573A1, September 3, 2009.
- [52] Belal, T.; Awad, T.; DeRuiter, J.; Clark, R. GC-MS studies on acylated derivatives of 3-methoxy-4-methyl- and 4-methoxy-3-methyl-phenethylamines: regioisomers related to 3,4-MDMA. *Forensic Sci. Int.* **2008**, *178*, 61–82.

- [53] Rösner, P.; Junge, T. Investigation of the alkylamino group of aliphatic and arylaliphatic amines by collision-induced dissociation mass spectra of $C_4H_{10}N^+$ immonium ions. *J. Mass Spectrom.* **1996**, *31*, 1047–1053.
- [54] Smith, F. T.; DeRuiter, J.; Abdel-Hay, K.; Clark, C. R. GC-MS and FTIR evaluation of the six benzoyl-substituted-1-pentylindoles: isomeric synthetic cannabinoids. *Talanta* **2014**, *129*, 171–182.
- [55] Harris, D. N.; Hokanson, S.; Miller, V.; Jackson, G. P. Fragmentation differences in the EI spectra of three synthetic cannabinoid positional isomers: JWH-250, JWH-302, and JWH-201. *Inter. J. Mass. Spectrom.* **2014**, *368*, 23–29.
- [56] Zaitso, K.; Miyagawa, H.; Sakamoto Y.; Matsuta, S.; Tsuboi, K.; Nishioka H.; Katagi, M.; Sato, T.; Tatsuno, M.; Tsuchihashi, H.; Suzuki, K.; Ishii, A. Mass spectrometric differentiation of the isomers of mono-methoxyethylamphetamines and mono-methoxydimethylamphetamines by GC–EI–MS–MS. *Forensic Toxicol.* **2013**, *31*, 292–300.
- [57] Kusano, M.; Zaitso, K.; Nakayama, H.; Nakajima, J.; Hisatsune, K.; Moriyasu, T.; Matsuta, S.; Katagi, M.; Tsuchihashi, H.; Ishii, A. Positional isomer differentiation of synthetic cannabinoid JWH-081 by GC-MS/MS. *J. Mass Spectrom.* **2015**, *50*, 586–591.
- [58] Akamatsu, S.; Yoshida, M. Fragmentation of synthetic cannabinoids with an isopropyl group or a *tert*-butyl group ionized by electron impact and electrospray. *J. Mass Spectrom.* **2016**, *51*, 28–32.
- [59] Kohyama, E; Chikumoto, T.; Furusawa, R.; Suenami, K.; Kawashima, H.; Tada, H.; Nagai, H.; Soda, M.; Kitaichi, K.; Ito, T. Regioisomeric differentiation of synthetic cannabinoids with an *N*-fluorobenzyl indole core by gas chromatography–tandem mass spectrometry. *Forensic Chem.* **2017**, *6*, 28–35.
- [60] Jones, L.; Kollar, J. Differentiation of AB-FUBINACA. *Forensic Drug Review*. <http://www.forensicdrugreview.com/24> (accessed May 30, 2019).
- [61] McLuckey, S. A.; Glish, G. L.; Cooks, R. G. Kinetic energy effects in mass spectrometry/mass spectrometry using a sector/quadrupole tandem instrument. *Int. J. Mass Spectrom. Ion Phys.* **1981**, *39*, 219–230.
- [62] Fetterolf, D. D.; Yost, R. A. Energy-resolved collision-induced dissociation in tandem mass spectrometry. *Int. J. Mass Spectrom. Ion Phys.* **1982**, *44*, 37–50.
- [63] Harrison, A. G. Energy-resolved mass spectrometry: a comparison of quadrupole cell and cone-voltage collision-induced dissociation. *Rapid Commun. Mass Spectrom.* **1999**, *13*, 1663–1670.
- [64] Sjöberg, P. J. R.; Markides, K. E. Energy-resolved collision-induced dissociation atmospheric pressure chemical ionization mass spectrometry of constitutional and stereo steroid isomers. *J. Mass Spectrom.* **1998**, *33*, 872–883.

- [65] Yamagaki, T.; Fukui, K.; Tachibana, K. Analysis of glycosyl bond cleavage and related isotope effects in collision-induced dissociation quadrupole-time-of flight mass spectrometry of isomeric trehaloses. *Anal. Chem.* **2006**, *78*, 1015–1022.
- [66] Kurimoto, A.; Daikoku, S.; Mutsuga, S.; Kanie, O. Analysis of energy-resolved mass spectra at MSⁿ in a pursuit to characterize structural isomers of oligosaccharides. *Anal. Chem.* **2006**, *78*, 3461–3466.
- [67] Aboufazeli, F.; Kolli, V.; Dodds, E. D. A comparison of energy-resolved vibrational activation/dissociation characteristics of protonated and sodiated high mannose N-glycopeptides. *J. Am. Soc. Mass Spectrom.* **2015**, *26*, 587–595.
- [68] Toyama, A.; Nakagawa, H.; Matsuda, K.; Sato, T.; Nakamura, Y.; Ueda, K. Quantitative structural characterization of local N-glycan microheterogeneity in therapeutic antibodies by energy-resolved oxonium ion monitoring. *Anal. Chem.* **2012**, *84*, 9655–9662.
- [69] Snedecor, G. W.; Cochran, W. G. *Statistical Methods*, 8th edition; Iowa State University Press: Iowa City, 1989.
- [70] Becke, A. D. Density-functional thermochemistry. III. The role of exact exchange. *J. Chem. Phys.* **1993**, *98*, 5648–5652.
- [71] Lee, C.; Yang, W.; Parr, R. G. Development of the Colle-Salvetti correlation-energy formula into a functional of the electron density. *Phys. Rev. B* **1988**, *37*, 785–789.
- [72] Reddy, P. N.; Srikanth, R.; Bhanuprakash, K.; Srinivas, R. Selenoketene (H₂C=C=Se)⁺ and selenoketyl cumulene (HC=C=Se)⁺ ions and their neutral counterparts: a tandem mass spectrometric and computational study. *J. Mass Spectrom.* **2005**, *40*, 796–806.
- [73] Elrod, M. J. A comprehensive computational investigation of the enthalpies of formation and proto affinities of C₄H₇N and C₃H₃ON compounds. *Inter. J. Mass. Spectrom.* **2003**, *228*, 91–105.
- [74] Senda, N. The development of Winmostar, a GUI software for computational chemistry. *Idemitsugihou* **2006**, *49*, 106–111.
- [75] Hui, Z.; Jun, Z.; Xun, X. Quantum chemical calculations of bond dissociation energies for COOH scission and electronic structure in some acids. *Chi. Phys. B* **2013**, *22*, 023301.
- [76] Jiang, K.; Bian, G.; Pan, Y.; Lai, G. Recognizing *ortho*-, *meta*- or *para*-positional isomers of S-methyl methoxyphenylmethylenhydrazine dithiocarboxylates by ESI-MS²: the positional effect of the methoxyl substituent. *Inter. J. Mass. Spectrom.* **2011**, *299*, 13–19.
- [77] Banister, S. D.; Moir, M.; Stuart, J.; Kevin, R. C.; Wood, K. E.; Longworth, M.; Wilkinson, S. M.; Beinat, C.; Buchanan, A. S.; Glass, M.; Connor, M.; McGregor, I. S.; Kassiou, M. Pharmacology of indole and indazole synthetic cannabinoid designer

- drugs AB-FUBINACA, ADB-FUBINACA, AB-PINACA, ADB-PINACA, 5F-AB-PINACA, 5F-ADB-PINACA, ADBICA, and 5F-ADBICA. *ACS Chem. Neurosci.* **2015**, *6*, 1546–1559.
- [78] Uchiyama, N.; Matsuda, S.; Kawamura, M.; Kikura-Hanajiri, R.; Goda, Y. Two new-type cannabimimetic quinolinyl carboxylates, QUPIC and QUCHIC, two new cannabimimetic carboxamide derivatives, ADB-FUBINACA and ADBICA, and five synthetic cannabinoids detected with a thiophene derivative α -PVT and an opioid receptor agonist AH-7921 identified in illegal products. *Forensic Toxicol.* **2013**, *31*, 223–240.
- [79] Banister, S. D.; Longworth, M.; Kevin, R.; Sachdev, S.; Santiago, M.; Stuart, J.; James, B. C.; Mack, J. B. C.; Glass, M.; McGregor, I. S.; Connor, M.; Kassiou, M.; Pharmacology of valinate and *tert*-leucinate synthetic cannabinoids 5F-AMBICA, 5F-AMB, 5F-ADB, AMB-FUBINACA, MDMB-FUBINACA, MDMB-CHMICA, and Their Analogues. *ACS Chem. Neurosci.* **2016**, *7*, 1241–1254.
- [80] Hess, C.; Schoeder, C. T.; Pillaiyar, T.; Madea, B.; Christa, E.; Müller, C. E.; Pharmacological evaluation of synthetic cannabinoids identified as constituents of spice. *Forensic Toxicol.* **2016**, *34*, 329–343.
- [81] Murakami, T.; Iwamuro, Y.; Ishimaru, R.; Chinaka, S.; Sugimura, N.; Takayama, N.; Differentiation of AB-FUBINACA positional isomers by the abundance of product ions using electron ionization-triple quadrupole mass spectrometry. *J. Mass Spectrom.* **2016**, *51*, 1016–1022.
- [82] Tukey, J. W. Comparing individual means in the analysis of variance. *Biometrics* **1949**, *5*, 99–114.
- [83] Corder, G. W.; Foreman, D. I. Nonparametric Statistics for Non-Statisticians: A Step-by-Step Approach; John Wiley & Sons: Hoboken, 2009.
- [84] Gross, J. H. Principles of Ionization and Ion Dissociation; Springer: Berlin, 2011.
- [85] Vékey, K. Internal energy effects in mass spectrometry. *J. Mass Spectrom.* **1996**, *31*, 445–463.
- [86] Murakami, T.; Iwamuro, Y.; Ishimaru, R.; Chinaka, S.; Noda, I.; Higashibayashi, S.; Takayama, N. Elucidation of the fluorine substitution position on the phenyl ring of synthetic cannabinoids by electron ionization–triple quadrupole mass spectrometry. *Jpn. J. Forensic Sci. Tech.* **2017**, *22*, 133–143.
- [87] Wong, P. S. H.; Cooks, R. G. Ion trap mass spectrometry. *Current Separations*. <http://currentseparations.com/issues/16-3/cs16-3c.pdf> (accessed May 30, 2019).
- [88] EMCDDA. EMCDDA–Europol 2008 Annual Report on the implementation of Council Decision 2005/387/JHA. <http://www.emcdda.europa.eu/html.cfm/index132901EN.html> (accessed May 30, 2019).
- [89] Brandt, S. D.; Sumnall, H. R.; Measham, F.; Cole, J. Analyses of secondgeneration

- 'legal highs' in the UK: initial findings. *Drug Test. Anal.* **2010**, *2*, 377–382.
- [90] Archer, R. P. Fluoromethcathinone, a new substance of abuse. *Forensic Sci. Int.* **2009**, *185*, 10–20.
- [91] GOV.UK. ACMD report on the consideration of the cathinones. <https://www.gov.uk/government/publications/acmd-report-on-the-consideration-of-the-cathinones> (accessed May 30, 2019).
- [92] Federal Register. Schedules of controlled substances: temporary placement of 10 synthetic cathinones into schedule I. <https://www.federalregister.gov/documents/2014/01/28/2014-01172/schedules-of-controlled-substances-temporary-placement-of-10-synthetic-cathinones-into-schedule-i> (accessed May 30, 2019).
- [93] Federal Register. Schedules of controlled substances: placement of 10 synthetic cathinones into schedule I. <https://www.federalregister.gov/documents/2017/03/01/2017-03974/schedules-of-controlled-substances-placement-of-10-synthetic-cathinones-into-schedule-i> (accessed May 30, 2019).
- [94] SWGDRUG. Drug monographs. <http://www.swgdrug.org/monographs.htm> (accessed May 30, 2019).
- [95] Westphal, F.; Junge, T. Ring positional differentiation of isomeric N-alkylated fluorocathinones by gas chromatography/tandem mass spectrometry. *Forensic Sci. Int.* **2012**, *223*, 97–105.
- [96] Takeda, A.; Tagami, T.; Asada, A.; Doi, T.; Kawaguchi, M.; Satsuki, Y.; Sawabe, Y. Regioisomeric separation of ring-substituted cathinones by liquid chromatography-mass spectrometry with a naphthylethyl column. *Forensic Toxicol.* **2017**, *35*, 399–407.
- [97] Murakami, T.; Iwamuro, Y.; Ishimaru, R.; Chinaka, S.; Takayama, N.; Hasegawa, H. Differentiation of AB-FUBINACA and its five positional isomers using liquid chromatography–electrospray ionization-linear ion trap mass spectrometry and triple quadrupole mass spectrometry. *Forensic Toxicol.* **2018**, *36*, 351–358.
- [98] Ditchfield, R.; Hehre, W. J.; Pople, J. A. Self-consistent molecular-orbital methods. IX. An extended gaussian-type basis for molecular-orbital studies of organic molecules. *J. Chem. Phys.* **1971**, *54*, 724–728.
- [99] Knapp, D. R. Handbook of Analytical Derivatization Reactions; John Wiley & Sons: Hoboken, 1979.
- [100] Nagy, T.; Kuki, Á.; Nagy, L.; Zsuga, M.; Kéki, S. Rapid qualitative analysis of 2-flavonoids, rutin and silybin, in medical pills by direct analysis in real-time mass spectrometry (DART-MS) combined with in situ derivatization. *J. Mass Spectrom.* **2018**, *53*, 240–246.
- [101] Alsenedi, K. A.; Morrison, C. Comparison of six derivatizing agents for the determination of nine synthetic cathinones using gas chromatography-mass spectrometry. *Anal. Methods* **2017**, *9*, 2732–2743.

- [102] Murakami, T.; Iwamuro, Y.; Ishimaru, R.; Chinaka, S.; Kato, N.; Sakamoto, Y.; Sugimura, N.; Hasegawa, H. Energy-resolved mass spectrometry for differentiation of the fluorine substitution position on the phenyl ring of fluoromethcathinones. *J. Mass Spectrom.* **2019**, *54*, 205–212.
- [103] Meshram, H. M.; Goud, P. R.; Reddy, B. C.; Kumar, D. A. Triton B-mediated efficient and convenient alkoxylation of activated aryl and heteroaryl halides. *Synth. Commun.* **2010**, *40*, 2122–2129.
- [104] Danikiewicz, W.; Bienkowski, T.; Kozłowska, D.; Zimnicka, M. Aromatic nucleophilic substitution (S_NAr) reactions of 1,2- and 1,4-halonitrobenzenes and 1,4-dinitrobenzene with carbanions in the gas phase. *J. Am. Soc. Mass Spectrom.* **2007**, *18*, 1351–1363.
- [105] McMurry, J. E. Organic Chemistry, sixth edition; Brooks Cole: California, 2003.
- [106] Abiedalla, Y.; DeRuiter, J.; Abdel-Hay, K. M.; Clark, C. R. Differentiation of homologous and regioisomeric methoxy-cathinone derivatives by GC–MS, MS/MS and GC–IR. *Forensic Chem.* **2016**, *2*, 46–54.
- [107] Matsuta, S.; Kakehashi, H.; Nakano, S.; Shima, N.; Kamata, T.; Nishioka, H.; Miki, A.; Sakamoto, Y.; Miyagawa, H.; Kusano, M.; Zaitso, K.; Tsuchihashi, H.; Katagi, M. Comprehensive analysis and structural estimation of synthetic cathinones using GC-MS/MS, *Jpn. J. Forensic Sci. Tech.* **2017**, *22*, 109–121.
- [108] Tsujikawa, K.; Kuwayama, K.; Kanamori, T.; Iwata, Y. T.; Inoue, H. Thermal degradation of α -pyrrolidinopentiophenone during injection in gas chromatography/mass spectrometry. *Forensic Sci. Int.* **2013**, *231*, 296–299.
- [109] Sellaergren, B. Molecularly Imprinted Polymers, Volume 23; Elsevier: Amsterdam, 2000.
- [110] Bui, B. T. S.; Haupt, K.; Molecularly imprinted polymers: synthetic receptors in bioanalysis. *Anal. Bioanal. Chem.* **2010**, *398*, 2481–2492.
- [111] Olsen, J.; Martin, P.; Wilson, I. D. Molecular imprints as sorbents for solid phase extraction: potential and applications. *Anal. Commun.* **1998**, *35*, 13H–14H.
- [112] Andersson, L. I. Molecular imprinting for drug bioanalysis: a review on the application of imprinted polymers to solid-phase extraction and binding assay. *J. Chromatogr. B* **2000**, *739*, 163–173.
- [113] Tamayo, F. G.; Turiel, E.; Martin-Esteban, A. Molecularly imprinted polymers for solid-phase extraction and solid-phase microextraction: recent developments and future trends. *J. Chromatogr. A* **2007**, *1152*, 32–40.
- [114] Pichon, V. Selective sample treatment using molecularly imprinted polymers. *J. Chromatogr. A* **2007**, *1152*, 41–53.
- [115] Turiel, E.; Martin-Esteban, A. Molecularly imprinted polymers for sample preparation: a review. *Anal. Chim. Acta* **2010**, *668*, 87–99.

- [116] Djozan, D.; Farajzadeh, M. A.; Sorouraddin, S. M.; Baheri, T. Molecularly imprinted-solid phase extraction combined with simultaneous derivatization and dispersive liquid-liquid microextraction for selective extraction and preconcentration of methamphetamine and ecstasy from urine samples followed by gas chromatography. *J. Chromatogr. A* **2012**, *1248*, 24–31.
- [117] Atlabachew, M.; Torto, N.; Chandravanshi, B. S.; Redi-Abshiro, M.; Chigome, S.; Mothibedi, K.; Combrinck, S. A (–)-norephedrine-based molecularly imprinted polymer for the solid-phase extraction of psychoactive phenylpropylamino alkaloids from Khat (*Catha edulis* Vahl. Endl.) chewing leaves. *Biomed. Chromatogr.* **2016**, *30*, 1007–1015.
- [118] Rahmani, M. E.; Ansari, M.; Kazemipour, M.; Nateghi, M. Selective extraction of morphine from biological fluids by magnetic molecularly imprinted polymers and determination using UHPLC with diode array detection. *J. Sep. Sci.* **2018**, *41*, 958–965.
- [119] Mergola, L.; Orabona, C.; Albin, E.; Vasapollo, G.; Scorrano, S.; Sole, R. D. Urinary L-kynurenine quantification and selective extraction through a molecularly imprinted solid-phase extraction device. *J. Sep. Sci.* **2018**, *41*, 3024–3212.
- [120] Biotage. AFFINILUTETM MIP Columns. <http://biotage.com/product-page/affinilute-mip-columns> (accessed May 30, 2019).
- [121] Biotage. Application note, AFFINILUTE MIP–Amphetamines. http://www.biotage.com/files/AN/AFFINILUTE_MIP/11357_an708_amphetamines.pdf (accessed May 30, 2019).
- [122] Widstrand, C.; Bergstrand, S.; Wihlborg, A. K. Technical Report, Simple, fast and class selective extraction of amphetamine and related drugs from urine using molecularly imprinted polymer (MIP) SPE and LC/MS/MS. https://www.sigmaaldrich.com/content/dam/sigma-aldrich/docs/Supelco/General_Information/t407148.pdf (accessed May 31, 2019).
- [123] Kumazawa, T.; Hasegawa, C.; Hara, K.; Uchigasaki, S.; Lee, X. P.; Seno, H.; Suzuki, O.; Sato, K. Molecularly imprinted solid-phase extraction for the selective determination of methamphetamine, amphetamine, and methylenedioxyphenylalkylamine designer drugs in human whole blood by gas chromatography-mass spectrometry. *J. Sep. Sci.* **2012**, *35*, 726–733.
- [124] Logan, B. K. Methamphetamine-effects on human performance and behavior. *Forensic Sci. Rev.* **2002**, *14*, 133–151.
- [125] Dioumaeva, I.; Hughes, J. M. SAMHSA-compliant LC/MS/MS analysis of amphetamines in urine with Agilent Bond Elut Plexa PCX and Agilent Poroshell 120. <https://www.agilent.com/cs/library/applications/5990-9623EN.pdf> (accessed May 31, 2019).

- [126] Predictive pK_a values of synthetic cathinones calculated by MarvinSketch ver. 17.25 (ChemAxon, Budapest, Hungary) were as follows; methcathinone, 8.02; methylone, 7.96; ethcathinone, 8.11, buphedrone, 8.18; penthedrone, 8.20; hexedrone, 8.20; 4-MMC, 8.05; 4-EMC, 8.04; 4-MeOMC, 8.01; 4-FMC, 7.98; and 4-BMC, 7.99.
- [127] Taft, R. W. Jr. Polar and steric substituent constants for aliphatic and *o*-benzoate groups from rates of esterification and hydrolysis of esters. *J. Am. Chem. Soc.* **1952**, *74*, 3120–3128.
- [128] Maskell, P. D.; Paoli, G. D.; Seneviratne, C.; Pounder, D. J. Mephedrone (4-methylmethcathinone)-related deaths. *J. Anal. Toxicol.* **2011**, *35*, 188–191.
- [129] Adamowicz, P.; Tokarczyk, B.; Stanaszek, R.; Slopianka, M. Fatal mephedrone intoxication—A case report. *J. Anal. Toxicol.* **2013**, *37*, 37–42.
- [130] Chung, H.; Lee, J.; Kim, E. Trends of novel psychoactive substances (NPSs) and their fatal cases. *Forensic Toxicol.* **2016**, *34*, 1–11.
- [131] Busardò, F. P.; Kyriakou, C.; Napoletano, S.; Marinelli, E.; Zaami, S. Mephedrone related fatalities: a review. *Eur. Rev. Med. Pharmacol. Sci.* **2015**, *19*, 3777–3790.
- [132] Papaseit, E.; Olesti, E.; de la Torre, R.; Torrens, M.; Farre, M. Mephedrone concentrations in cases of clinical intoxication. *Curr. Pharm. Des.* **2017**, *23*, 5511–5522.
- [133] Barrios, L.; Grison-Hernando, H.; Boels, D.; Bouquie, R.; Monteil-Ganiere, C.; Clement, R. Death following ingestion of methylone. *Int. J. Legal Med.* **2016**, *130*, 381–385.
- [134] Wood, D. M.; Davies, S.; Puchnarewicz, M.; Button, J.; Archer, R.; Ovaska, H.; Ramsey, J.; Lee, T.; Holt, D. W.; Dargan, P. I. Recreational use of mephedrone (4-methylmethcathinone, 4-MMC) with associated sympathomimetic toxicity. *J. Med. Toxicol.* **2010**, *6*, 327–330.
- [135] Thornton, S. L.; Gerona, R. R.; Tomaszewski, C. A. Psychosis from a bath salt product containing flephedrone and MDPV with serum, urine, and product quantification. *J. Med. Toxicol.* **2012**, *8*, 310–313.

List of Publications

List of Publications

1. Murakami, T.; Iwamuro, Y.; Ishimaru, R.; Chinaka, S.; Takayama, N.; Hasegawa, H. Differentiation of AB-FUBINACA and its five positional isomers using liquid chromatography–electrospray ionization–linear ion trap mass spectrometry and triple quadrupole mass spectrometry. *Forensic Toxicol.* **2018**, *36*, 351–358.
2. Murakami, T.; Iwamuro, Y.; Ishimaru, R.; Chinaka, S.; Hasegawa, H. Molecularly imprinted polymer solid-phase extraction of synthetic cathinones from urine and whole blood samples. *J. Sep. Sci.* **2018**, *41*, 4506–4514.
3. Murakami, T.; Iwamuro, Y.; Ishimaru, R.; Chinaka, S.; Kato, N.; Sakamoto, Y.; Sugimura, N.; Hasegawa, H. Energy-resolved mass spectrometry for differentiation of the fluorine substitution position on the phenyl ring of fluoromethcathinones. *J. Mass Spectrom.* **2019**, *54*, 205–212.
4. Murakami, T.; Iwamuro, Y.; Ishimaru, R.; Chinaka, S.; Hasegawa, H.; Kavthe, R. D.; Asao, N. Differentiation of *o*-, *m*-, and *p*-fluoro- α -pyrrolidinopropiophenones by Triton B-mediated one-pot reaction. *Forensic Sci. Int.* in press (Accepted: 4 June 2019)

List of Other Publications

1. Murakami, T.; Iwamuro, Y.; Chinaka, S.; Takayama, N.; Komatsu, T. Highly sensitive detection of organophosphorus pesticides using 5,10,15,20-tetrakis(4-hydroxyphenyl) porphyrin, *Anal. Sci.* **2015**, *31*, 1325–1328.
2. Murakami, T.; Iwamuro, Y.; Ishimaru, R.; Chinaka, S.; Sugimura, N.; Takayama, N.; Differentiation of AB-FUBINACA positional isomers by the abundance of product ions using electron ionization–triple quadrupole mass spectrometry. *J. Mass Spectrom.* **2016**, *51*, 1016–1022.
3. Murakami, T.; Iwamuro, Y.; Ishimaru, R.; Chinaka, S.; Noda, I.; Higashibayashi, S.; Takayama, N. Elucidation of the fluorine substitution position on the phenyl ring of synthetic cannabinoids by electron ionization–triple quadrupole mass spectrometry. *Jpn. J. Forensic Sci. Tech.* **2017**, *22*, 133–143.
4. Iwamuro, Y.; Murakami, T.; Ishimaru, R.; Chinaka, S. Postmortem detection of rocuronium and sugammadex by LC/MS in the blood of a patient who died on postoperative day 8. *Forensic Toxicol.* **2019**, *37*, 250–253.

Acknowledgments

This dissertation was completed under the direction of Professor Dr. Hiroshi Hasegawa, Institute of Science and Engineering, Kanazawa University. I would like to express my sincere gratitude and appreciation to him for continuous support, valuable instruction, and precious discussions throughout the duration of my studies.

I would like to express my gratitude to Professor Dr. Hirohisa Nagatani, Associate Professor Dr. Teruya Maki, and Associate Professor Dr. Akio Ohta, Institute of Science and Engineering, Kanazawa University, and Associate Professor Dr. Yohei Sasaki, Institute of Medical, Pharmaceutical and Health Sciences, Kanazawa University, for their valuable suggestions and helpful comments.

The experiments reported in this dissertation were mainly carried out at the Forensic Science Laboratory (FSL) of the Ishikawa Prefectural Police Headquarters. I would like to express my greatest appreciation to Dr. Nariaki Takayama, former director of the FSL; Dr. Satoshi Chinaka, vice director of the FSL; and Drs. Reiko Ishimaru and Yoshiaki Iwamuro, expert researchers of chemistry at the FSL, for their continuous support and helpful suggestions. This dissertation could not have been written without their guidance.

I would like to express my deep appreciation to Professor Dr. Teruyuki Komatsu, Faculty of Science and Engineering, Chuo University, for valuable instruction and significant encouragement since my undergraduate days.

I wish to express my deep appreciation to Professor Dr. Naoki Asao and Postdoctoral Researcher Dr. Rahul D. Kavthe, Graduate School of Science and Technology, Shinshu University; Associate Professor Dr. Shuhei Higashibayashi, Faculty of Pharmacy, Keio University; Dr. Ippei Noda and Ms. Mika Ohara, Institute for Molecular Science, for their advice, valuable discussions, and collaboration in the Nanotechnology Platform Program

(Molecule and Material Synthesis) of the Ministry of Education, Culture, Sports, Science and Technology (MEXT), Japan.

I gratefully acknowledge Dr. Natsuhiko Sugimura, Materials Characterization Central Laboratory, Waseda University, for useful advice and collaboration regarding quantum chemical calculations.

I wish to thank Mr. Yuki Sakamoto, Shimadzu Corporation, for helpful support in mass spectrometric measurements and collaboration.

I would like to acknowledge Dr. Noriyuki Kato and Mr. Kakeru Kobayashi, Scientific Crime Laboratory, Kanagawa Prefectural Police Headquarters, for their technical suggestions and collaboration.

I wish to express my gratitude to Mr. Koji Kanda, FSL of Mie Prefectural Police Headquarters, for his kind assistance with the chemical syntheses.

This work was partially supported by JSPS KAKENHI (Nos. 15H00542, 16H00703, and 17H00694) and Nanotechnology Platform Program (Molecule and Material Synthesis) of the MEXT, Japan (Nos. S-16-MS-0026b and NPS17012).

Finally, I would like to extend my gratitude to my beloved wife, Mami Murakami, for her constant support and cooperation, and my cute son, Soki Murakami, for giving me energy to continue my studies. I must also wholeheartedly thank my parents, Masami Murakami and Toyoko Murakami, for their continuous unwavering support and tender encouragement in every pursuit I have undertaken.

Takaya Murakami
Takaya Murakami